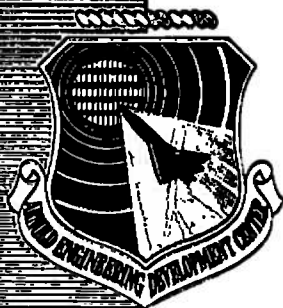


AEDC-TR-68-146

**ARCHIVE COPY
DO NOT LOAN**

cy,



**RADIATION HEAT FLUX
FROM HIGH PRESSURE ARCS**

**C. H. Marston, G. Frind, and B. Damsky
General Electric Company**

July 1968

This document has been approved for public release
and sale; its distribution is unlimited.

AEDC TECHNICAL LIBRARY



5 0720 00036 7575

**ARNOLD ENGINEERING DEVELOPMENT CENTER
AIR FORCE SYSTEMS COMMAND
ARNOLD AIR FORCE STATION, TENNESSEE**

PROPERTY OF U. S. AIR FORCE
AEDC LIBRARY
AF 40(600)1200

NOTICES

When U. S. Government drawings specifications, or other data are used for any purpose other than a definitely related Government procurement operation, the Government thereby incurs no responsibility nor any obligation whatsoever, and the fact that the Government may have formulated, furnished, or in any way supplied the said drawings, specifications, or other data, is not to be regarded by implication or otherwise, or in any manner licensing the holder or any other person or corporation, or conveying any rights or permission to manufacture, use, or sell any patented invention that may in any way be related thereto.

Qualified users may obtain copies of this report from the Defense Documentation Center.

References to named commercial products in this report are not to be considered in any sense as an endorsement of the product by the United States Air Force or the Government.

RADIATION HEAT FLUX
FROM HIGH PRESSURE ARCS

C. H. Marston, G. Frind, and B. Damsky
General Electric Company

This document has been approved for public release
and sale; its distribution is unlimited.

FOREWORD

The work reported herein was sponsored by Headquarters, Arnold Engineering Development Center (AEDC), Air Force Systems Command (AFSC), Arnold Air Force Station, Tennessee. The results of research presented were obtained by the General Electric Company, Missile and Space Division and Power Transmission Division, under Contract F40600-67-C-0005, AEDC Program Element 6140501F, Project 8951, Task 895107.

Capt. T. L. Hershey was the technical monitor. His advice and continuing interest were much appreciated. Dr. C. H. Marston and Dr. G. Frind were the principal investigators. Thermodynamic properties of Delrin plasma were the work of W. G. Browne and his staff. His advice and help are gratefully acknowledged. Miss A. M. Schorn did the programming for the Delrin radiation data compilation and the modifications to ARCRAD III. Her continued cooperation and consultations after transfer to a new job are especially appreciated. Mr. H. Sadjian's cogent advice in spectroscopic problems was very helpful for the investigation. Mr. R. N. Liang designed the critical elements of the electrical system. We wish to acknowledge the significant contribution of Mr. E. A. Baxter in designing part of the apparatus and in assisting with the measurements and the able assistance of Mr. B. A. Bellinger with the spectroscopic and photometer work. Finally, we would like to thank Mr. J. Heckendorn for his untiring and most efficient help with shop work, especially on the many modifications of ablation type constrictors.

This technical report has been reviewed and is approved.

Terry L. Hershey
Captain, USAF
Research Division
Directorate of Plans
and Technology

Edward R. Feicht
Colonel, USAF
Director of Plans
and Technology

ABSTRACT

An ablation type constrictor has been developed in which an electric arc at very high pressure is sufficiently stable for spectrographic measurements. Radial temperature distributions were determined for 250 ampere arcs in Delrin, $(\text{COH}_2)_n$, plasma at 100 and 150 atmospheres. Voltage gradient is constant along the arc axis and as high as 500 volts/cm. Pressure gradient in the constrictor is negligible. These two results indicate strongly that in spite of the self-induced flow field, the ablation type arc is homogeneous along the column.

Temperature measurement was based on non-optically thin Abel inversion of continuum intensity measurements useful to an optical depth of one or more, which related temperature to theoretically computed continuum emission. A previously developed arc radiation model was extended to include a few selected lines, and these contribute significantly to total radiation because they are very much broadened.

CONTENTS

Section	Page
I INTRODUCTION	1
II ANALYSIS	3
A. Radiant Emission from Self-Absorbing Arc Column	3
B. Spectral Lines	5
C. Two Zone Model.	6
D. Temperature Profiles from Non-Optically Thin Arcs	8
III COMPUTATION OF/WITH DELRIN PROPERTIES	10
A. Thermodynamic Properties of Delrin.	10
B. Transport Properties	11
C. Radiation Data	11
D. Computation Summary.	14
IV APPARATUS	31
V ARC CONSTRICTORS AND ARC STABILITY.	34
A. Constrictor Stabilization	34
B. Radiation Stabilization.	34
C. Development of the Ablation Type Constrictor for Optical Measurements	35
VI MEASUREMENT OF ARC PARAMETERS.	42
A. Pressure Rise in the Constrictor	42
B. Voltage Gradient and Axial Intensity	42
C. Constrictor Ablation Rate	43
VII MEASUREMENT OF RADIANT HEAT FLUX.	54
VIII TEMPERATURE MEASUREMENTS.	56
IX RESULTS AND CONCLUSIONS	64
A. Arc Temperature	64
B. Energy Distribution	65
C. Spectral Lines	65
D. Application to Air Arcs	65

CONTENTS (Cont'd)

Section	Page
APPENDIX I ABEL INVERSION AND INTEGRATION	70
APPENDIX II NON-OPTICALLY THIN ABEL INVERSION PROGRAMS	76
REFERENCES	99

LIST OF ILLUSTRATIONS (Cont)

<u>Figure</u>		<u>Page</u>
21	Voltage Gradient of Air Arc vs Pressure	49
22	Arc Voltage for Different Lengths of Plexiglas Constrictors, 150 atm.	50
23	Voltage Gradient of a Plexiglas Arc vs a Function of Pressure	50
24	Voltage Gradient of a Delrin Ablation Arc vs Current	51
25	Ablation of Delrin at 100 Atmospheres	52
26	Variation of Delrin Ablation Rates with Pressure	53
27	Calorimeter - Schematic and Photograph	55
28	Spectral Plate for the Measurement of the Temperature of a High Pressure Delrin Arc, 110 Atm, 250 Amp	58
29	Absolute Spectral Intensity of Delrin Arc, 110 Atm, 250 Amp	59
30	Local Emission Coefficient of Delrin Arc, 110 Atm, 250 Amp	60
31	Radial Temperature Distributions in High Pressure Delrin Arcs Based on Intensity Measurements at 7050 Å.	61
32	Summary of Temperature Measurements	63
33	Cumulative Net Continuum Radiation 157.5 Atm, 250 amp Temperature Profile.	67
34	Net Radiant Heat Flux per Unit Arc Column Length and per Wave Number in Vicinity of O ₇₇₇ Line	68
35	Net Radiant Heat Flux per Unit Arc Column Length and per Wave Number in Vicinity of H _α Line	69
36	Abel Integration.	75
37	Block Diagram, Program INVER	82

LIST OF ILLUSTRATIONS

<u>Figure</u>		<u>Page</u>
1	Radiant Interchange Model	4
2	Delrin Equilibrium Thermodynamic State	15
3	Delrin Composition, 10-200 atm	16
4	Oxygen Deionization Absorption Cross Sections	20
5	Negative Ion Photoionization Cross Sections	22
6	Delrin Spectral Radiance, 1 mm Slab 5000-25000 ^o K.	24
7	Computation for High Pressure Arc Radiation.	29
8	Emission Coefficient for use in Temperature Profile Determination . .	30
9	Overall View of Experimental Ensemble and Close-Up View	32
10	Constrictor Designed for Radiation Stabilization and Magnified Views of the Radiation Stabilized Arc.	37
11	Stability of Plexiglas Arc as Seen by a Streak Camera and a Framing Camera	38
12	Schematic of a Simple Two-Piece Ablation Constrictor.	39
13	Optical Constrictor - Schematic and Photograph	40
14	Streak of a Stable and an Unstable Test in Delrin Constrictors	41
15	Schematic Diagram for Pressure Rise Measurement and Photograph . .	44
16	Delrin Constrictor Ready for Firing	46
17	Arc Voltages for Delrin Constrictors of Different Lengths, 100 atm . .	47
18	Arc Voltages for Delrin Constrictors of Different Lengths, 150 atm . .	48
19	Arc Voltages for Delrin Constrictors of Different Lengths, 200 atm . .	48
20	Voltage Gradient of Delrin Ablation Arc vs Pressure	49

NOMENCLATURE

A	Area
A_j	j^{th} coefficient of a polynomial
c	Speed of light
c_1	Radiation constant, 1.1909×10^{-12} watt cm^2 /str
c_2	Radiation constant, $1.4380 \text{ cm}^{\circ}\text{K}$
e	2.718. . .
e	Electron charge
f_{lu}	Spectral line oscillator strength
$f(r)$	Function, Appendix I
$\hat{f}(r)$	Transformed function, Appendix I
g	Statistical weight
h	Planck constant
i	Summation index
$i(r)$	Emission coefficient
$I(x)$	Radiant Intensity
$I^*(x)$	Radiant Intensity which would have been observed except for self absorption
j	Summation index
J	Probability distribution, Equation 3
k	Absorption coefficient (cm^{-1})
k_B	Boltzmann constant
K_{mks}	8.98776×10^9 newton m^2/coul^2 , (equivalent to v-m/coul)
L	Physical length
L_0	Loschmitt Number
m	Summation limit
n	Wave number (cm^{-1})
N_ℓ	Number of particles in lower state of a transition
P	Pressure
R	Outer radius of arc

r	Radius
Ry	Rydberg constant
T	Temperature
v	$h\nu/k_B T$
x	{ Axial displacement; exponent in temperature Profile Equation 5; Variable in calculation of H absorption cross section, Equations 11 and 12
γ	Angle between surface normal and point of observation
η	$\frac{r}{r_k}$, see sentence preceding Equation 9, Appendix I
θ_i	$\frac{T_i - T_A}{T_A}$
ρ	Density
ρ_0	Density at STP
σ	Root mean square deviation
σ_i	Absorption cross section for i^{th} atomic species
ω	Solid angle

SECTION I

INTRODUCTION

One of the critical problems to be dealt with in the development of high enthalpy, high pressure electric arc heaters, and also in the generation of high pressure arc plasmas for basic studies of transport properties, is the strong influence of radiation in the transfer of energy from the arc to the surrounding gas and to the container walls. The objective of the study was to determine temperature profiles and heat fluxes from such high pressure arcs (100 atmospheres and up). In the pressure range of interest, self-absorption is an important phenomenon not only for discrete spectral lines but increasingly even for continuum radiation. It must therefore be accounted for in an analysis of the heat flux from such an arc.

Under a previous contract, an analytical model and computer program (called ARCRAD III) were developed for computation of radiant interchange within, and net radiant emission from, a cylindrically symmetric constricted arc. The importance of self-absorption was shown to be very much dependent on frequency. In the vacuum ultraviolet part of the spectrum, no energy reaches the constrictor wall while only a minor correction was necessary in computing temperature from continuum intensity measurements in the infrared (at 8330 Å).

Radiant emission from high pressure arcs is diminished somewhat by self-absorption but still constitutes a serious problem for arc confinement. Earlier work⁽¹⁾ showed, for instance, specific radial heat fluxes up to 100 kw/cm² at the constrictor wall. This value far exceeds the upper energy limit (~10 kw/cm²) for steady state, wall-stabilized arcs with water cooled copper constrictors so a practical very high pressure arc apparatus must use either stabilization principles. The ablation type arc has been used for the highest energies and pressures⁽²⁻⁷⁾. Other successful experiments have been made with a "free burning arc,"^(8,9) with arcs in rapid rotation in magnetic fields⁽¹⁰⁾ and with "swirl" stabilized arcs.

Whereas it seems unlikely that a steady state, wall-stabilized, arcing apparatus can successfully be operated at very high pressures and currents, the advantages of the wall-stabilized column for a quantitative measurement of the plasma parameters are obvious. Our early efforts⁽¹⁾ were therefore directed toward transient operation of wall-stabilized arcs in small diameter, uncooled copper constrictor cascades. Serious instabilities of the plasma column were encountered at pressures of the order of 100 atm., particularly at high currents, (400 amp), which limited our measurements to a study of the simpler arc parameters such as current, voltage gradient, arc diameter and radial heat flux.

A measurement of the more important plasma parameter temperature was accomplished at a current of 100 amps at a strongly reduced specific radiative flux. At this condition, the arc was still relatively stable.

To expand on the arc parameters pressure and current, in the work covered by this report, two approaches were followed:

First, working with a copper cage constrictor, additional effort was made to eliminate disturbances and thus delay the onset of instabilities; also, external magnetic fields were applied to supplement the stabilization afforded by the constrictor. Second, an ablation type constrictor was built. This is a constrictor made of a material which is an electrical insulator and which evaporates under action of the arc. Of these, only the ablation type constrictor proved to be sufficiently stable for measurement of the temperature distribution.

Two wall materials were used for the ablation type constrictor: Plexiglas for preliminary work because its transparency permitted photographic observation of the entire arc column, and Delrin because its composition is almost pure $(\text{H}_2\text{CO})_n$ (it does not carbonize), and thermodynamic and radiative properties, while neither simple nor immediately available, offered some prospect of yielding to calculation.

Progressing to higher arc pressure and current and therefore to higher density and higher temperature also meant that the effect of self-absorption on intensity profile measurements would be inescapable. It therefore becomes essential to account for it in the Abel inversion process of converting intensity to temperature profiles. A procedure suggested by Griem⁽¹¹⁾ was developed and proved highly successful.

Use of the continuum for temperature measurements required investigation of the contribution to total absorption coefficient from the wings of nearby spectral lines. A few lines were also chosen to check their contribution to net radiant emission.

SECTION II

ANALYSIS

A. RADIANT EMISSION FROM SELF-ABSORBING ARC COLUMN

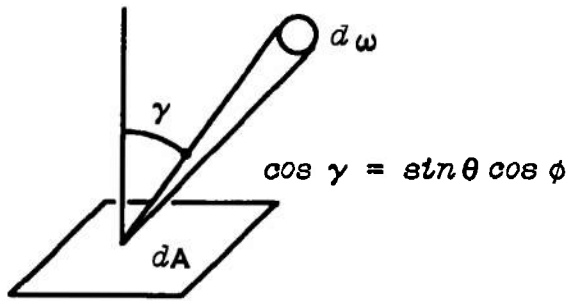
The model used in computing radiant emission from a self-absorbing arc column, and the analysis based on it, have been described in detail⁽¹⁾. The radiating arc column is assumed to be cylindrically symmetric, with a length-to-diameter ratio sufficiently large (10 or more) to neglect end effects. The arc cylinder is divided into annuli, each at a uniform temperature and density. Then, taking into account the effect of self-absorption within the annulus, volumetric emission from each annulus is converted to an equivalent radiant flux from the annulus boundary surfaces. The assumption of local thermodynamic equilibrium (LTE) permits the application of Kirchoff's law relating absorption, transmission, and emission. Except for the core, each annulus has an interior (concave) surface as well as an exterior (convex) surface from which radiant emission must be taken into account.

Radiant interchange among all annuli is computed by considering emission, absorption, and transmission along a representative array of paths from all the emitting surfaces to the outside of the column. Because self-absorption is significant, the controlling parameter is optical depth which is the dimensionless product of absorption coefficient and a characteristic length. Two optical depths are distinguished here: 1) absorption lengths along the transmission path, and 2) emission lengths within each annulus.

Computation of radiant interchange among the annuli proceeded as follows, Figure 1. Consider a surface element dA of an annulus, radiating with an average intensity I within a solid angle $d\omega$ over a wave number interval n in a direction making an angle γ with the normal to dA . This equivalent surface emission arises from the volume within the annuli contained within the projection of $d\omega$ back through dA . Some of the radiated energy will be absorbed by other annuli along the path and some will escape the arc column entirely. The radiant interchange between every possible pair of annuli was computed, taking into account the optical depth of the absorption path between the annuli. After appropriate summations, which are a massive sorting and summing job ideally suited for a digital computer, the result is net emission for each annulus. The fact that not all transmission paths intersect all annuli results in the absence of some terms, but these were taken care of in the scheme for indexing the summation loops of computer program ARCRAD IIIb.

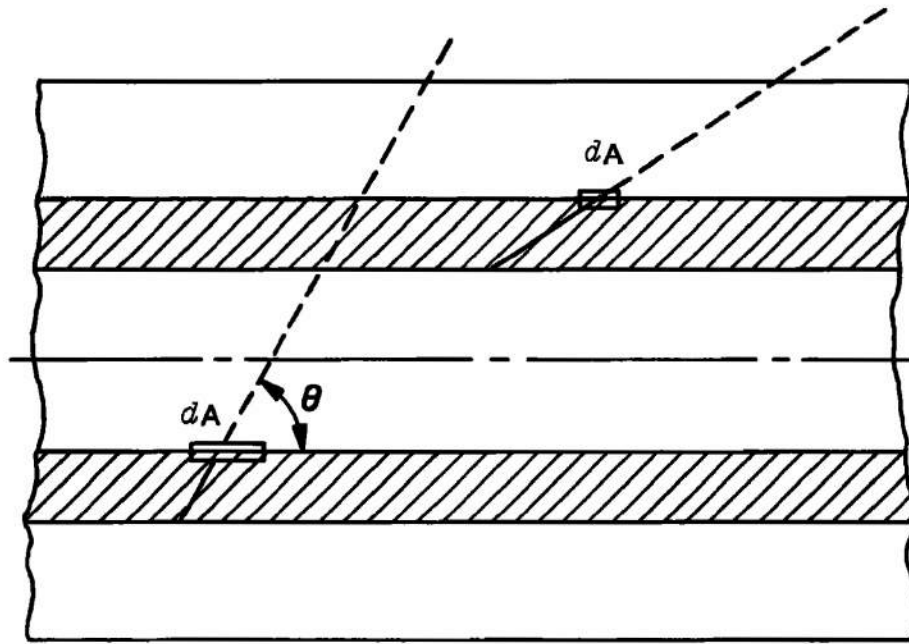
This program is essentially the same as ARCRAD III, which was presented in detail in the previous report, except that:

- (1) To meet the requirements of a new computer system (GE 635), several large entities within the main program were separated out as subroutines.
- (2) A minor refinement was made to the calorimeter integral calculation to account for the slight variation of effective view factor with angle in a plane normal to the arc centerline.

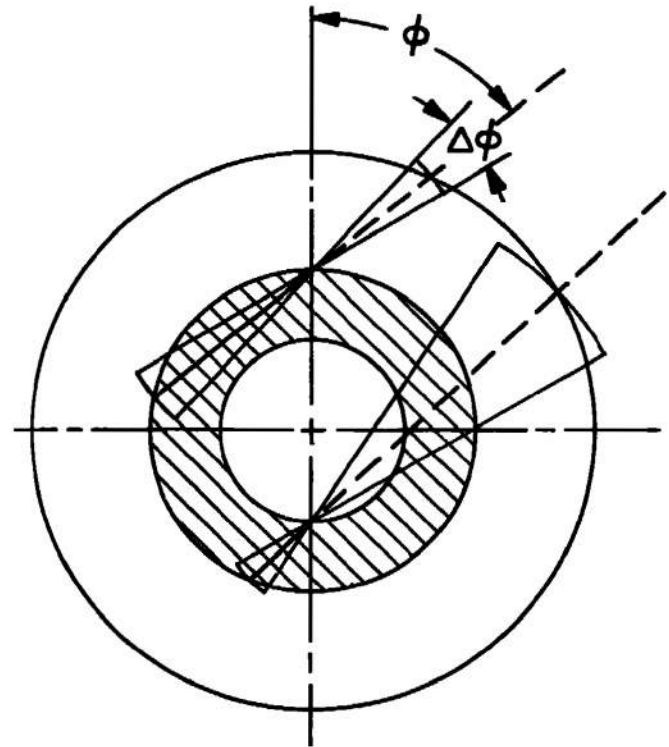


(A) AREA ELEMENT AND SOLID ANGLE

———— EMISSION, INCLUDING SELF-ABSORPTION
 - - - - TRANSMISSION - ABSORPTION



(B) SIDE VIEW, SECTION



(C) END VIEW

Figure 1. Radiant Interchange Model

(3) A capability for computing spectral line emission was added. .

B. SPECTRAL LINES

At the very high pressures which are of interest to us, the spectral lines are very much broadened and all but a few outstanding ones are submerged in the continuum. Some remain significant however, and to determine just how significant, a few which can be clearly distinguished experimentally and which are well known theoretically are chosen for exploration with program ARCRAD IIIb. Those chosen are shown in Table I; they include four hydrogen and two oxygen lines, the latter two being of just about the same importance whether the plasma is air or Delrin.

Spectral lines were accounted for as an addendum to the continuum calculation by taking, for each line, a band of wave numbers within which radiation from the line is significant, and subdividing that band*, centered about the nominal wave number of the line. Line broadening and shift are both temperature and density dependent so they must be computed separately for each annulus. Within each wave number subinterval, and for each annulus, the absorption coefficient including that due to the continuum for the line was calculated at the center of each wave number subinterval in the following way. Following Penner⁽¹²⁾, integrated absorption is given by

$$\int_{-\infty}^{+\infty} k \, dn = 2.375 \times 10^7 \left(\frac{N_{\ell}}{L_0} \right) (1 - e^{-v}) f_{\ell u} [\text{cm}^{-2}] \quad (1)$$

where N_{ℓ} is the number of atoms in the lower state of the transition, L_0 is the Loschmidt number, $f_{\ell u}$ is the oscillator strength, and the exponential accounts for stimulated emission. The assumption of LTE permits calculation of N_{ℓ} from the Boltzmann distribution, approximated as

$$N_{\ell} \cong \frac{g_{\ell} e^{-v_{\ell}}}{\sum_{i=1} g_i e^{-v_i}} \quad (2)$$

where g is statistical weight and $v = h\nu/k_B T$. The natural line profile was used so that the normalized probability distribution for emission in the wave number interval dn is given by

* The total number of subintervals cannot exceed the 71 intervals used for the continuum calculation.

$$J(|n - n_o|) dn = \frac{1}{\pi} \frac{(\Delta n)_{1/2} dn}{(n - (n_o - n_d))^2 + (\Delta n)_{1/2}^2} \quad (3)$$

The half-half-width $(\Delta n)_{1/2}$ is the wave number interval within which the line intensity decreases from its maximum value to one half its maximum value. It is tabulated, along with the line shift, n_d , by Griem⁽¹¹⁾ for many lines, including the oxygen lines in Table I. For hydrogen lines, $(\Delta n)_{1/2}$ was determined from published curves of hydrogen line intensity⁽¹³⁾.

The absorption coefficient due to continuum radiation (assumed constant and equal to its value at the nominal line center wave number) must also be added, so that we have, finally

$$k(n, T) = \left[\int_{-\infty}^{+\infty} k dn \right] J(n - n_o) + k_{\text{cont}}(T) \quad (4)$$

Having set up the absorption coefficients and wave number intervals, the calculation of radiation including a spectral line then proceeds in precisely the same fashion as the continuum previously computed. Any combination of the lines listed in Table I can be included in a computer run.

C. TWO ZONE MODEL

The lower temperature, outer part of the arc, contributes relatively little either to power dissipation or to radiant emission and the accurate determination of temperature profiles in the outer region is very difficult. For these reasons, the arc is divided into two zones, interior (Zone I) and exterior (Zone II). In Zone I, once the temperature profile has been established, as discussed below, the annulus boundaries are so determined that the weighted average temperature of each annulus is a multiple of 1000°K. This procedure results in a representative but tractable number of annuli and eliminates the need for temperature interpolation of absorption coefficient data. In Zone II, the profile was assumed linear, in 1000°K increments down to 1000°K. In the outer layers, radiant emission is very small but absorption is strong enough to prevent vacuum UV radiation from reaching the wall.

Program ARCRAD IIIb was set up to use a temperature profile of the form

$$(T - T_A)/(T_{\text{CL}} - T_A) = 1 - (r/r_A)^x \quad (5)$$

because the fullness of the profile is then governed by a single parameter x , and the symmetry condition at the centerline is satisfied for any $x > 1$. Best fit to a particular temperature profile (in the least squares sense) is obtained if T_{CL} and T_A are also optimized. The standard least squares procedure⁽¹⁶⁾ leads to three simultaneous non-linear equations in x , T_{CL} and T_A which are difficult to solve. However, at fixed T_A there are only two equations,

Table I: Spectral Lines Included in ARCRAD IIIb

Line	λ_o (Å)	n_o (cm ⁻¹)	Half-half Width (Refs. 11 and 13)			Lower Energy Level (Ref. 14) (cm ⁻¹)	Oscillator Strength (Ref. 15) ---
			(Å)				
			10,000°K	20,000°K	40,000°K		
L _α	1215	82259	0.00676	0.00676	0.00676	0	0.4162
L _β	1025	97492	0.0121	0.0121	0.0121	0	0.0791
H _α	6562	15237	0.871	0.871	0.871	82,259	0.6407
H _β	4861	20570	4.76	4.76	4.76	82,259	0.1193
O ₇₇₇	7773	12864	0.0327	0.0443	0.566	73,768	0.922
O ₈₄₅	8445	11839	0.0528	0.0708	0.0895	76,795	0.898

both of which can be solved for dimensionless T_{CL} as a function of x . If $\theta_i = (T_i - T_A)/T_A$, and the temperature is tabulated for m values of radius, these equations are

$$\theta_{CL} = \frac{\sum_{i=1}^m \theta_i [1 - (r_i/r_A)^x]}{\sum_{i=1}^m [1 - (r_i/r_A)^x]^2} \quad (6)$$

$$\theta_{CL} = \frac{\sum_{i=1}^m \theta_i (r_i/r_A)^x \ln(r_i/r_A)}{\sum_{i=1}^m (r_i/r_A)^x (\ln r_i/r_A) [1 - (r_i/r_A)^x]} \quad (7)$$

A computer program providing automatic successive trial values and linear interpolation in the neighborhood of the solution led to rapid convergence. Repetition for several values of T_A gave the required fit.

D. TEMPERATURE PROFILES FROM NON-OPTICALLY THIN ARCS

Determination of arc temperature from measurements of continuum intensity depends on an Abel inversion (Appendix I) of a series of intensity measurements along a line of sight at successive increments of displacement, x , from the cylindrical axis of symmetry. When the plasma is optically thin (negligible self-absorption), the conventional Abel inversion converts intensities, $I(x)$ to local emission coefficients $i(r)$, which can then be related to temperatures, assuming local thermodynamic equilibrium, if continuum absorption coefficients are available (see Section III).

$$i(r) = k L \left(\frac{c_1}{c_2} \right)^{5/5} (T^5) \left(\frac{v^5}{e^v - 1} \right) ; (k L \ll 1) \quad (8)$$

Note that c_1 and c_2 are the Planck radiation constants and, again, $v = h\nu/k_B T$.

The method described herein is based on use of the Abel inversion integral in an iterative way suggested by Griem⁽¹¹⁾. Successive approximations to $I^*(x)$, the intensity which would have been observed if no absorption had taken place, are computed with measured intensities used as an initial approximation to $I^*(x)$. Inversion yields emission coefficients and hence a temperature distribution which can be used to determine local absorption. Abel integration, Appendix I, can then be applied to compute approximations to both $I^*(x)$ and $I(x)$.

If $I(x)$ has been computed from the correct $I^*(x)$, it will match the observed $I(x)$. In general, the observed and computed values will not match, so a new approximation to $I^*(x)$ is obtained by multiplying each current local $I^*(x)$ by the ratio of observed to computed local $I(x)$.

Optical depth is found by an Abel integration along the line of sight of the form of Equation 6, Appendix I.

$$\tau(x) = 2 \int_x^{r_0} \frac{i(r) r dr}{I_T \sqrt{r^2 - x^2}} \quad (9)$$

The Planck function, I_T , is known because temperature has been determined from $i(r)$. Because $i(r)$ and I_T are known only at discrete points, the integration must be numerical, as discussed in detail in Appendix I.

Cremers⁽¹⁷⁾ procedure for performing the Abel inversion was followed. The plasma radius is divided into zones of equal size and a polynomial is fitted to the data in each zone by the method of least squares⁽¹⁶⁾. Details of this process are also given in Appendix I and the computer programs developed to carry it out are discussed in Appendix II.

SECTION III

COMPUTATION OF/WITH DELRIN PROPERTIES

To study electric arc behavior one must first have an arc that is well defined and will hold steady long enough to be photographed; in addition, the analysis requires cylindrical symmetry. The practical aspects of achieving this experimentally are discussed in Section V, but, briefly, the most effective method we have found is stabilization by ablation from a constrictor tube made of an organic plastic. The obvious drawback is that we are then limited to a plasma composed of the ablation products, but this is not serious if the ablation is clean and uniform, and if the plasma constituents are known.

An ideal material for the purpose is Delrin, a material which is pure polyformaldehyde $(H_2CO)_n$, except for less than 0.5 percent anti-oxidants containing C, H, N and O; according to the Philadelphia Product Information office of the DuPont Chemical Company. With the basic chemical composition known, it was then possible to develop tables of plasma properties for use in subsequent analyses. Since the plasma is highly ionized, and the phenomena of interest are closely associated with free electrons, no qualitative and little quantitative difference is expected from behavior of arc plasma.

A. THERMODYNAMIC PROPERTIES OF DELRIN

Thermodynamic properties were computed by Browne using a program already developed and previously applied to air and other plasmas. The remainder of this subsection quotes from a report (18) written about the air plasma work:

"The procedure which is followed . . . is to generate a set of ideal gas thermal functions, that is, enthalpy, free energy and specific heat, for each of the species of interest in the system. The list of constituents treated in these studies include the various atoms, atomic ions, diatoms, diatomic ions, polyatomic molecules and the electron. In addition to the thermal functions of each specie, the heat of formation is required. The heat of formation data is often inferred from thermochemical, spectroscopic or ionization potential measurements. The equilibrium composition of the mixture is found by effectively minimizing the Gibbs free energy given any two state variables which describe the thermodynamic state of the system. The mixture calculations are predicted on the absence of forces between charged species. Knowing the equilibrium composition, the thermodynamic properties of the mixture, namely, enthalpy, entropy, etc., can then be readily determined

"The calculation procedure . . . involved the evaluation of the translational and electron partition functions and their contribution to the thermal functions. The electronic energy level summation was extended over all energy levels up to and

beyond the ionization level as tabled in Moore ⁽¹⁴⁾. This procedure has been demonstrated to yield essentially the same thermodynamic properties for atoms and atomic ions at temperatures below 15,000°K, as predicted by using one of the more exact electronic cutoff procedures ⁽¹⁹⁾.

"The ideal gas thermal functions and thermodynamic properties of diatoms and diatomic ions constitute a composite of low and high temperature calculations. The low temperature calculations were based on the rigid rotator-harmonic oscillator approximations with centrifugal stretching and vibrational anharmonicity corrections included. The high temperature calculations are based on the virial methodology. Here the classical second virial coefficient is evaluated using the Morse potential. The second virial coefficient, in conjunction with its first and second temperature derivative is, in turn, related to the thermal functions of the diatom through the partition function. The polyatomic molecular thermodynamic properties are based on the rigid rotator-harmonic oscillator approximation

"The mixture equilibrium composition calculation procedure is the well-known Brinkley method ⁽²⁰⁾ in which the mixture is considered to be composed of ideal gases without charge interaction. The system of algebraic equations expressing the free energy constraints is solved along with the atomic conservation statements by use of the Newton-Raphson technique"

Results of the thermodynamic equilibrium calculations are presented as thermodynamic state, Figure 2, and composition as a function of temperature and pressure, Figures 3a-3d. Individual species concentrations were also available for use in the determination of radiation absorption coefficients.

B. TRANSPORT PROPERTIES

An examination of published values of transport properties for several types of plasmas indicated that results for several different plasmas above 15,000°K by one author tended to differ about as much or sometimes less than results for the same plasma from different authors ⁽²¹⁻²³⁾. The correlations of Weber ⁽²⁴⁾ which have previously been applied to the air plasma were therefore also used for Delrin in ARCRAD IIIb.

C. RADIATION DATA

In computing absorption coefficients for continuum radiation, radiative processes taken into account were: free-bound deionization of singly ionized H, C, and O; photodetachment of electrons from the negative ions H⁻, C⁻, and O⁻, and free-free radiation (Bremstrahlung). These were considered to be the primary processes since peak arc temperatures are of the order of 20,000°K where these species predominate. Below 10,000°K an enormously complex

system of molecular band radiation exists* but, as long as the plasma layer at these temperatures is not optically thick, the radiant intensity effect is negligible. For this reason only the O₂ Schumann-Runge system was included as a sample. As is the case for air, molecular absorption of vacuum ultraviolet radiation is an important process at low temperatures since this serves to prevent such radiation from reaching the arc column boundary.

Sources and methods are summarized below.

a. H Free Bound

For the hydrogen atom a direct calculation of the deionization continuum is possible (12, 26) Expressed as an absorption cross-section the equation is

$$\sigma_H = \left[\frac{32 \pi^2 e^6 Ry \exp(-x_1) K_{mks}^3}{3\sqrt{3} h^3 c^3 n^3} \right] \times \left[\sum_{n_i < n}^{x_{10}} \frac{\exp(x_i)}{i^3} + \frac{\exp(x_{11} - 1)}{2x_1} \right] (\text{cm}^2) \quad (10)$$

where Ry is the Rydberg constant and

$$x_1 = \frac{h c Ry}{k_B} \quad (11)$$

$$x_i = \frac{x_1}{i^2} \quad (12)$$

$$n_i = \frac{Ry}{i^2} \quad (13)$$

b. O and C free bound

The quantum-defect method of Burgess and Seaton (27) was used by Sherman and Kulander to compute cross sections for radiative recombination (absorption coefficient per particle, in cm²) of several species including O (28) and C (29). Typical cross sections are shown in Figure 4. Although values were available only to 20,000^o K, they change very slowly

* Main and Bauer (25) list 44 different systems involving C, H, and O.

with temperature, so a second-order LaGrange interpolation was used to extrapolate to 25,000°K based on values at 16,000°, 18,000°, and 20,000°K.

c. H⁻

Radiation associated with the negative hydrogen ion has been the subject of considerable interest to astrophysicists for many years. Chandrasekhar (30, 31) gives a curve (Figure 5a) for the cross section for deionization and a tabulation of both free-free and free-bound radiation as a function of temperature. His table of the absorption coefficient per neutral hydrogen atom and per unit electron pressure for free-free radiation associated with the negative hydrogen ion was found to be well represented by a double logarithmic interpolation of selected values (Table II).

Table II. Selected Values of \hat{k} (31)

Wave Number (cm ⁻¹)	$\theta = 5040/T$ (°K)	
	2	0.5
2000	8.4×10^{-25}	3.6×10^{-25}
8000	4.12×10^{-26}	8.9×10^{-27}
20000	8.9×10^{-27}	1.27×10^{-27}

The quantity \hat{k} is defined as absorption coefficient per neutral hydrogen atom and per unit electron pressure (atm), ($1500 \text{ cm}^{-1} < n < 25,000 \text{ cm}^{-1}$). Linear absorption coefficient is then given by

$$k_{\text{ff}, \text{H}^-} = \left[\hat{k} (N_{\text{H}}) \right] \left(\frac{N_{\text{e}}}{L_0} \right) \left(\frac{\rho}{\rho_0} \right) \left(\frac{T}{T_0} \right) \times 1.013 \times 10^6 \text{ (cm}^{-1}\text{)} \quad (14)$$

d. C⁻

Cross sections have been calculated both by Breene (32) and by Kulander and Sherman (28). The latter's values were used. They are based on the quantum defect method and are more than an order of magnitude larger (Figure 5b).

e. O⁻

Cross sections have been measured by Branscome *et al* (33) up to about 3 ev (24,000 cm⁻¹). Above that wave number the procedure of Meyerott as discussed in Penner (12) was followed, with the constants adjusted to fit Branscome's more recent measurements (Figure 5a).

f. Bremsstrahlung

The Kramers- Unsöld equation was used, with Gaunt factor and ion charge both at unity⁽³⁴⁾.

$$k_{\text{ff}} = \frac{3.708 \times 10^8}{c^3 n^3 \sqrt{T}} (1 - e^{-v}) N_e \left(\sum_i N_i \right) \quad i = C^+, H^+, O^+ \quad (15)$$

g. O₂ Schumann-Runge

Data were taken from curves for spectral radiance J(watt/cm³-str-Å) published by Breen and Nardone⁽³⁵⁾ and converted to absorption coefficients.

h. Vacuum UV Molecular Absorption

The predominant molecular species in Delrin plasma are H₂O, CO, CO₂, and CH₄. Absorption by these species was accounted for by averaging the experimental data collected by Schultze, et al⁽³⁶⁾.

Line radiation absorption coefficients are discussed in Section II part B, with key data shown in Table I.

Figures 6a-6e show continuum spectral radiance of Delrin at atmospheric density and at 5000^o K temperature increments. The graphs are computer plotted for a 1 millimeter thick slab and show the individual species, total spectral radiance and the black body limiting curve. As expected, the Bremsstrahlung and deionization continua are dominant and the vacuum ultraviolet region is nearly black body even at low temperature.

D. COMPUTATION SUMMARY

The block diagram, Figure 7, summarizes the computations performed on this project. The absorption coefficients and thermodynamic data already discussed were inputs to program ARCRAD IIIb. They were also the source for calculations of emission coefficient as a function of temperature at a specified wave number, to be used in the temperature profile measurements discussed in Section IID and part C of Appendix II.

Figure 8 shows typical emission coefficient behavior. At the infrared wavelength chosen, Bremsstrahlung and H_{fb} radiation are dominant, as can be seen from the dashed curve on the figure which was calculated directly from Equations 10 and 15.

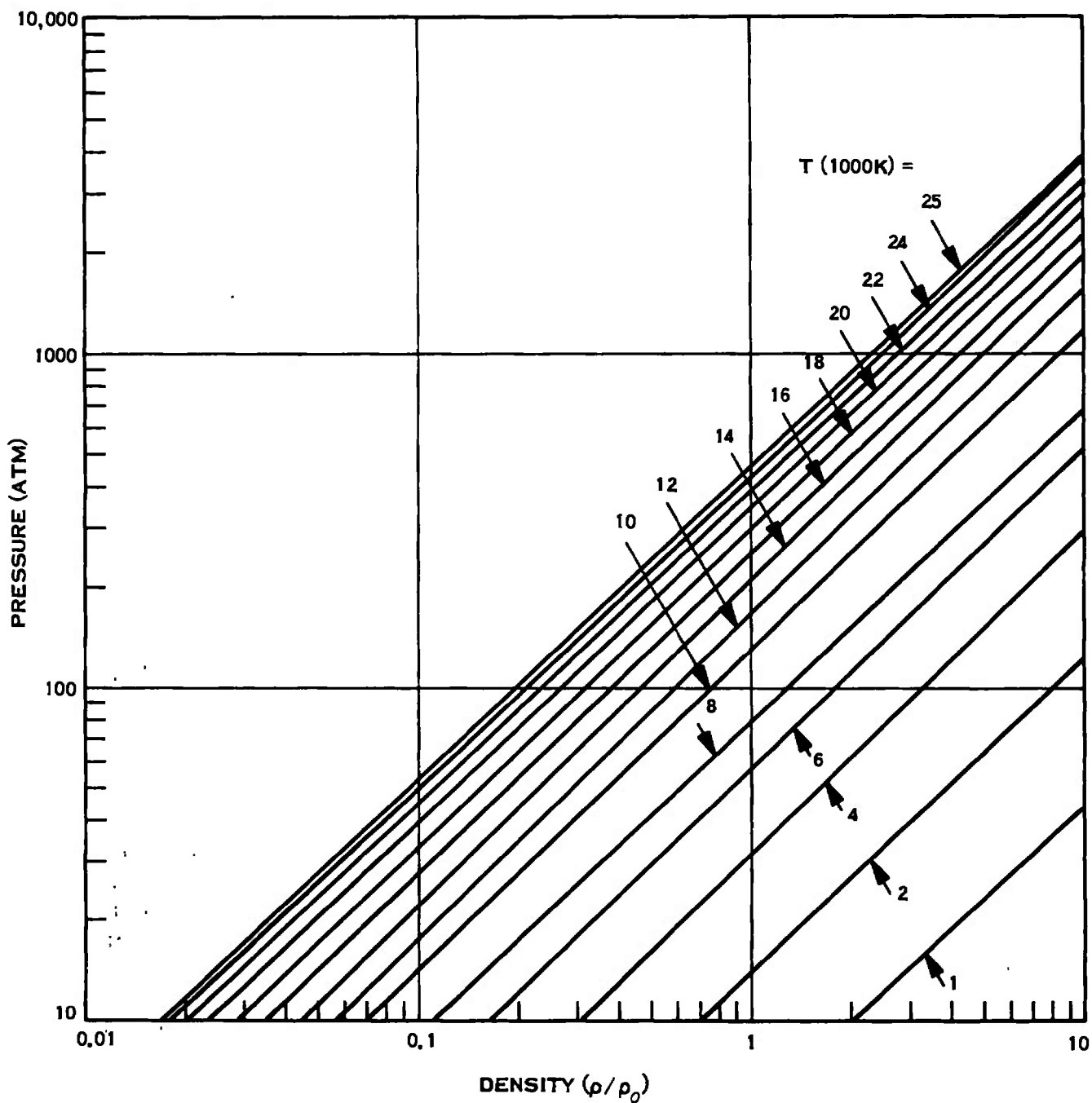


Figure 2. Delrin Equilibrium Thermodynamic State

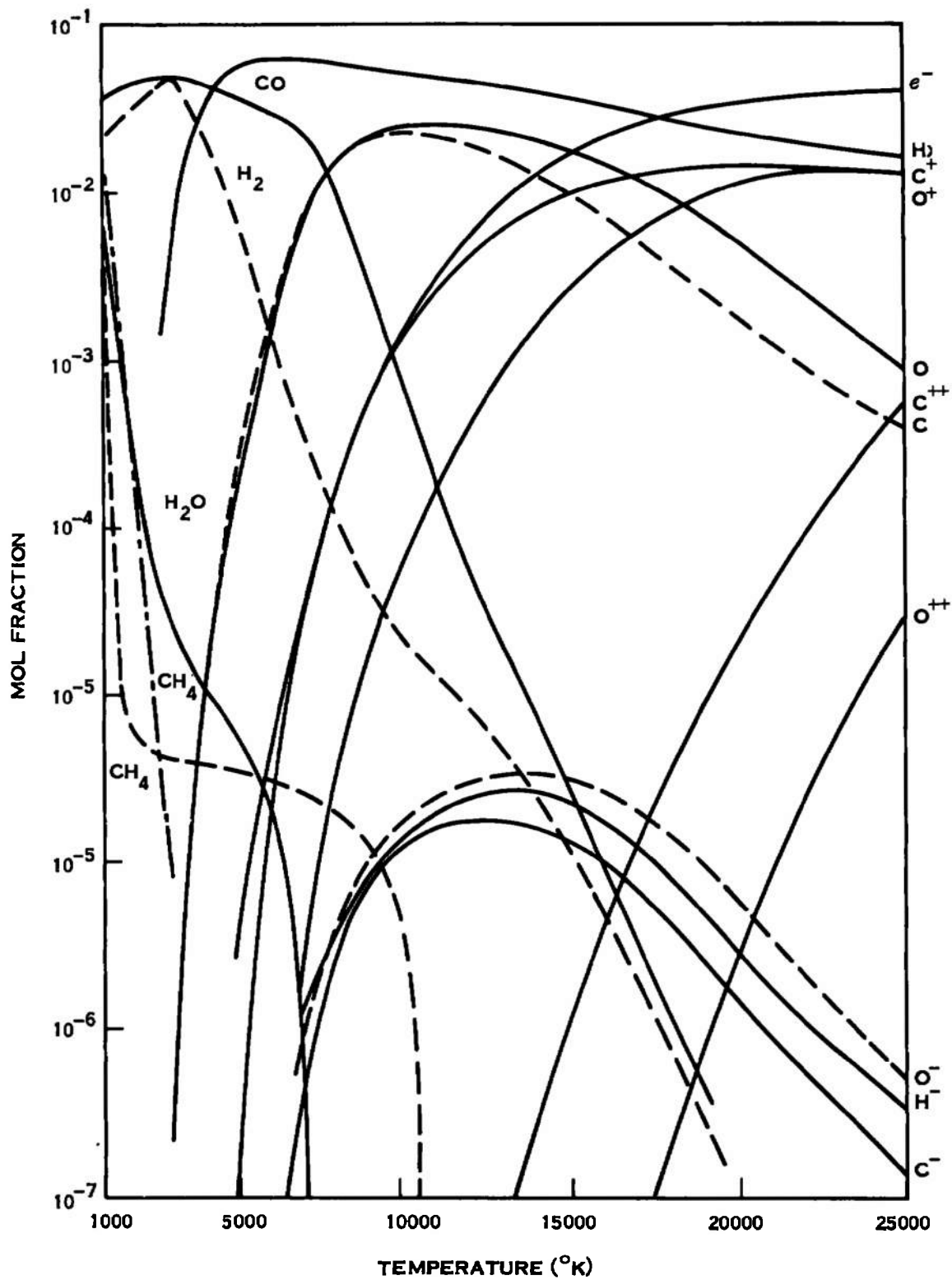


Figure 3a. Delrin Composition, P = 10 atm

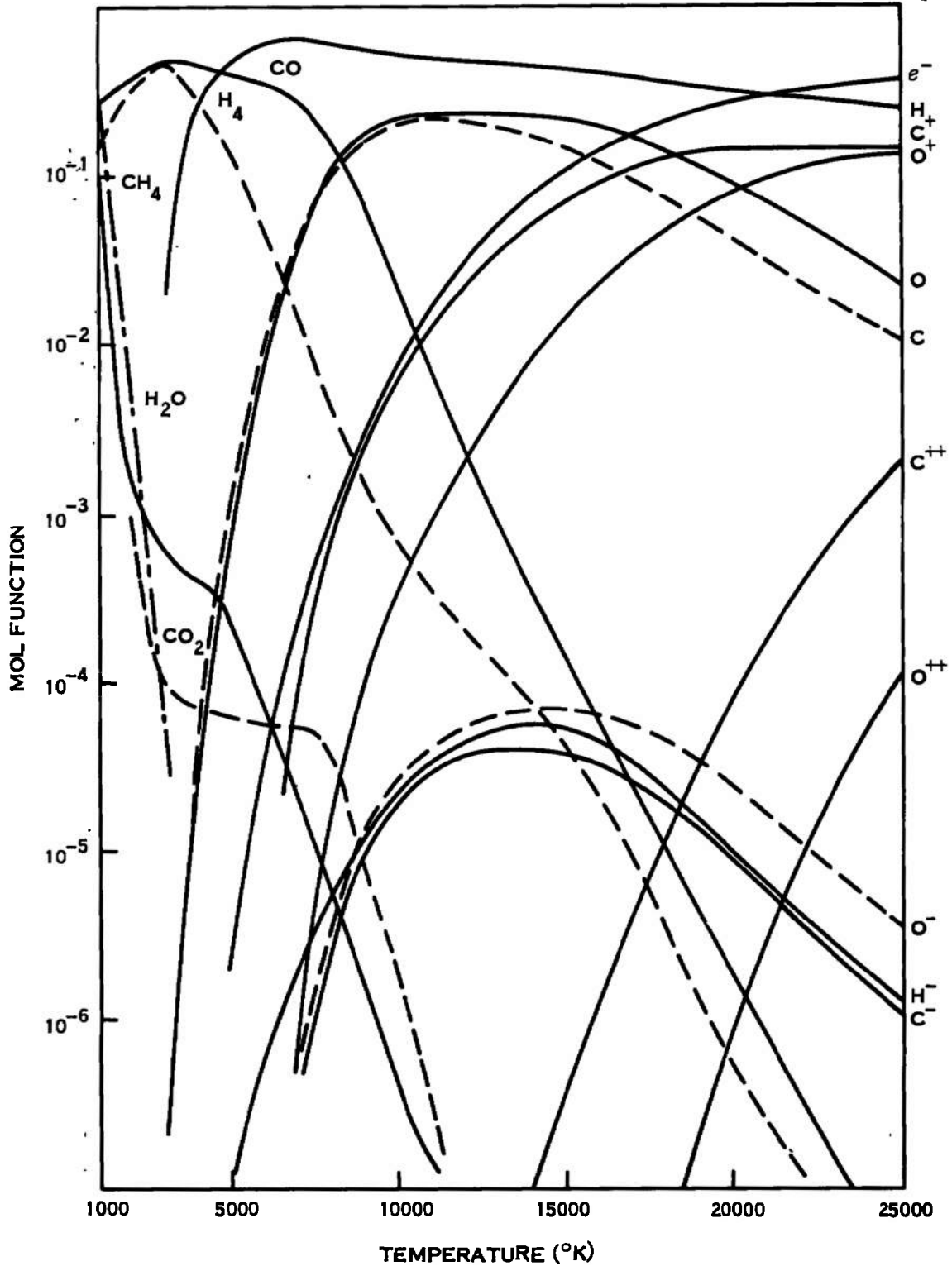


Figure 3b. Delrin Composition, P = 30 atm

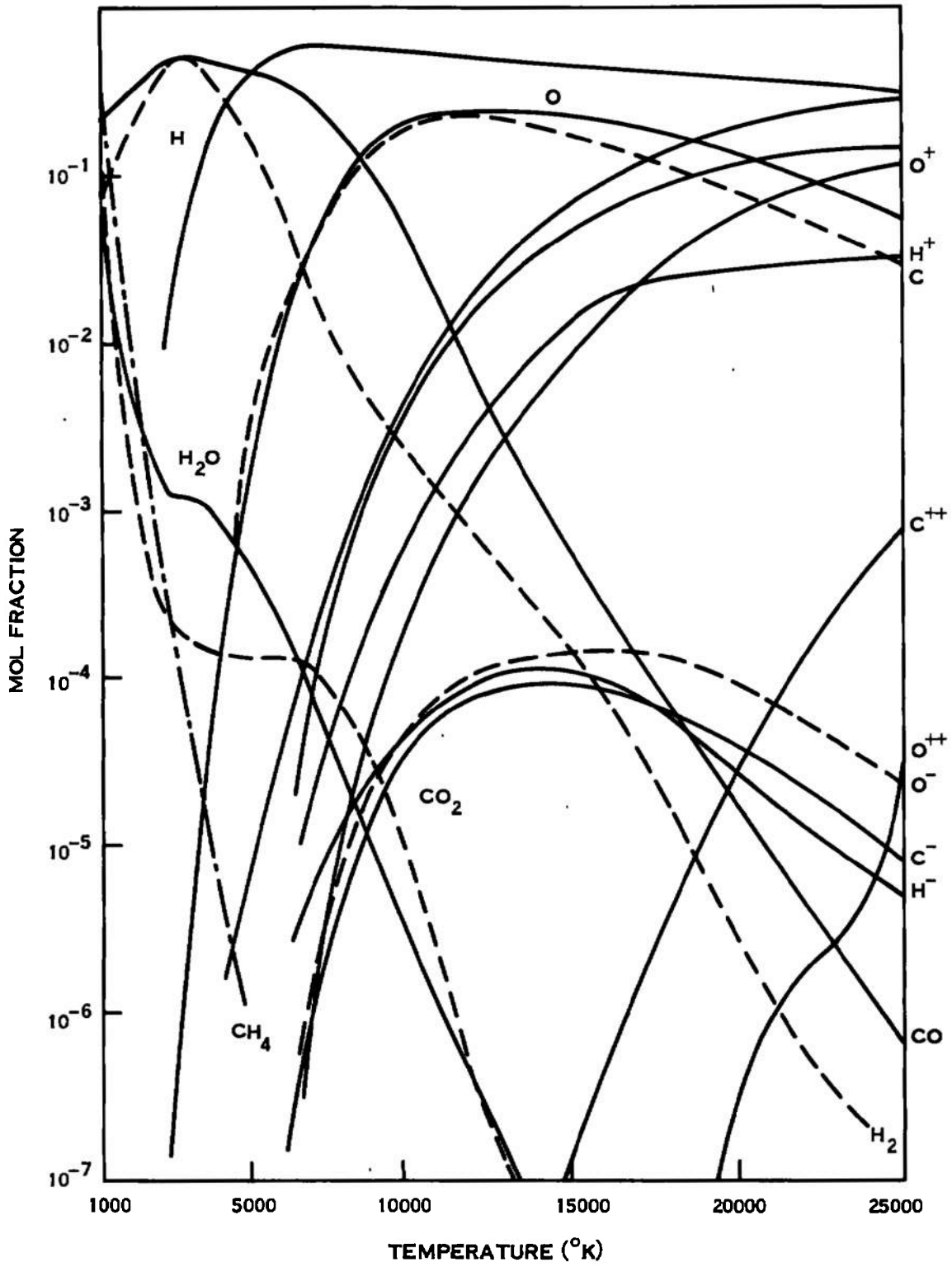


Figure 3c. Delrin Composition, P = 100 atm

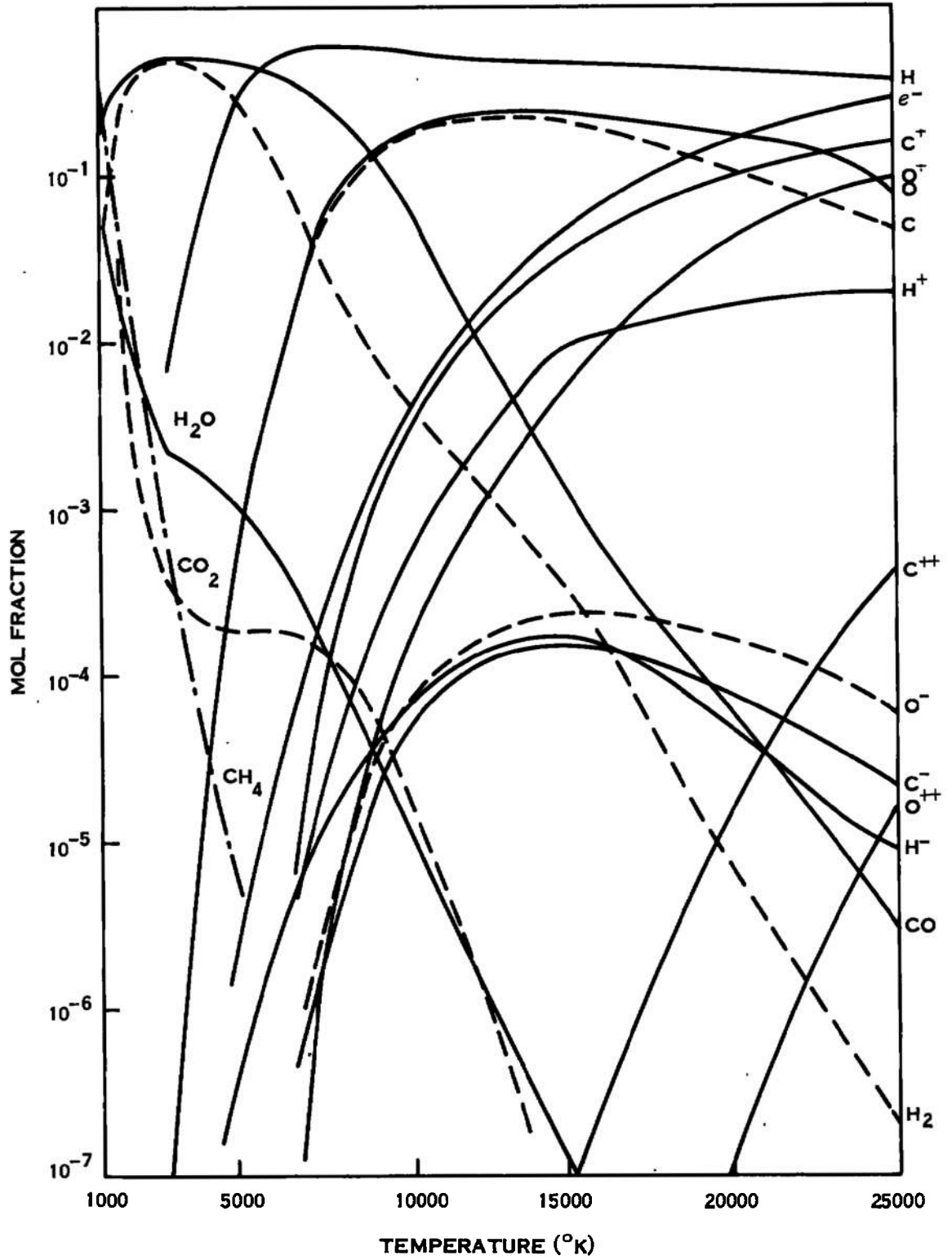


Figure 3d. Delrin Composition, P = 200 atm

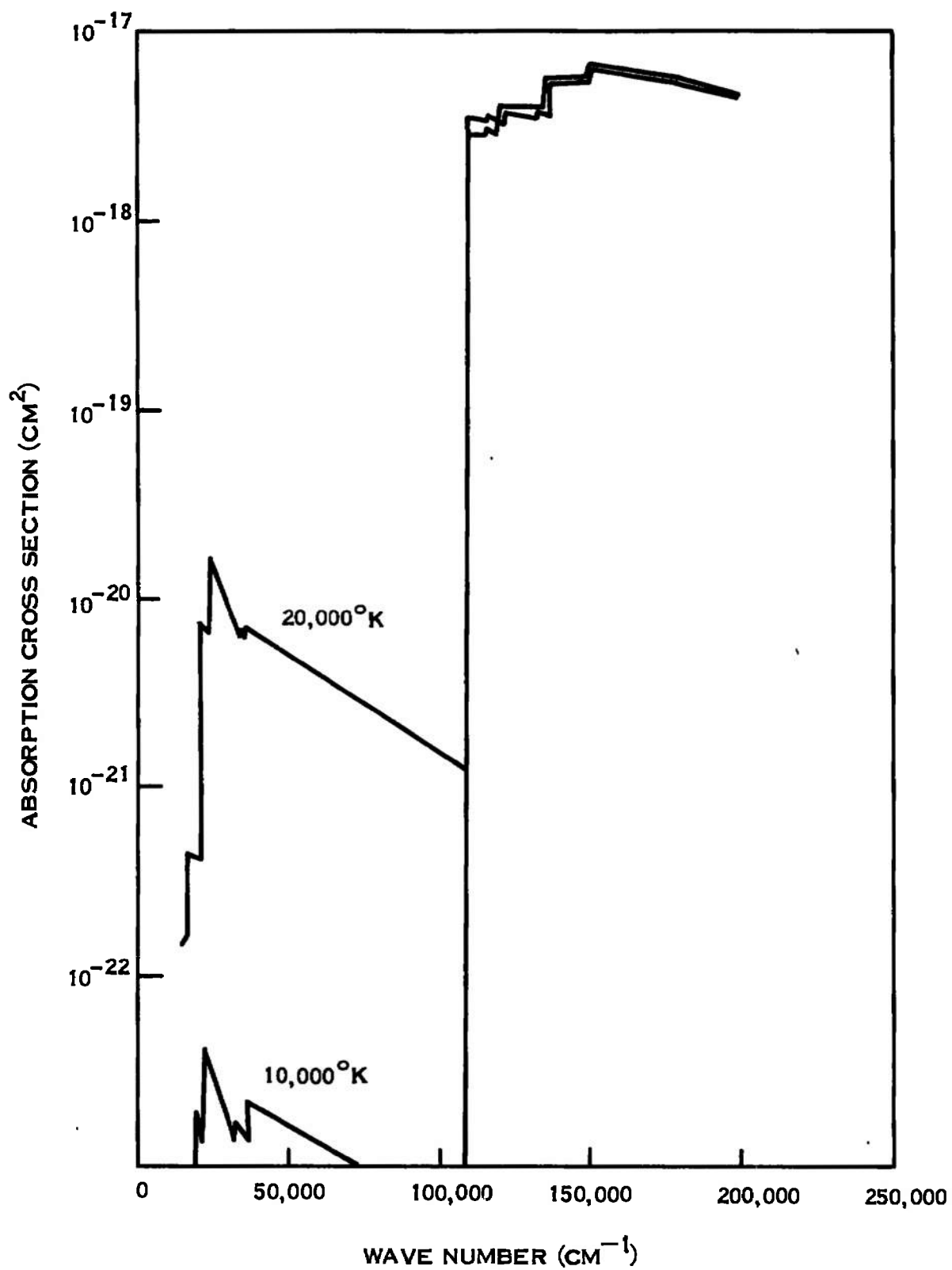


Figure 4a. Oxygen Deionization Absorption Cross Section

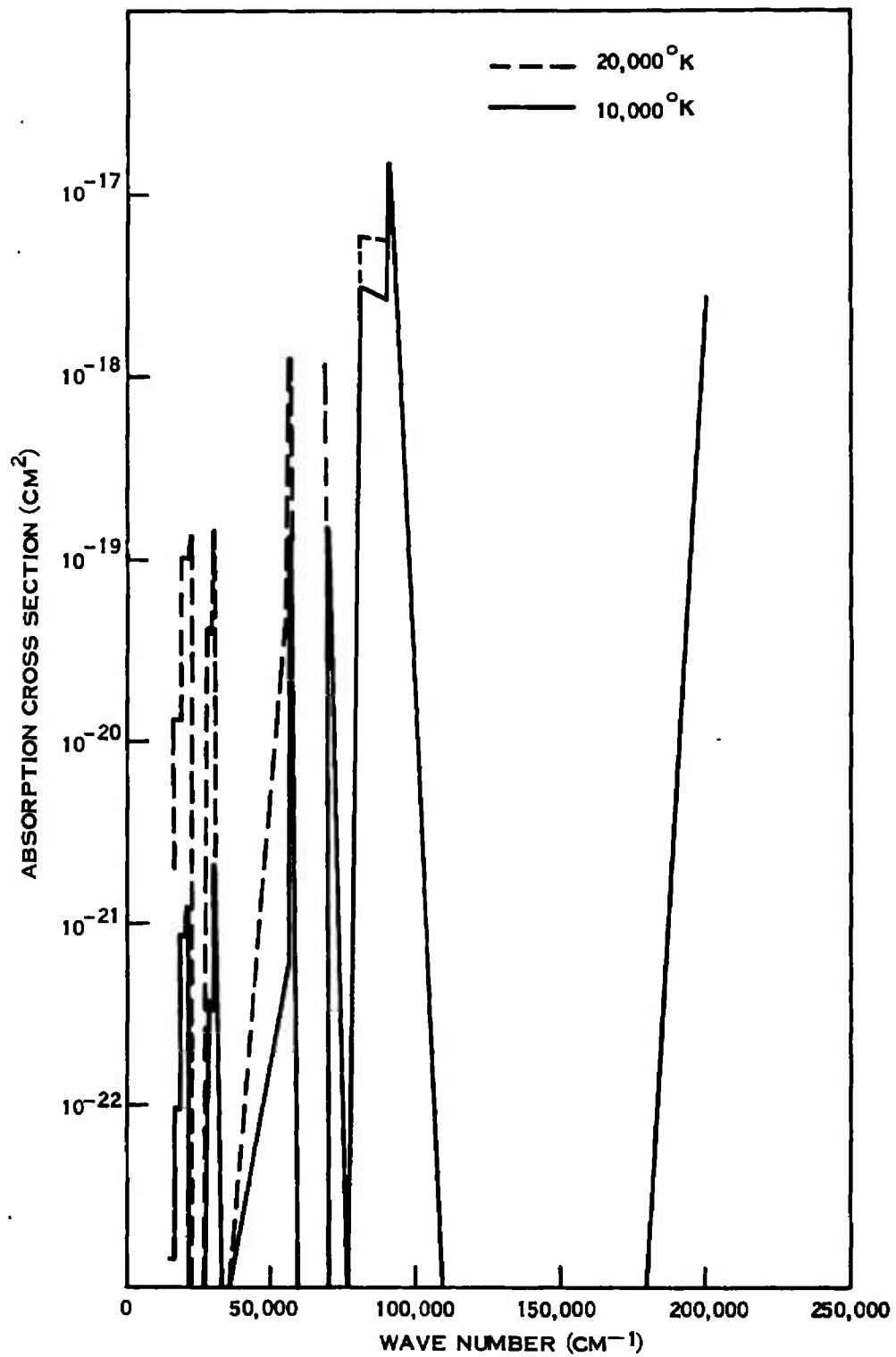


Figure 4b. Carbon Deionization Absorption Cross Section

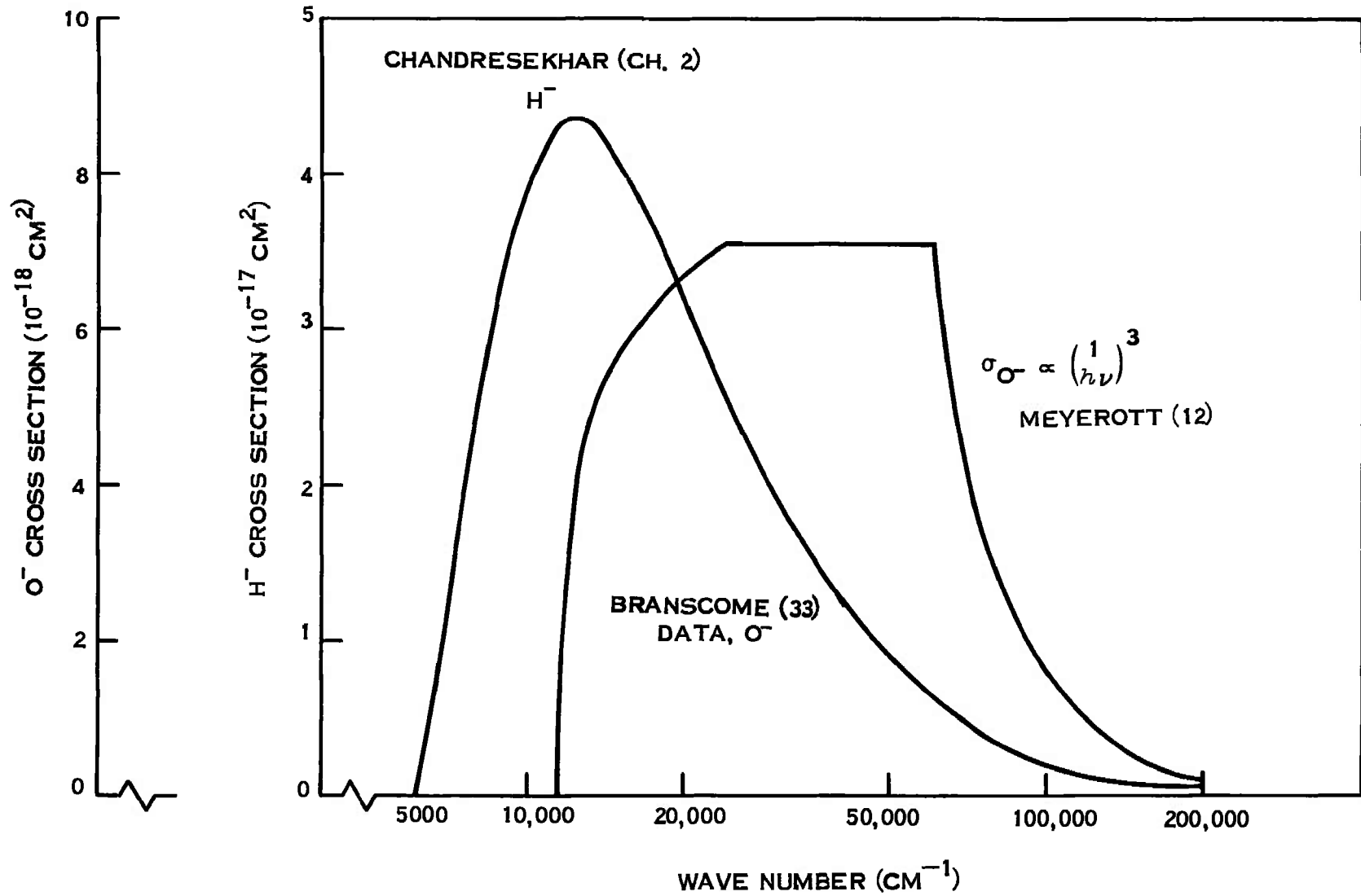


Figure 5a. Photoionization Cross-Section, H^- and O^-

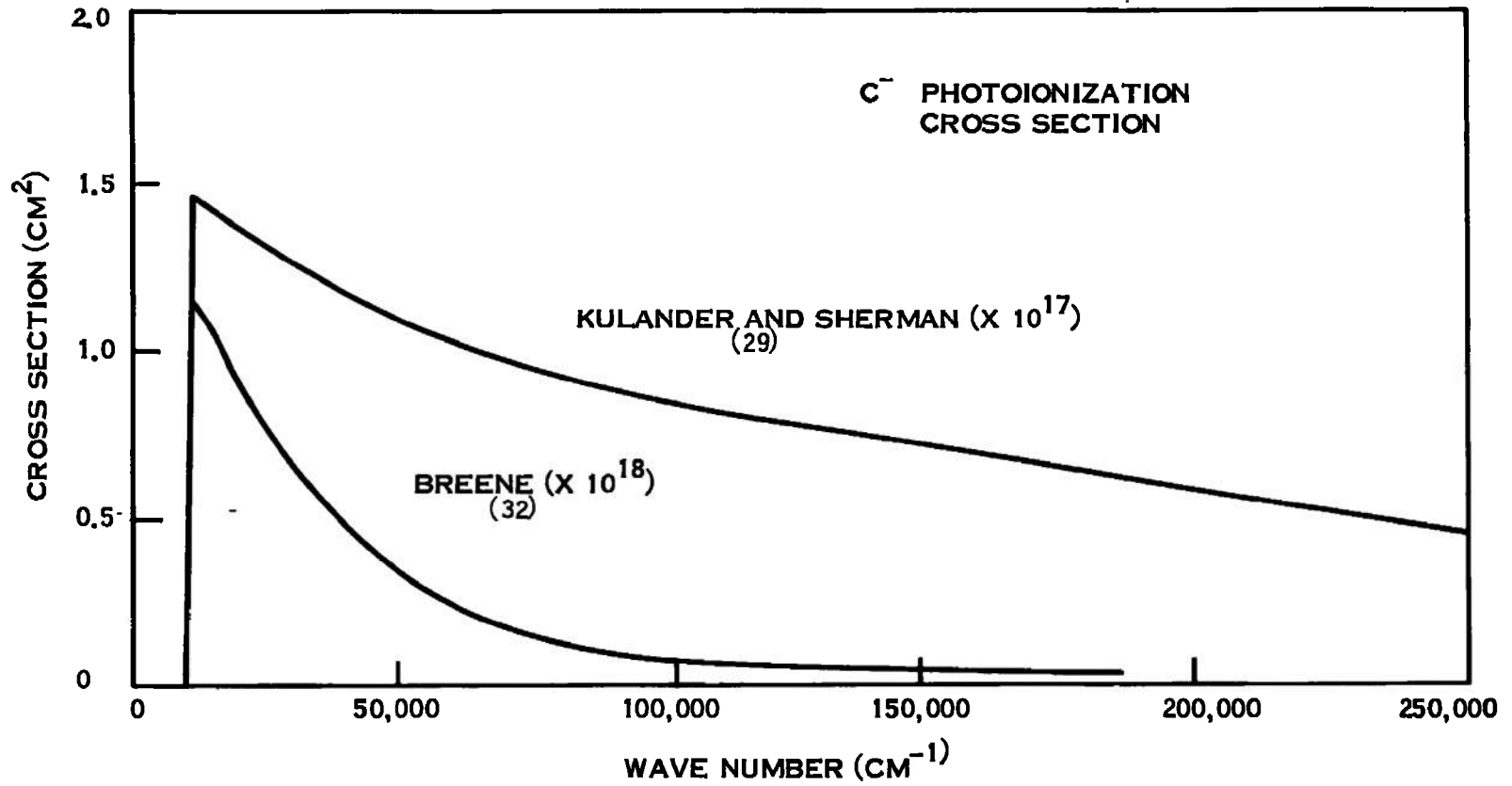
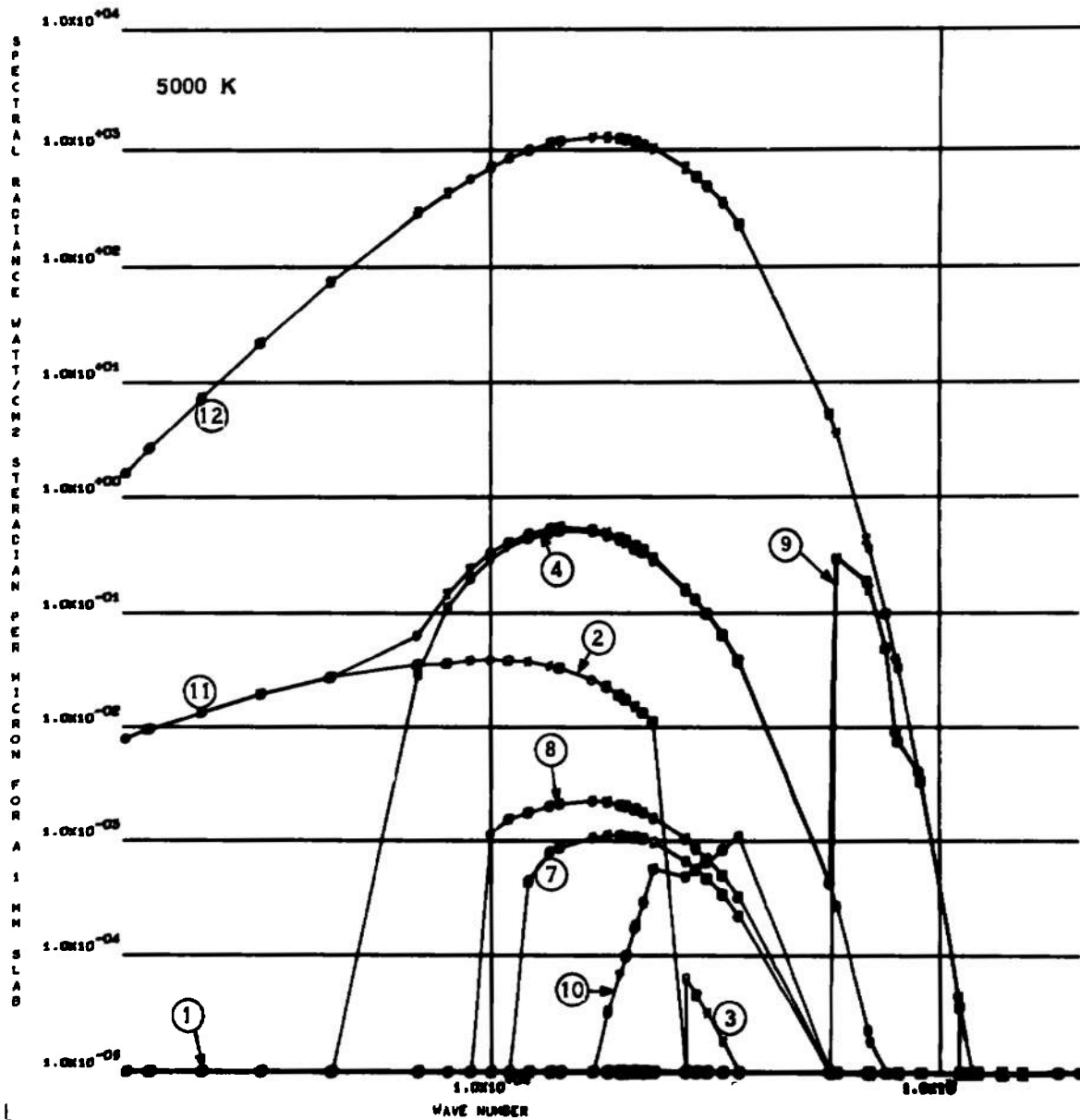
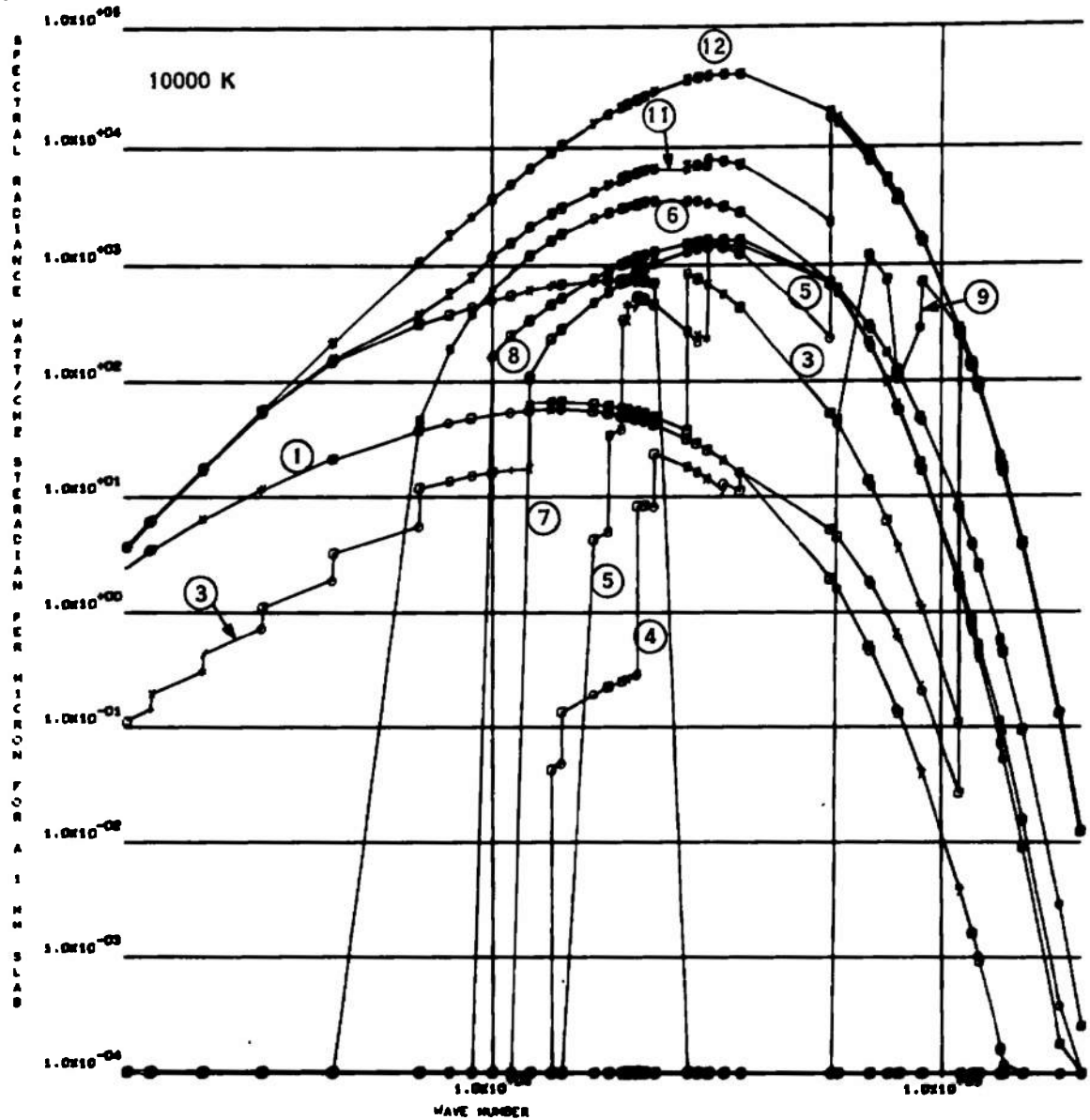


Figure 5b. Photoionization Cross Section, C⁻, Two Sources



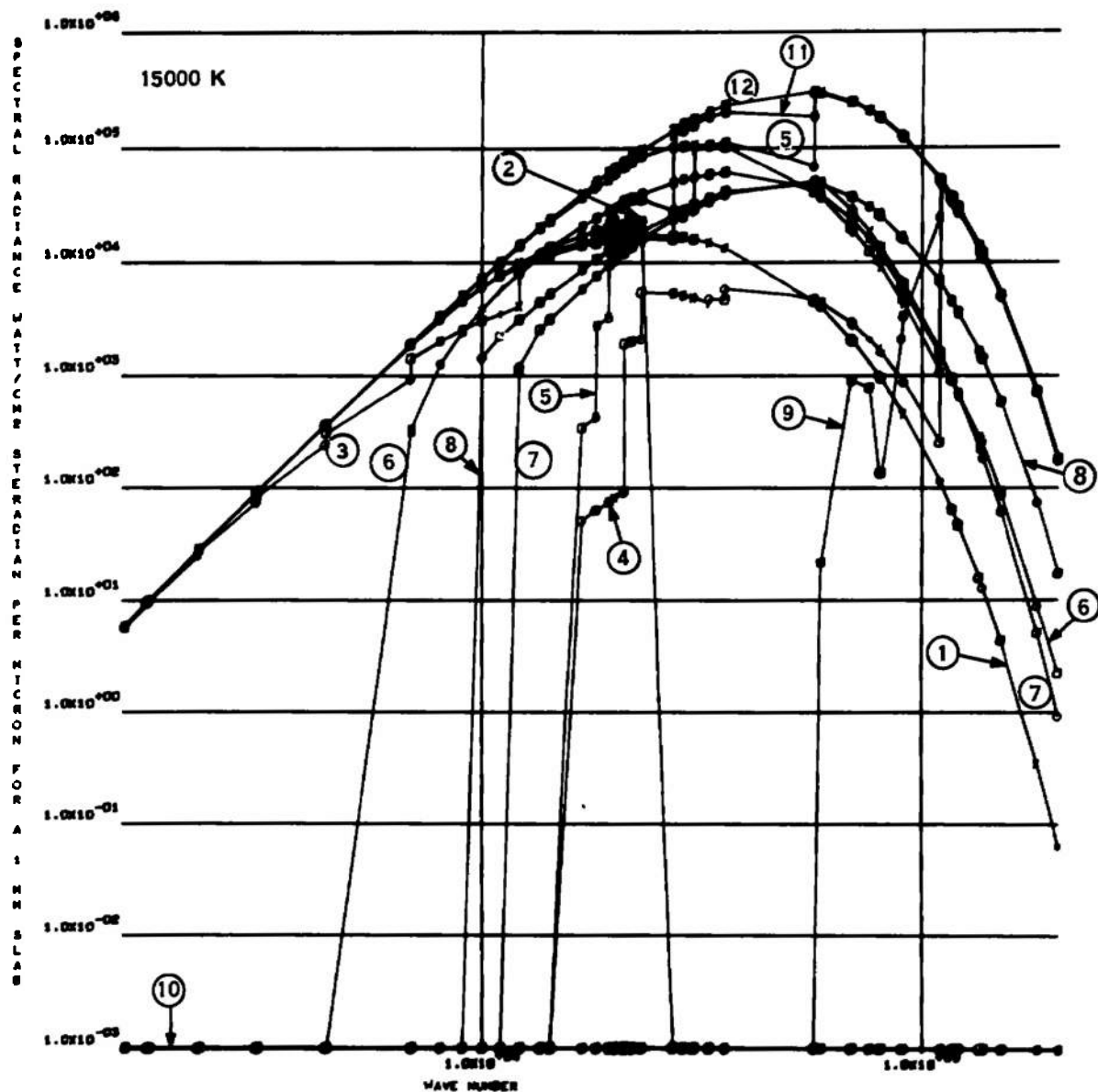
- | | | | |
|---|---------------------------|----|---------------------|
| 1 | BREMSSTRAHLUNG (EXCEPT H) | 7 | O^- |
| 2 | H^- FREE-FREE | 8 | C^- |
| 3 | H FREE-BOUND | 9 | VACUUM UV MOLECULAR |
| 4 | O FREE-BOUND | 10 | O (S-R) |
| 5 | C FREE-BOUND | 11 | ALL CONTRIBUTORS |
| 6 | H^- | 12 | BLACK BODY |

Figure 6a. Delrin Spectral Radiance, 1 mm Slab, $T = 5000^{\circ}K$, $\rho/\rho_0 = 1$



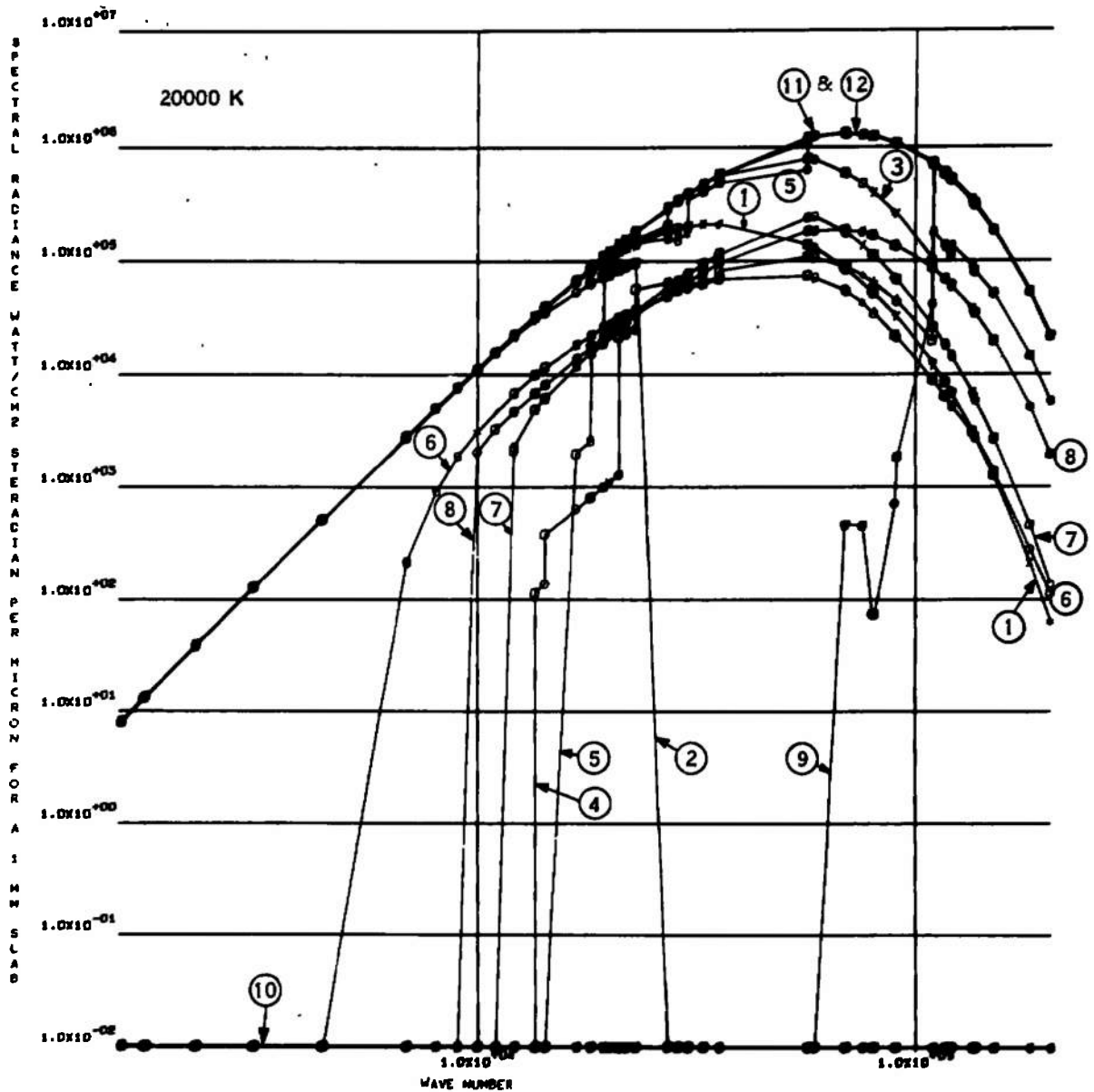
- | | | | |
|---|---------------------------|----|---------------------|
| 1 | BREMSSTRAHLUNG (EXCEPT H) | 7 | O^- |
| 2 | H^- FREE-FREE | 8 | C^- |
| 3 | H FREE-BOUND | 9 | VACUUM UV MOLECULAR |
| 4 | O FREE-BOUND | 10 | O (S-R) |
| 5 | C FREE-BOUND | 11 | ALL CONTRIBUTORS |
| 6 | H^- | 12 | BLACK BODY |

Figure 6b. Delrin Continuum Spectral Radiance, 1 mm Slab, $T = 10,000^{\circ}D$, $\rho/\rho_0 = 1$



- | | | | |
|---|---------------------------|----|---------------------|
| 1 | BREMSSTRAHLUNG (EXCEPT H) | 7 | O^- |
| 2 | H^- FREE-FREE | 8 | C^- |
| 3 | H FREE-BOUND | 9 | VACUUM UV MOLECULAR |
| 4 | O FREE-BOUND | 10 | O (S-R) |
| 5 | C FREE-BOUND | 11 | ALL CONTRIBUTORS |
| 6 | H^- | 12 | BLACK BODY |

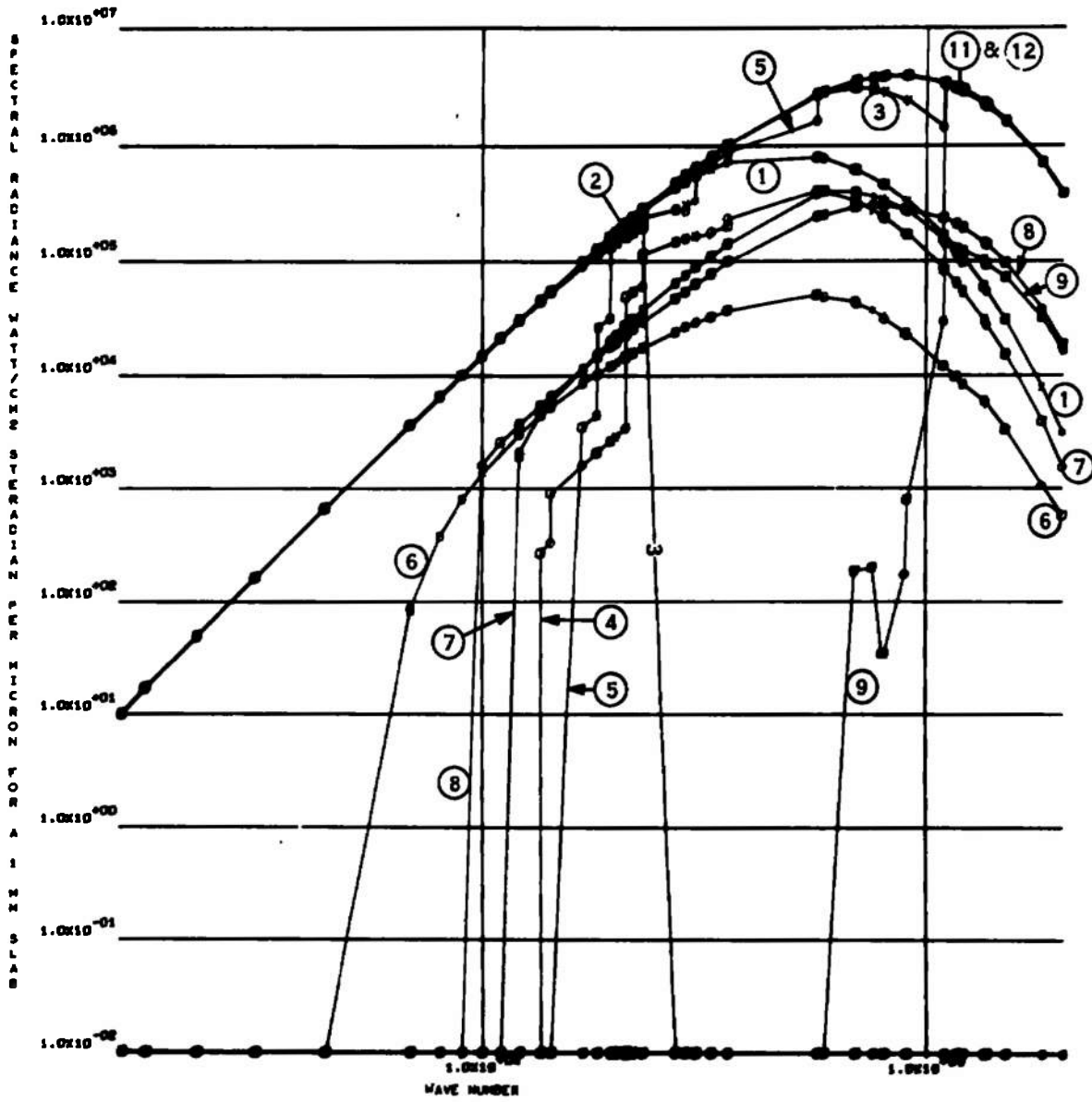
Figure 6c. Delrin Continuum Spectral Radiance, 1 mm Slab, $T = 15,000^{\circ}K$, $\rho/\rho_0 = 1$



- | | | | |
|---|---------------------------|----|---------------------|
| 1 | BREMSSTRAHLUNG (EXCEPT H) | 7 | O ⁻ |
| 2 | H ⁻ FREE-FREE | 8 | C ⁻ |
| 3 | H FREE-BOUND | 9 | VACUUM UV MOLECULAR |
| 4 | O FREE-BOUND | 10 | O (S-R) |
| 5 | C FREE-BOUND | 11 | ALL CONTRIBUTORS |
| 6 | H ⁻ | 12 | BLACK BODY |

Figure 6d. Delrin Continuum Spectral Radiance, 1 mm Slab, $T = 20,000^{\circ}\text{K}$ $\rho/\rho_0 = 1$

12/10/67



- | | |
|----------------------------------|-----------------------|
| 1 BREMSSTRAHLUNG (EXCEPT H^-) | 7 O^- |
| 2 H^- FREE-FREE | 8 C^- |
| 3 H FREE-BOUND | 9 VACUUM UV MOLECULAR |
| 4 O FREE-BOUND | 10 O (S-R) |
| 5 C FREE-BOUND | 11 ALL CONTRIBUTORS |
| 6 H^- | 12 BLACK BODY |

Figure 6e. Delrin Continuum Spectral Radiance, 1 mm Slab, $T = 25,000^\circ K$ $\rho/\rho_0 = 1$

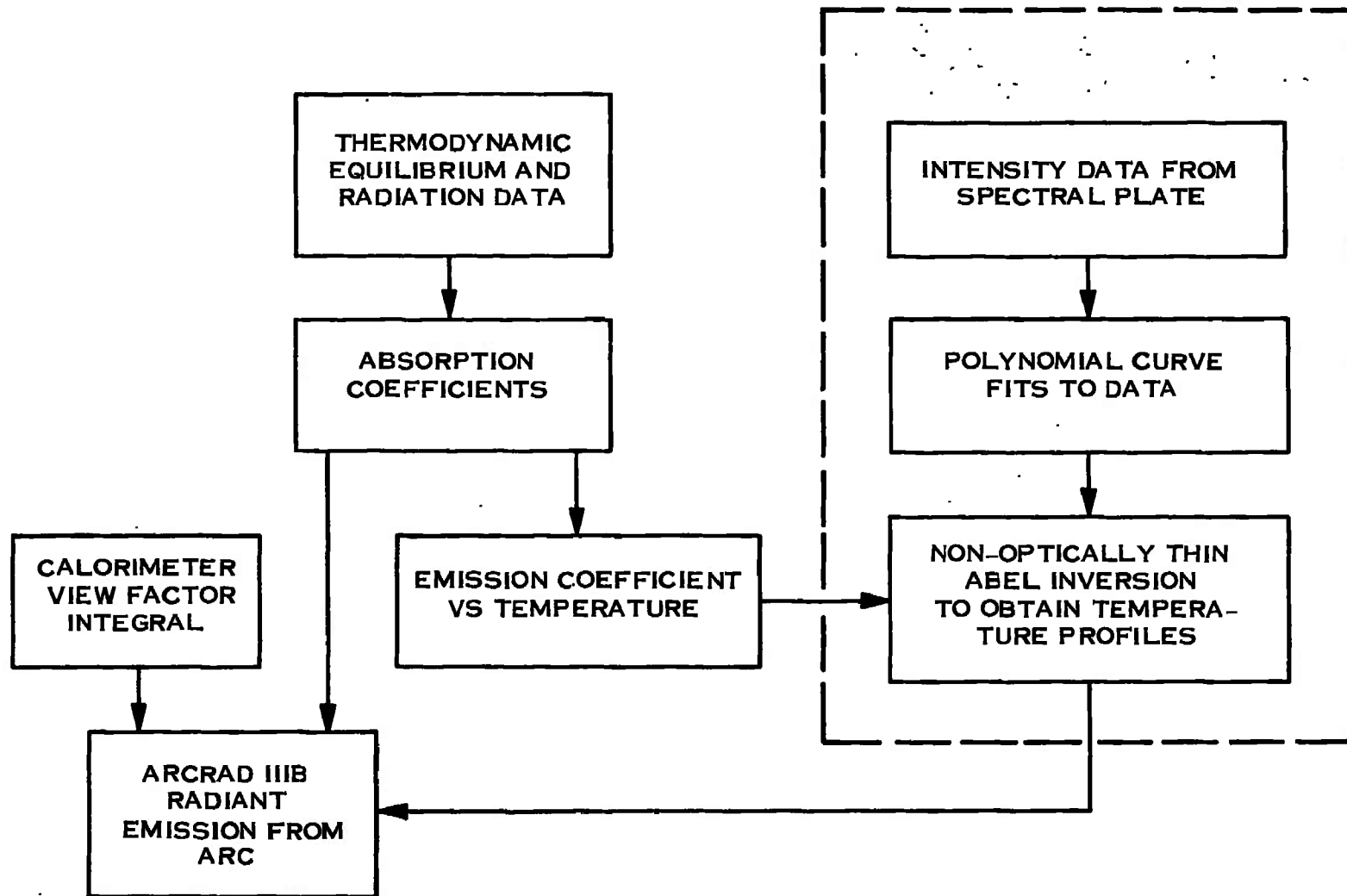


Figure 7. Block Diagram of Computations

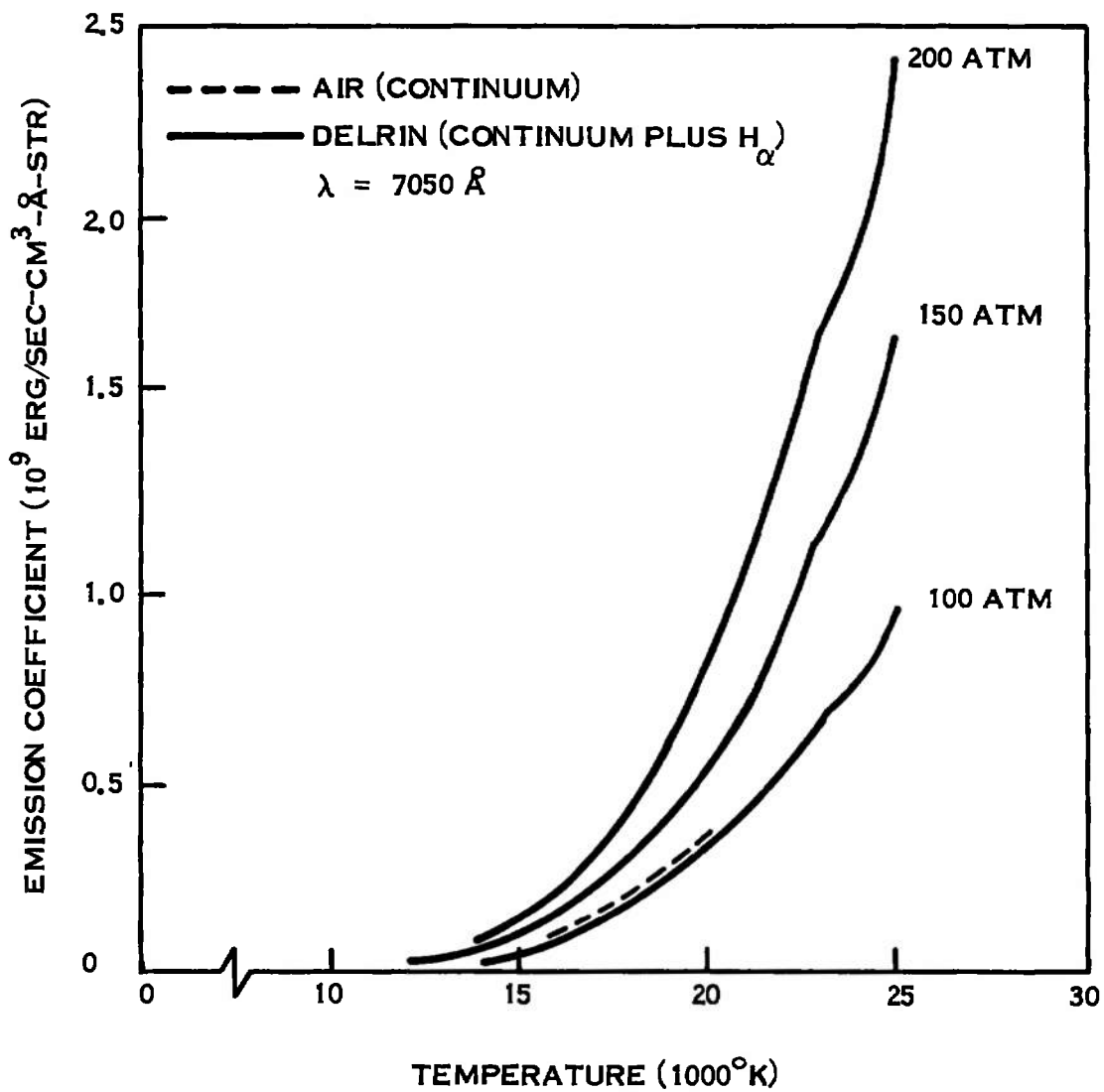


Figure 8. Emission Coefficient for use in Temperature Profile Determination

SECTION IV

APPARATUS

The conceptual design of the experimental apparatus remained largely unchanged from last year. A brief description will follow, but for further details see Reference 1. Figure 9 shows an overall view of the experimental area which is enclosed in armor plate for safety protection. The ensemble has been rearranged since last year.

Arcs were maintained for only a few milliseconds because the large heat flux, of the order of 100 kw/cm^2 , inevitably produces wall ablation after a millisecond. Even with an ablation type constrictor, it is undesirable to run for times longer than about 10 milliseconds because constrictor diameter increases rapidly and this constitutes a time varying boundary condition with strong effect on arc parameters. Power is supplied by shaping the discharge of a $500 \mu\text{f}$, 18,000 volt capacitor bank to square pulse. Capability is 250 amperes for 10 milliseconds with correspondingly higher currents for shorter times. Switching is by triggered ball gaps.

The aluminum test chamber is rated at 6,000 psi and has a volume of 220 cm^3 . Optical observation is made through two symmetrically placed Plexiglas windows, $1.4 \times 4 \text{ cm}$.

Synchronization of the arc and spectrographic exposure or other measurements is achieved with shuttered light sensors positioned around a rotating mirror. The same mirror serves as the central time resolving element of the spectrograph optical system. An exposure of 100 microseconds was a successful compromise of the conflicting requirements of plate exposure and stopping the remaining motion of the arc.

Spectra were recorded on Kodak 1N and 1F plates with a Hilger medium glass spectrograph. Photographic calibration was made with the anode of a carbon arc as intensity standard (37, 38). Identical optical system and exposure time were used for both arc and intensity standard.

Electrical measurements were made with CRT oscilloscopes. A Tektronix 502A was used for recording the weak signal of the calorimeter thermocouple and Tektronix 551 and 545 units for all other recordings.

Measurements were taken at 100, 150, and 200 atmospheres initial pressure. The pressure rise in the test chamber during arcing was measured with a Kistler #602A quartz pressure transducer so that the pressure at the time of the spectral exposure was known exactly.

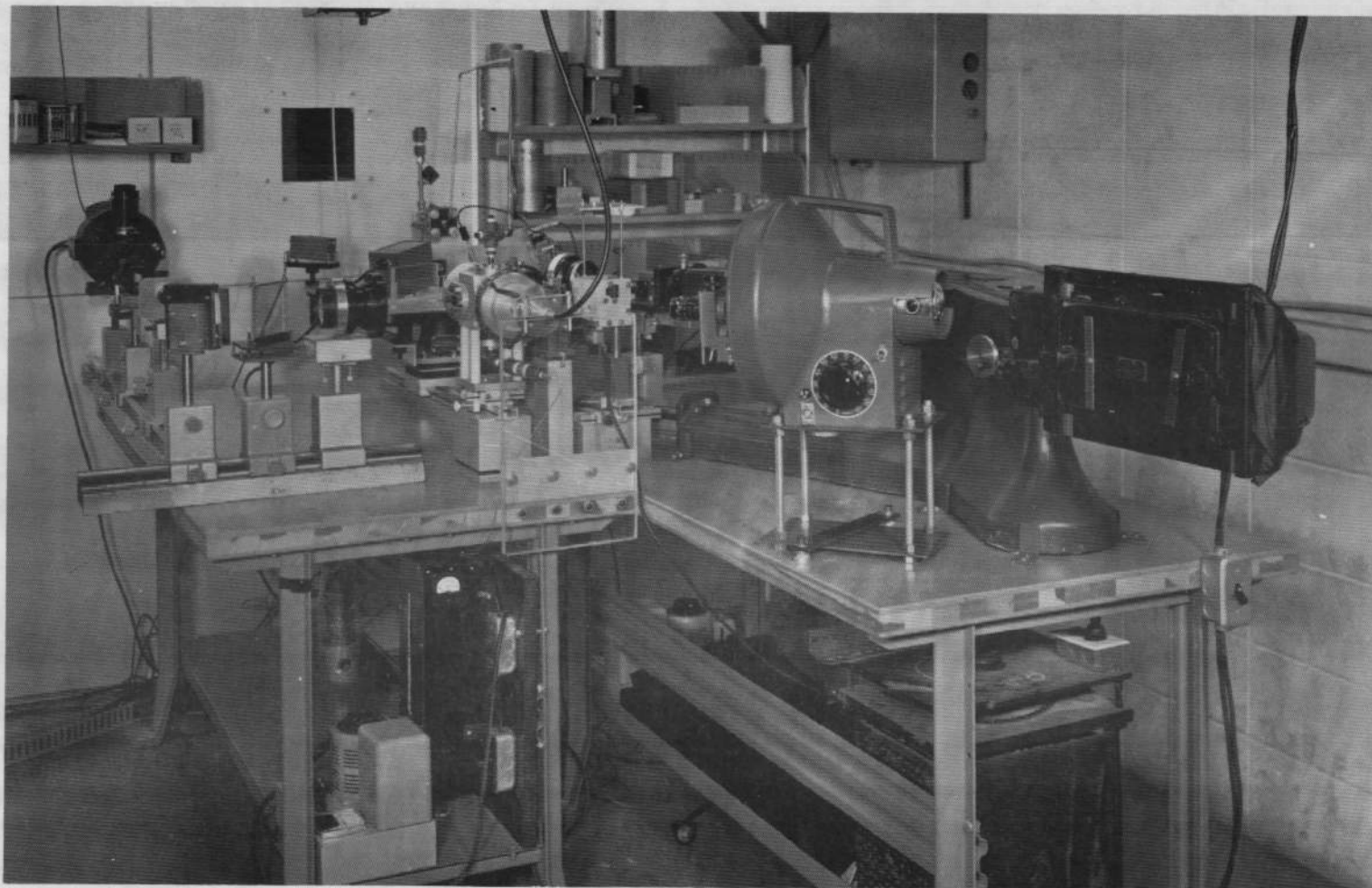


Figure 9a. Overall view of experimental ensemble. The arc is housed in aluminum pressure chamber at center. Two windows and a beam splitter allow simultaneous observation of the arc by spectograph and framing camera at right and streak camera at left.

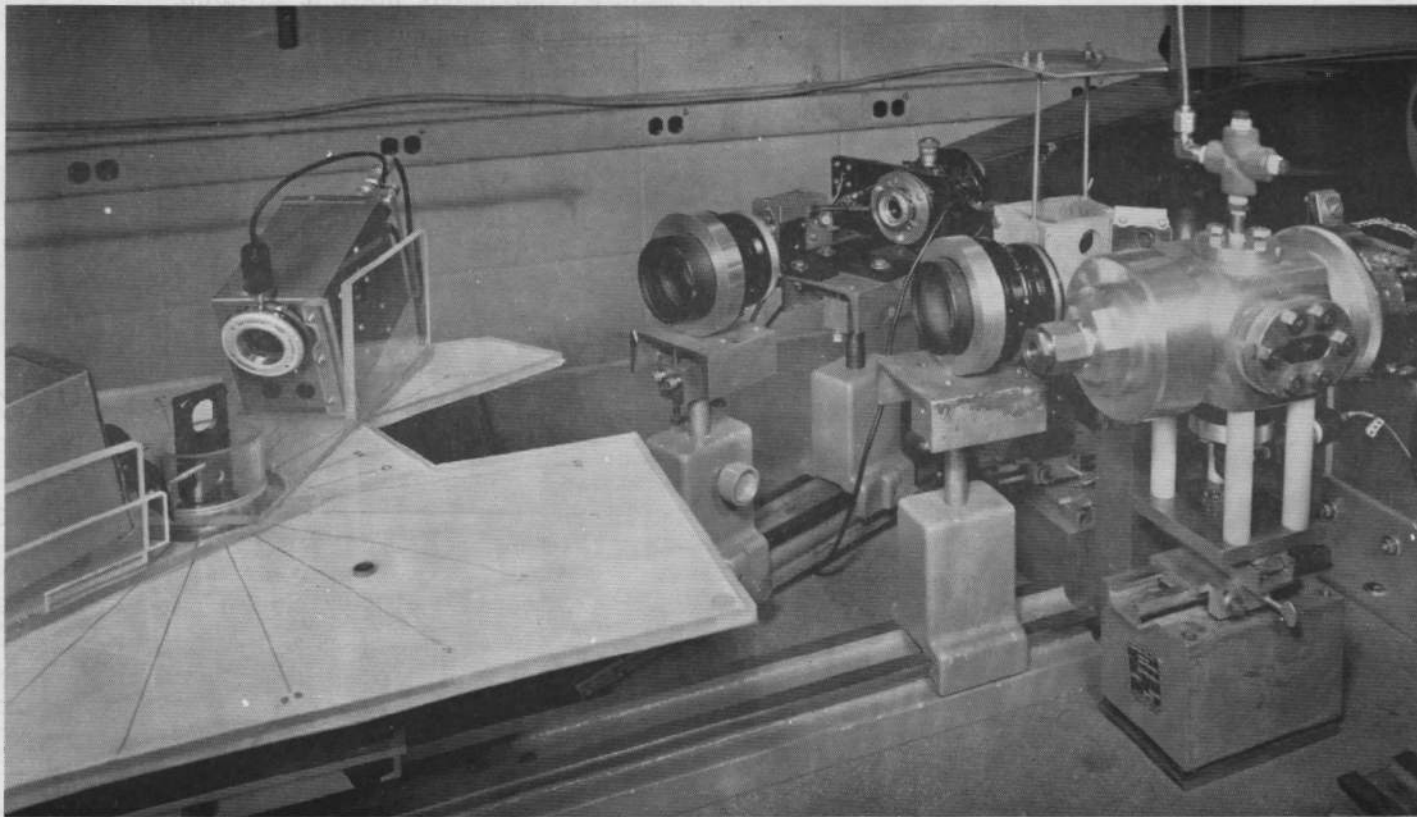


Figure 9b. Close-up view of spectrograph optics. A magnified image of the arc is focused on rotating mirror at left; a second image is formed on the spectrograph slit behind the shutter. The boxes grouped around the mirror contain a light source, light sensors, and electronics to synchronize the operation of the rotating mirror, the spectrograph shutter, and the arc. The flip-flop mirror (partially hidden by arc chamber) is positioned midway between the arc and the carbon arc intensity standard so that both may be photographed by the same system.

SECTION V

ARC CONSTRICTORS AND ARC STABILITY

Perhaps the most important and critical part of the experimental apparatus is the arc constrictor. Our problems with constrictor design and some important observations shall therefore be described in the following separate chapter.

A. CONSTRICTOR STABILIZATION

Previously, two types of constrictors were used.⁽¹⁾ One was the Maecker type constrictor, which consists of a stack of copper discs, forming a cylindrical tube for wall stabilization. The other was an ablation type constrictor with a cylindrical wall made of Plexiglas which vaporized under action of the arc, generating a cylindrically symmetric flow field of wall material.

High speed photographic work with Dynafax framing and streak cameras had shown that the Maecker constrictor could not generate stable arcs at high specific heat fluxes but exhibited strong kink instabilities, with the instability increasing with increasing pressure and/or arc energy. Whereas it was still possible to measure the radial temperature distribution of a 100 atmospheres, 100 amperes arc with an arc energy of 20 kw/cm, an arc at 100 atmospheres, with 400 amperes and 80 kw/cm, was too unstable for a measurement of the radial temperature distribution.

In contrast to this, the ablation type arc had, in some preliminary experiments, shown excellent stability. There is, of course, the drawback that the ablation type arc cannot be burned in an atmosphere of the pressurizing gas, but only in the evaporation products of the tube wall. To get N₂, or CO₂, plasmas, etc., with an ablation type constrictor, one must therefore use these gases in solidified form. This has been tried in the case of CO₂(6); but the required technique is not simple.

In view of these difficulties, an additional effort was made to obtain stable air arcs in the Maecker type constrictor 100 atmospheres and 200 amperes. This attempt was not successful. The use axial magnetic fields up to 2,000 gauss to enforce stability was also to no avail.

B. RADIATION STABILIZATION

At the suggestion of Dr. H. Hurwitz,* the arc radiation rather than tube walls was examined for defining a stable channel. A cylindrical mirror around the arc axis would redirect arc radiation into the arc channel proper and be partially reabsorbed there.

* Dr. Hurwitz is with the General Electric Company Research and Development Center, Schenectady, N. Y.

This process would constitute a feedback between the arc and its radiation and would help to burn the arc on the axis of the cylindrical mirror. The idea was tried and generated a plasma qualitatively much different than obtained in copper constrictors. The plasma did not constrict in a narrow channel, but instead continuously expanded during the 1 millisecond duration of the experiment, Figure 10. While the idea of a radiation stabilized arc shows promise and may well have important applications, the qualitatively very different character of the discharge would require a major amount of work before it could be used for measurements in the present study. Therefore, we did not follow this interesting idea in more detail, but turned with a major effort to the ablation type constrictor which had previously shown good stability.

C. DEVELOPMENT OF THE ABLATION TYPE CONSTRICTOR FOR OPTICAL MEASUREMENTS

The stability of the ablation type constrictor turned out to be excellent--as long as there were no openings in the walls of the cylindrical tube. Figure 11 shows some high speed camera frames and the simultaneous streak picture of an arc in a Plexiglas tube. After a very short unstable period, the arc steadies and remains steady during the complete duration of the experiment. However, the simple cylindrical tube of Plexiglas has some important drawbacks if side-on temperature measurements are to be made: (1) the tube constitutes a bad cylindrical lens which distorts the arc image; (2) Plexiglas evaporates only partially under action of the arc and shows some surface carbonization (The carbon particles often are focussed on the spectrograph slit and cause a streaky spectrogram); (3) The Plexiglas wall does not evaporate completely homogeneously but attains, after a while, a frosty glass appearance. None of these effects are acceptable and, therefore, a good window in the Plexiglas wall was needed for better quality optical observation.

The simplest window would be a slot between two short Plexiglas tubes, Figure 12. With this design, part of the plasma streams through the slot and the luminous volume is larger than the arc channel proper. Moreover we found arcs burning violently unstable in this design, apparently because small maladjustments between the two Plexiglas tubes caused an unsymmetric and fluctuating flow field.

After several intermediate steps, we came finally to the design shown in Figure 13. This design has a flat quartz window, relatively far removed from the arc channel. The window is mounted tightly to the body of the plastic "tube" to prevent plasma from streaming out into the window area. The design is symmetric with two windows at 180° for simultaneous optical observation with our time resolved spectrograph and a streak camera. As "tube" material, Delrin was chosen, both for its simple composition and for its "non-carbonization" characteristic. The flat window was Suprasil quartz, chosen for minimum energy absorption of the extremely strong far ultraviolet radiation of our arc.

This constrictor, which will be referred to as our "optical" constrictor, maintains a relatively stable arc, as shown by Figure 14. The figure reveals, however, that the arc does not burn strictly on the axis of the tube but slightly to one side, and some very slow, low amplitude motions persist. This degree of stability, however, is sufficient for our very short time spectrographic exposures.

Besides the "optical" ablation type constrictor, several others were built for measurements of electrical gradients, plasma pressure, and radial heat flux. For these measurements, the rather complicated optical window was not necessary and therefore omitted. All constrictors, however, were basically Delrin tubes with minor design modifications as demanded by the specific measurement. They are described in the sections where we report the respective measurements.

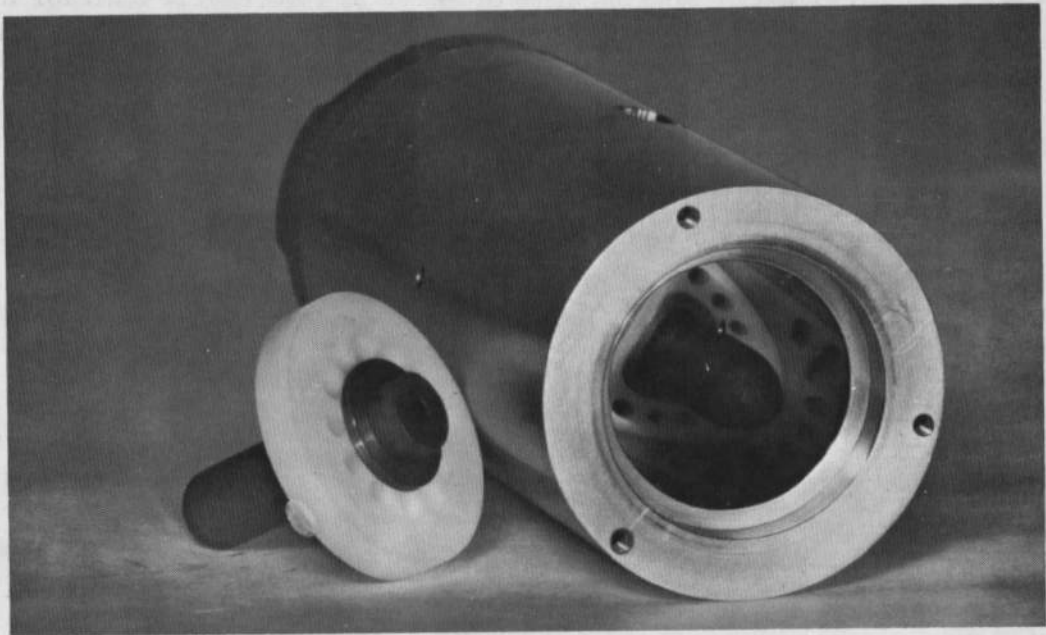
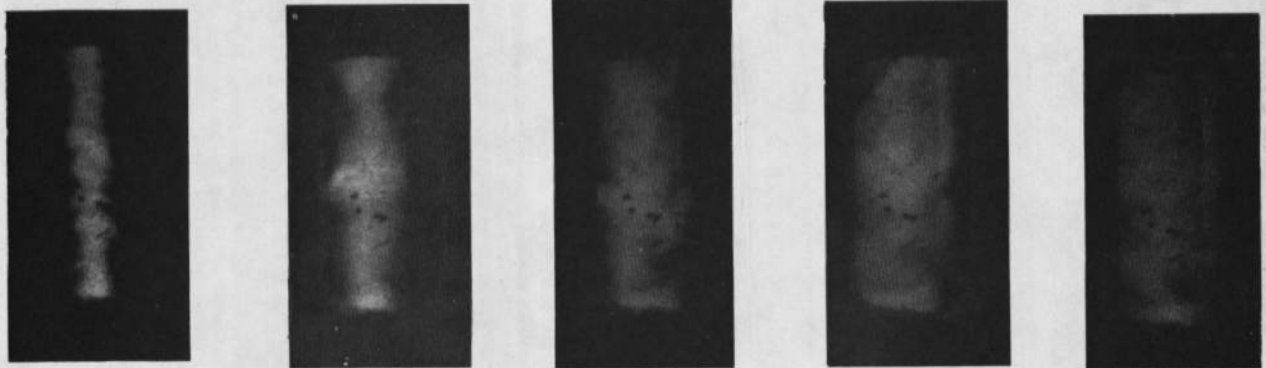


Figure 10 a. Constrictor designed for "radiation stabilization". The inner walls are highly polished and accurately concentric with the carbon electrodes.



100 μ sec

300 μ sec

500 μ sec

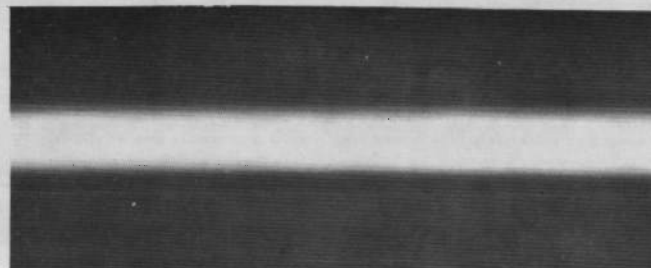
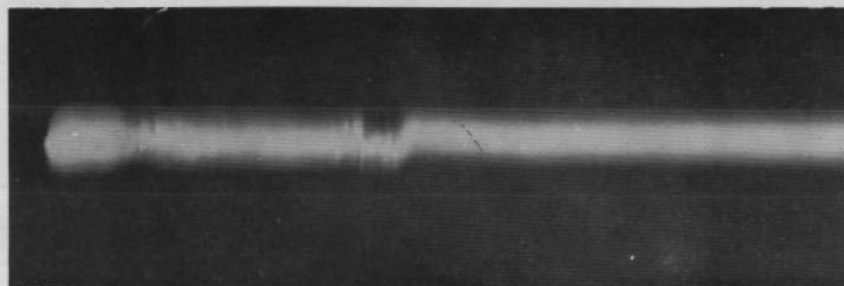
700 μ sec

900 μ sec

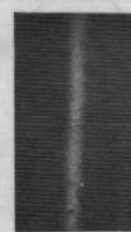
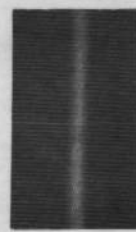
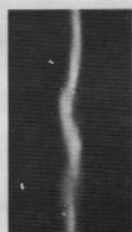
Figure 10 b. Magnified views of the "radiation stabilized" arc suggested by Hurwitz. The port is 10mm x 5mm. The 300 ampere arc was initiated by exploding a 0.00025 inch diameter tungsten fuse wire which was accurately centered at the focus of the polished stainless steel tube. Compare this diffuse arc with the constricted ones elsewhere in this report (Figure 11) and last year (Ref. 1, Figure 36).

Initial Development of Arc

Duration of Spectrograph Exposure
(100 μ sec.)



38



Time From
Arc Initiation
(μ sec.)

60

190

320

1,300

2,600

Frame

1

2

3

10

20

Figure 11. Stability of a Plexiglas ablation arc as seen by a streak camera and a framing camera. Note that the arc is initially unstable but becomes stable in a few hundred microseconds. The arc in the streak camera film is magnified 5.5 x; in the frame pictures magnification is 2x. The omitted frames are completely stable and identical with frames #3, 10 and 20.

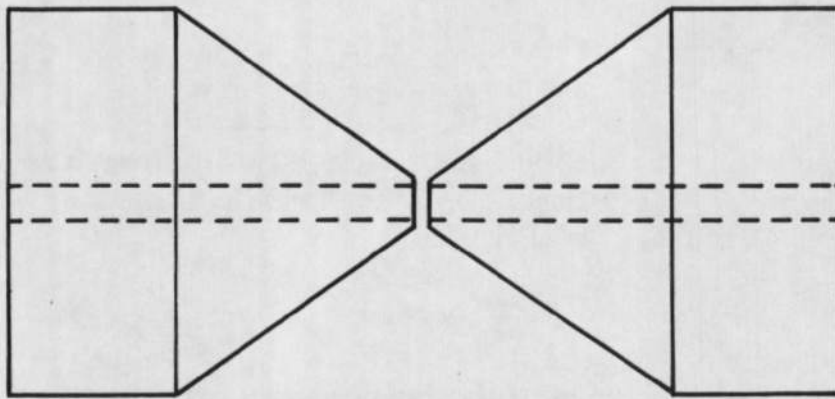


Figure 12. Schematic design of a simple, two-piece ablation constrictor with provision for spectroscopic observation of the arc. Such a device was found to produce an unstable arc because of slight misalignment of the two pieces and enlargement of the arc in the free region. For final design see Figure 13.

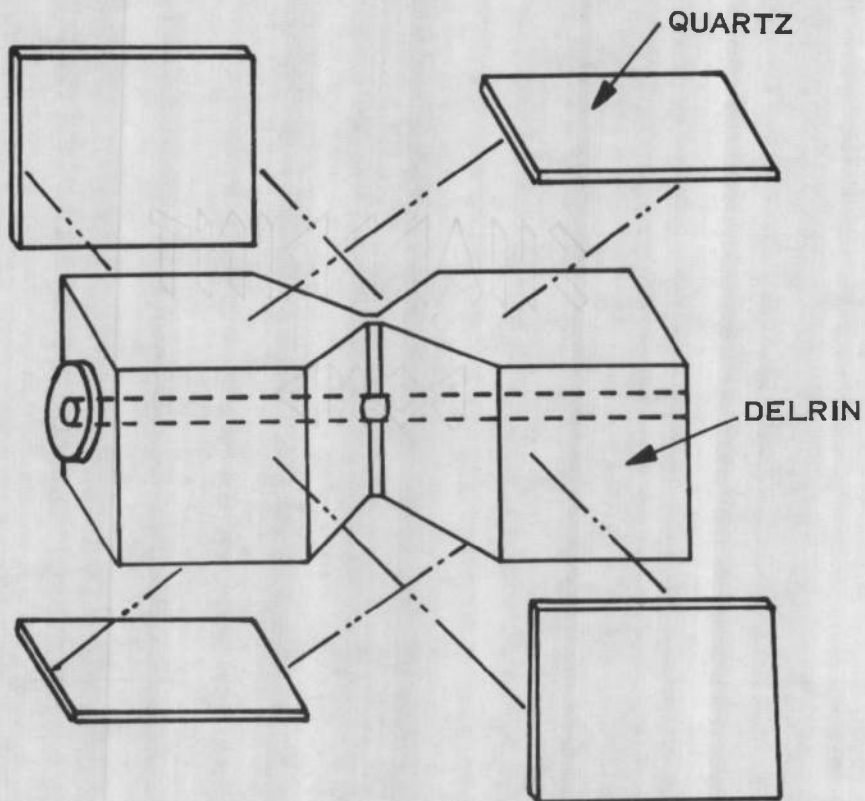


Figure 13 a. Schematic design of optical constrictor. The arc tube is made from one piece with minimal openings for observation. The Suprasil quartz windows provide a pressure seal yet pass almost all of the incident radiation.

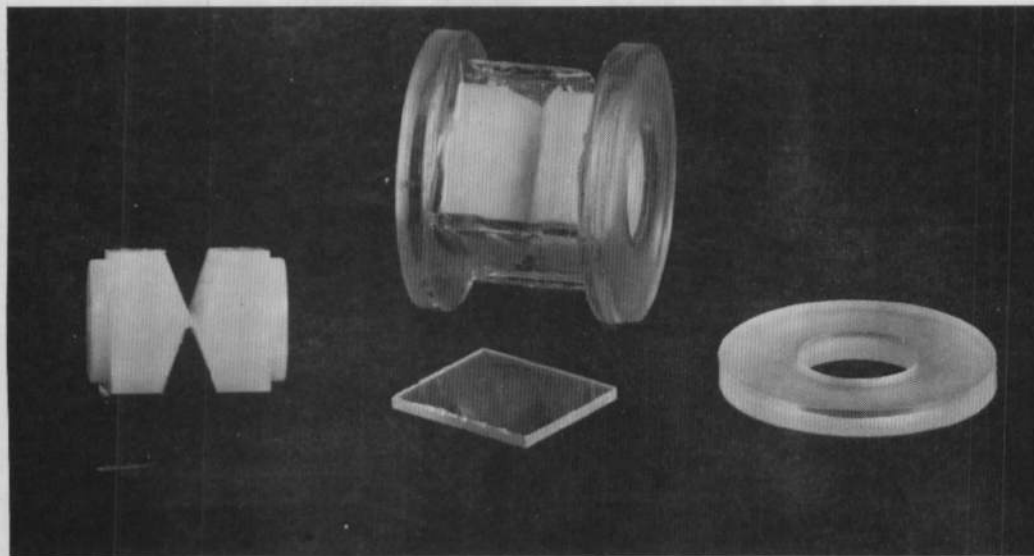


Figure 13 b. Photograph of an assembled optical constrictor and parts. Assembly was by glue placed away from the arc to avoid ablation.

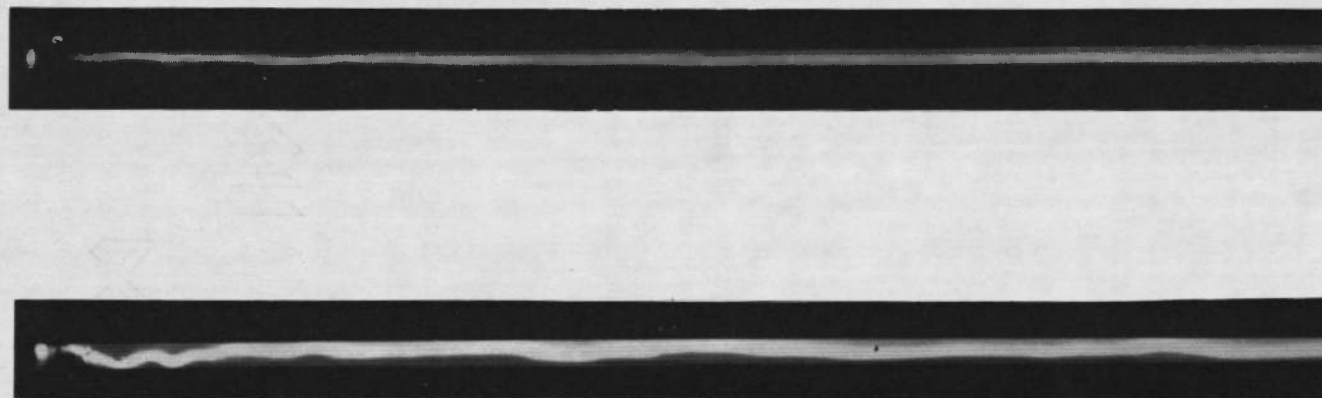


Figure 14. Streak camera traces of a stable and an unstable test in Delrin constrictors. Minor design changes can destabilize the arc and make measurements impossible. The view slit width must be the arc tube radius; the view slit must be sealed; and the "dead volume" between the window seal and the arc tube must be less than or equal to minimal.

SECTION VI

MEASUREMENT OF ARC PARAMETERS

It is of considerable importance to check whether the arc is uniform along its length. If the arc is axially nonuniform, observations would be required at a number of points along the arc axis, which is time consuming. Plasma flow from the constrictor ends was in the range of 1 to 2 grams/second, which might be expected to produce a large pressure rise in the constrictor and thus an undesirable axial variation of other arc properties. Meaningful calculation was difficult because most of the axial flow occurs near the walls where little is known of the temperature distribution, and there is also the possibility that a thin layer of Delrin liquid flows along the walls. Consequently, direct measurements of the pressure rise at the center of the constrictor, where spectral observations are made, was deemed advisable, along with voltage gradient measurements for several constrictor lengths.

A. PRESSURE RISE IN THE CONSTRICTOR

For the pressure measurement a special arc constrictor was built as shown in Figure 15. A Delrin port connects the arc duct to a steel tube of 0.009 inch inside diameter, which leads to a quartz pressure transducer (Kistler type 601 A). This arrangement enables us to read the pressure increase in the center of a constrictor during arc operation. The system was tested for rise time by recording the transducer output while an over-pressure protection diaphragm on the test chamber was intentionally burst. A simultaneous record of pressure drop as taken from a transducer directly connected to the pressure chamber was used as a comparison standard. From this measurement overall system response time was found to be of the order of 1 millisecond, adequate for our purposes.

The pressure transducer was then used to measure rise of the plasma pressure in the constrictor during arcing. It was found that the rise was very nearly the same as that for the entire high pressure container: approximately three atmospheres during a 5 millisecond run at 100 atmospheres. With such a small pressure drop in the tube, there should be no major effect from the flow field on the structure and energy balance of the arc.

B. VOLTAGE GRADIENT AND AXIAL INTENSITY VARIATION

Figure 16 shows the experimental arrangement used to determine voltage gradients. The Delrin constrictor is a simple cylinder placed between carbon electrodes accurately spaced 1.5 mm from each end. The length of the constrictor was varied in successive shots and the arc voltage, read from differential probes, was plotted as in Figure 17 to give the voltage gradient. Despite the slight scatter in the data points it is clear that there is no systematic deviation from linearity in the range of lengths tested. The non-zero voltage at "zero" length corresponds to the potential drops in the spaces between constrictor and electrodes plus the anode and cathode drops. The constrictors used for spectral investigation were 16 mm long, as were the constrictors tested for pressure rise.

The constancy of the voltage gradient along the tube agrees well with our earlier observation of a negligible pressure gradient along the arc and also with the observation that Plexiglas arcs show no intensity variation along the tube length. It appears, therefore, that at the conditions of our experiments, no significant axial inhomogeneity exists in the ablation type arcs.

Figures 18 and 19 show the results of gradient measurements at higher pressures with a similar result. Clearly the voltage grows with pressure, as shown in Figure 20. Figure 21 shows the corresponding curve made last year in air but unreported at that time. Notice the somewhat weaker dependence on air pressure as compared with the Delrin results. Plexiglas constrictors gave the same general result but with lower voltage gradients (Figures 22 and 23). All of the tests discussed above were made at 250 amperes, but Figure 24 shows that the voltage gradient is only slightly affected by a change in current near this value.

C. CONSTRICTOR ABLATION RATE

The ablation rate was determined by weighing the constrictors before and after testing on an analytical balance. Losses were generally several milligrams and could therefore be determined with fair accuracy. Arc energy was simply computed as the time-integrated product of arc current and voltage; anode and cathode voltage drops were neglected.

It was found that the ablation rate increased when the arc was burned for longer times (Figure 25). A rising curve for short times could be expected from the initial period required to initiate ablation. Evidence for the existence of this "initiation period" comes from high speed photographs, (Figure 14) which show the arc initially unstable, indicating that ablation stabilization has not begun, and from the arc voltage records which show an initial period of high voltage that drops when the photographs indicate stability.

Figure 25 also shows that the ablation rate increases at greater current. Pressure is also a strong factor in determining the ablation rate. Figure 26 shows a substantial increase in ablation of Delrin as pressure rises from 150 to 2900 psig.

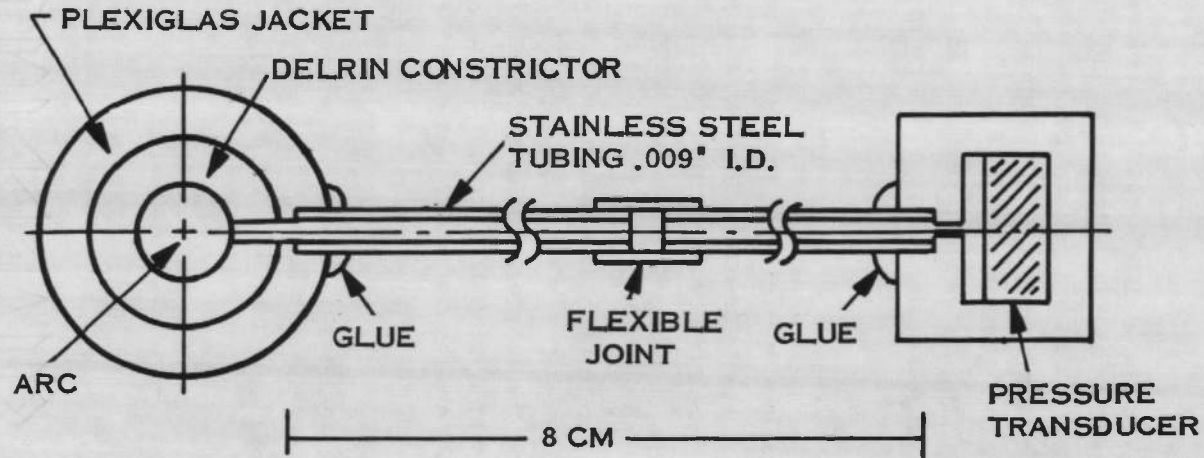


Figure 15a. Schematic diagram of setup for measurement of pressure rise at center of Delrin ablating constrictor. The steel tube is set back sufficiently far from the arc for "arc-over" protection. Careful tests were made to insure that the response time of the system was adequate for accurately measuring the pressure rise produced by a 10 msec. arc.

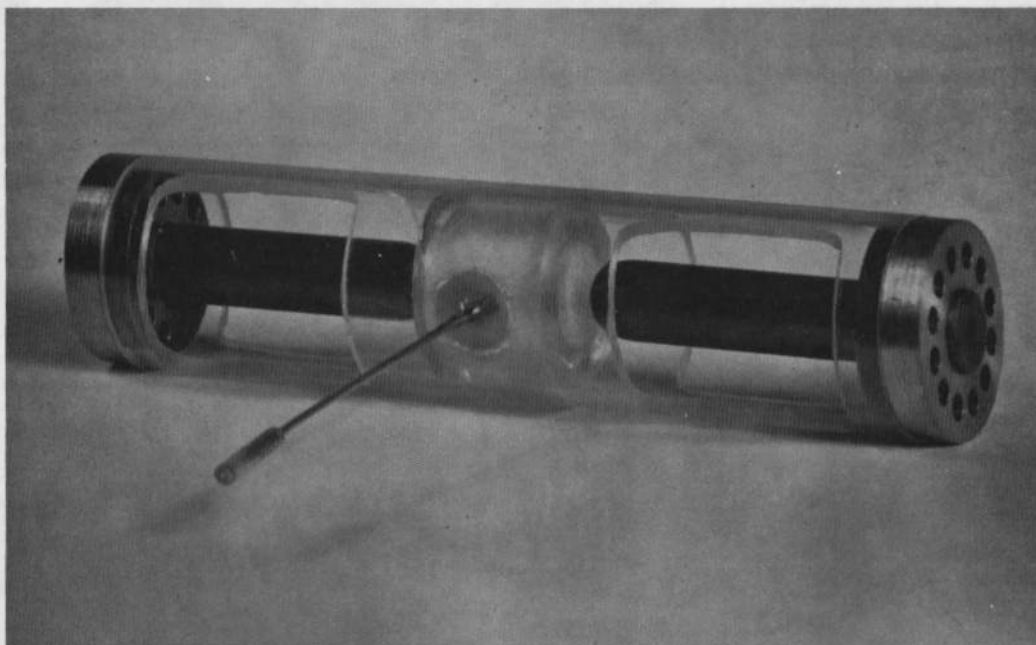


Figure 15b. Photograph of pressure measuring constrictor. The constrictor is shown mounted in a Plexiglas case with carbon electrodes positioned for firing. The copper mesh "coolers", Fig. 16, have been removed to show the electrodes. In the foreground is the flexible joint of the steel tube made with a jacket of polyethylene tubing.

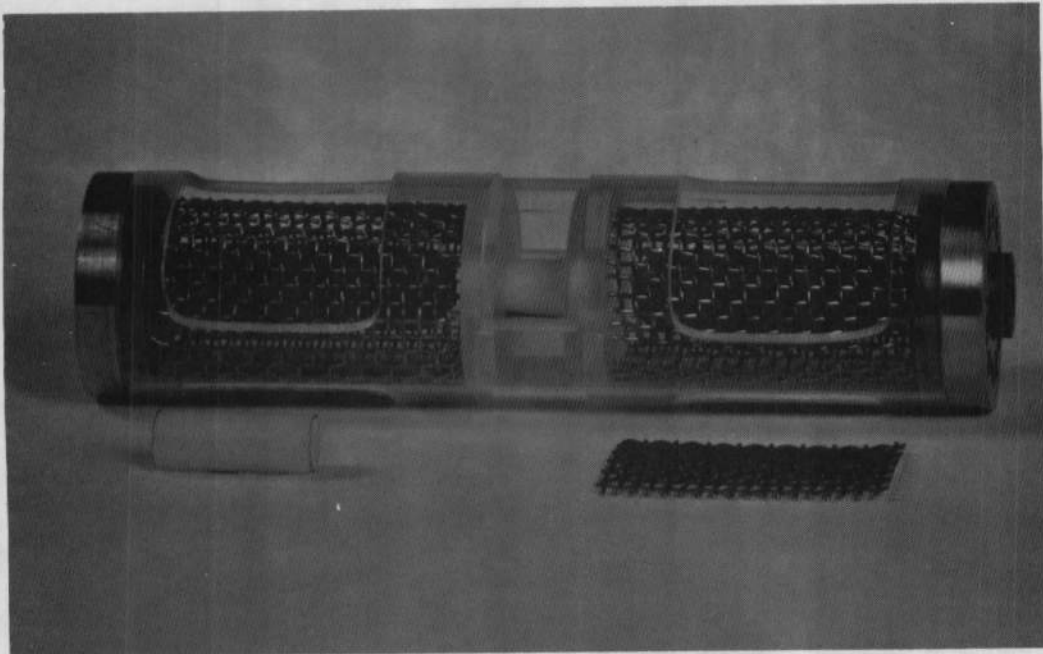


Figure 16. Delrin constrictor ready for firing. The plasma exhaust from the ends of the constrictor passes through layers of a copper mesh which cool the plasma and reduce the pressure rise in the arc chamber. The spacing between the ends of the constrictor and the electrodes is fixed at 1.5 mm.

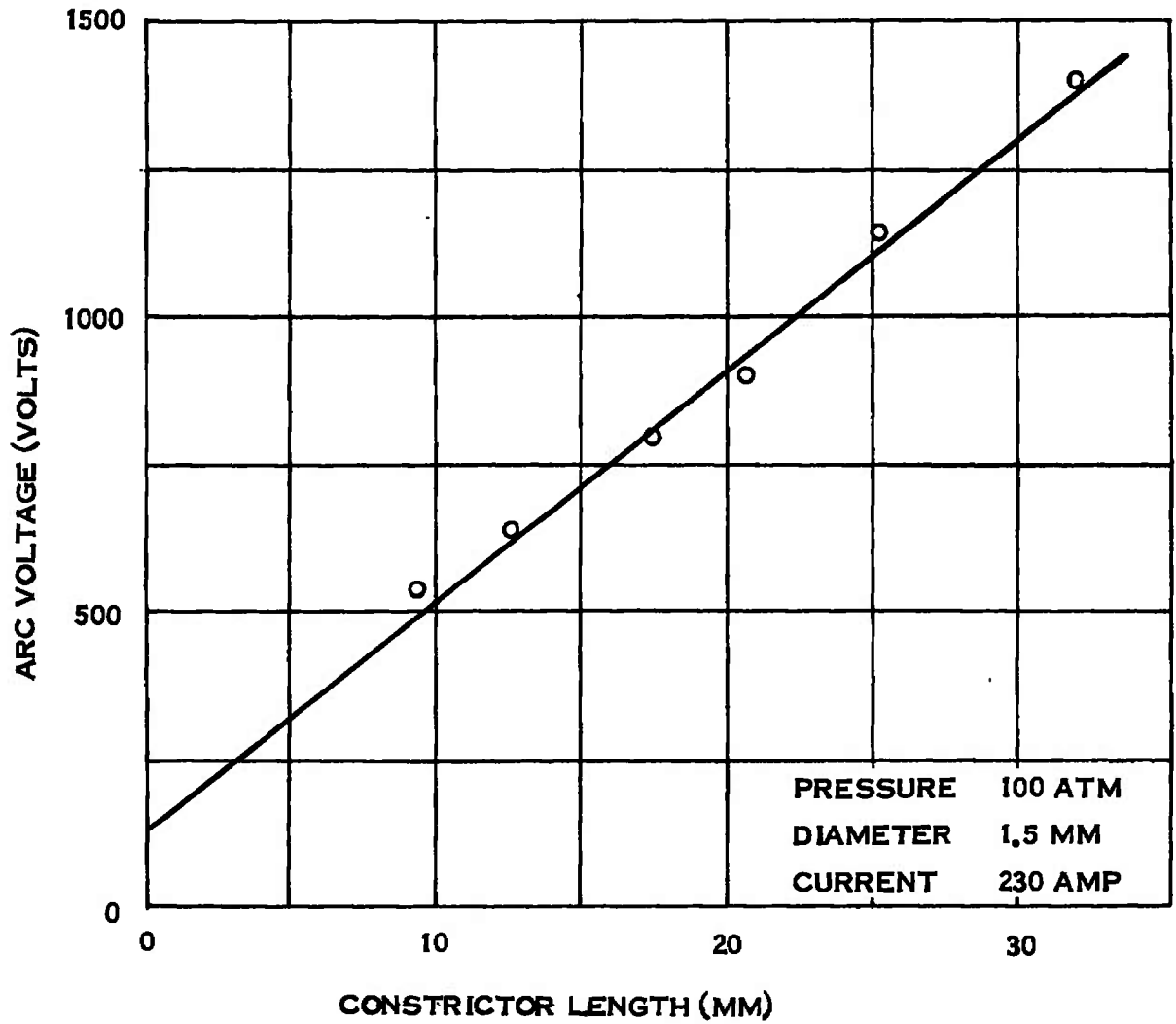


Figure 17. Arc voltage for Delrin constrictors of different lengths. The data points show no systematic deviations from linearity in the range of lengths tested. The slope gives a value of 395 volts/cm for the arc.

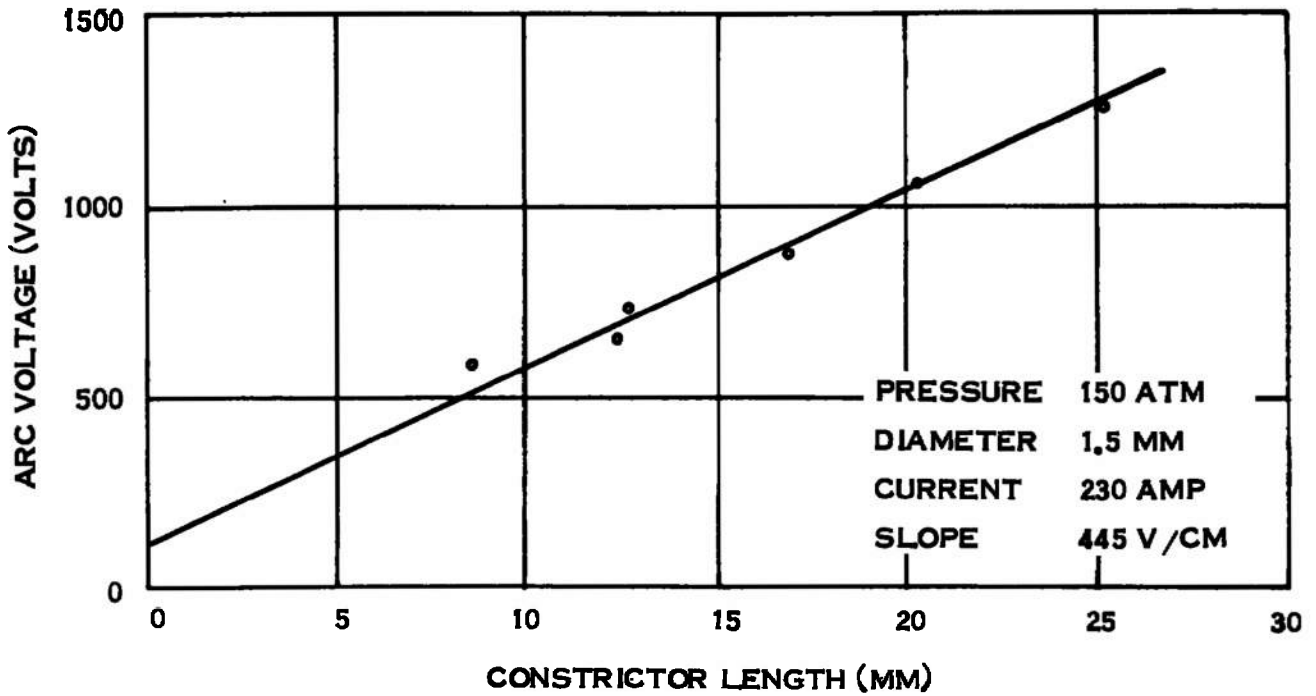


Figure 18. Arc voltages for Delrin constrictors of different lengths.

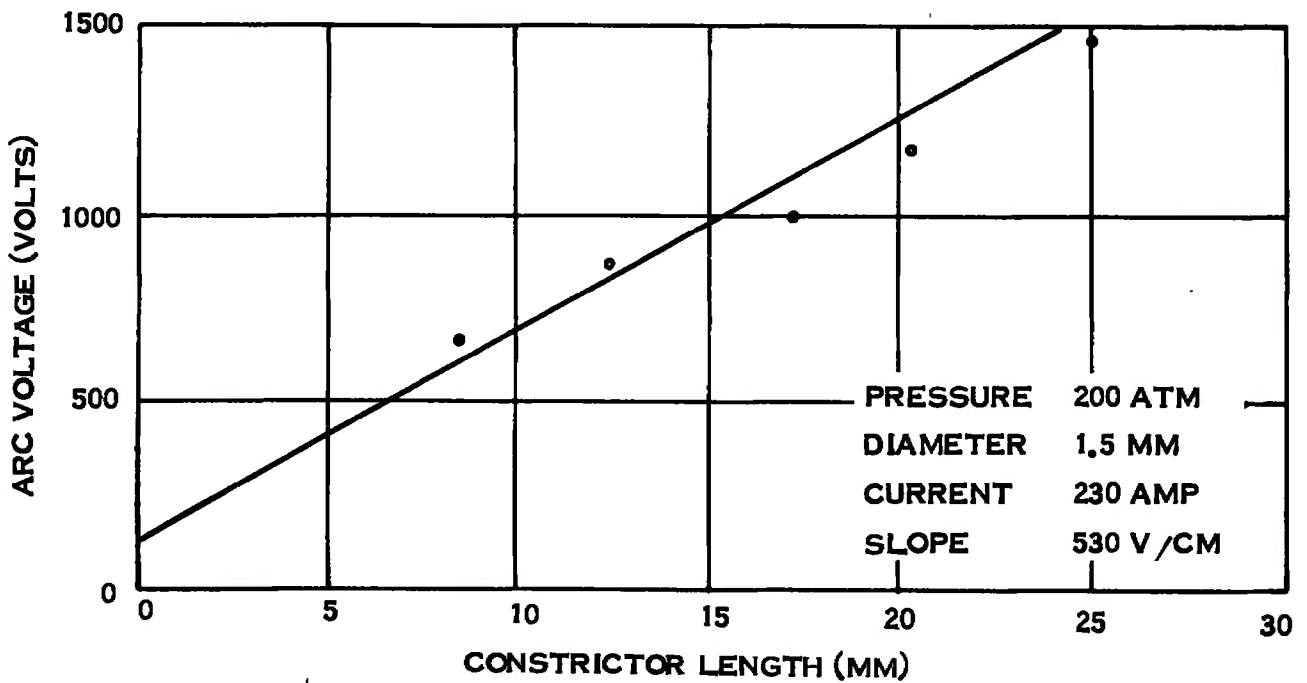


Figure 19. Arc voltages for Delrin constrictors of different lengths.

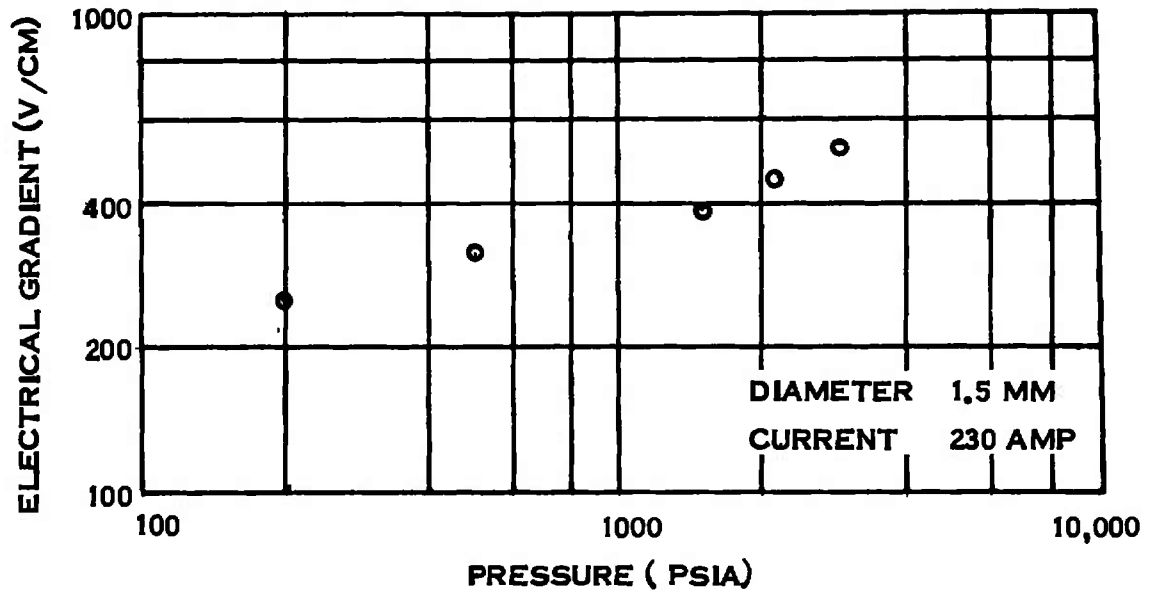


Figure 20. Voltage gradient of Delrin ablation arc vs pressure

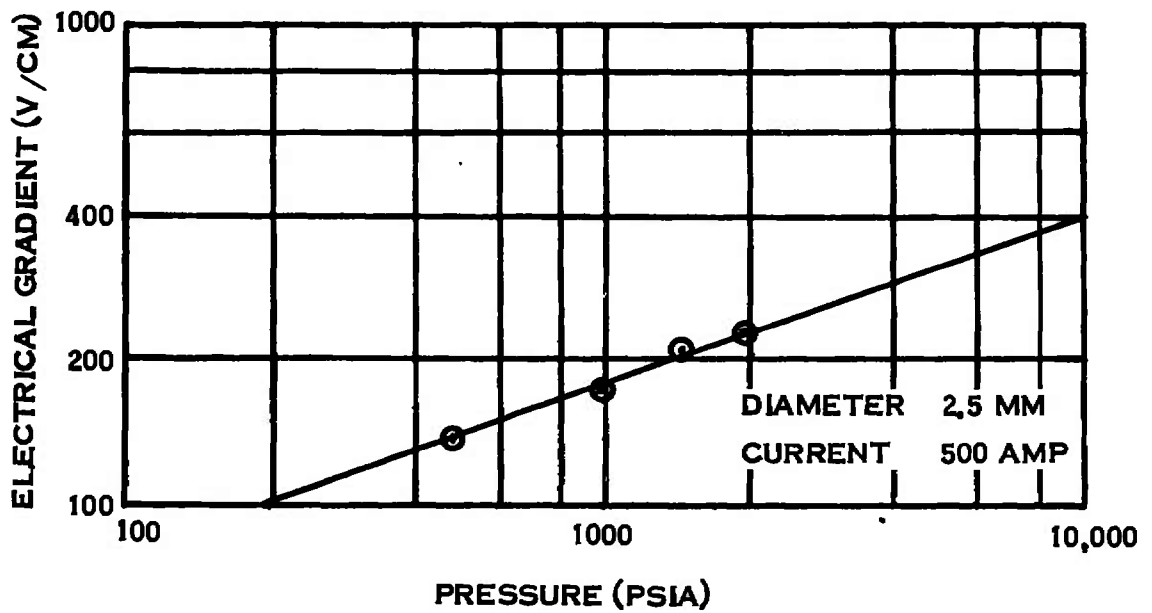


Figure 21. Voltage gradient of air arc vs pressure

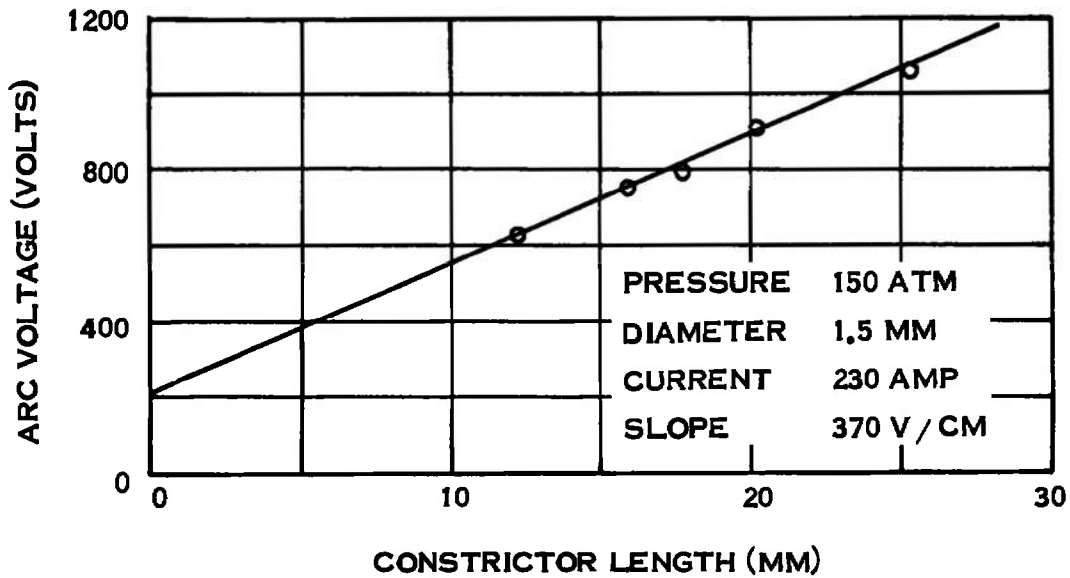


Figure 22. Arc voltage for different lengths of Plexiglas constrictors. Compare with Figures 17, 18 and 19.

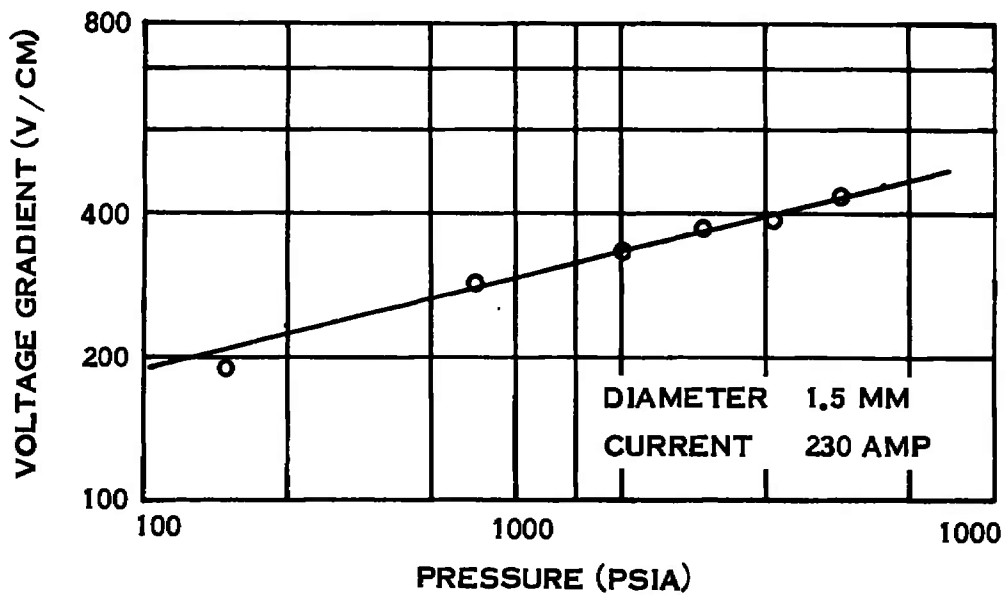


Figure 23. Voltage gradient of a Plexiglas arc as a function of pressure. The Plexiglas arc has a potential gradient between those of air and Delrin.

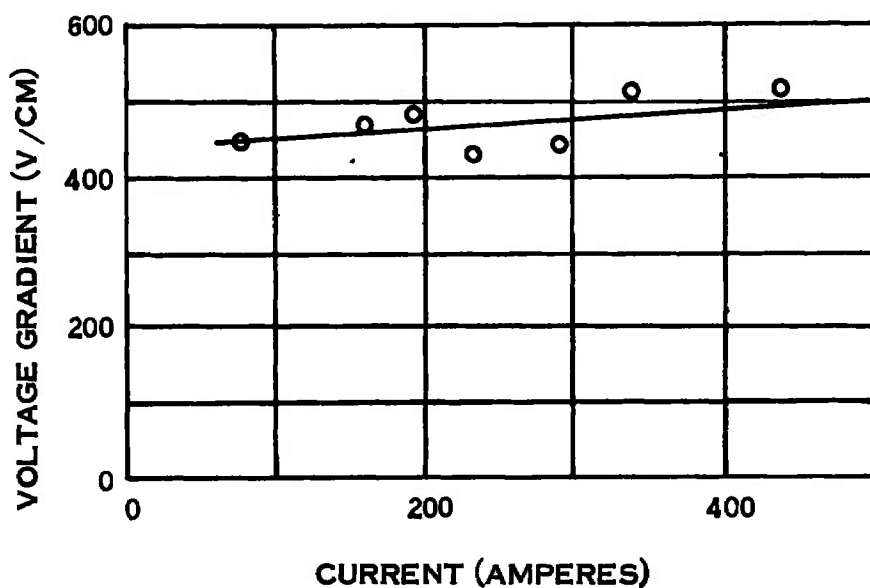


Figure 24. Voltage gradient of a Delrin ablation arc vs current. Despite the scatter of data points, it can be clearly seen that arc current has small effect on the voltage gradient above 100 amperes. These experiments were made in a 1.5 mm ID tube at a pressure of 150 atmospheres. Earlier experiments with 2.5 mm ID tubes showed voltage gradients 25 percent lower.

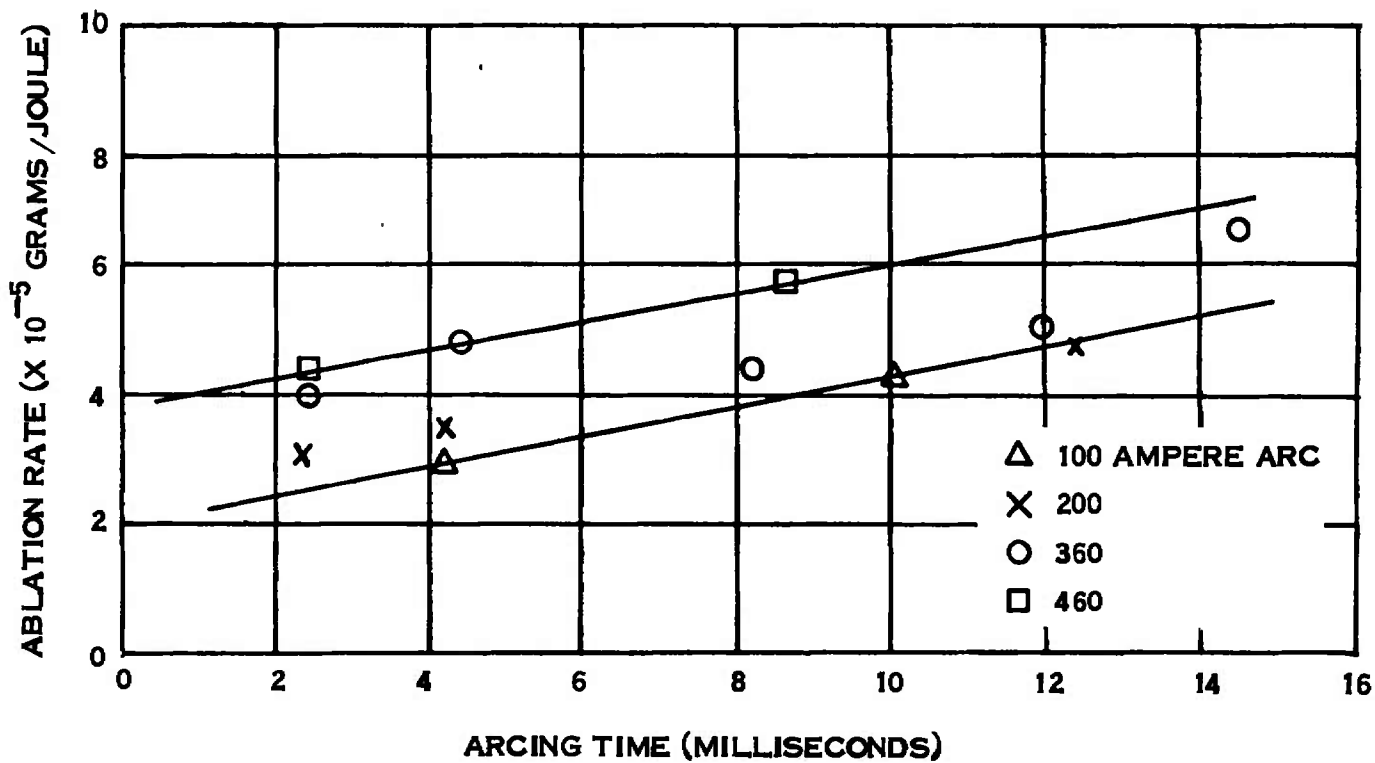


Figure 25. Ablation of Delrin at 100 atmospheres. The ablation rate increases slowly with arc current and with longer burning arcs. These results were taken with 2.5 mm ID constrictors which were weighed before and after the test on an analytical balance.

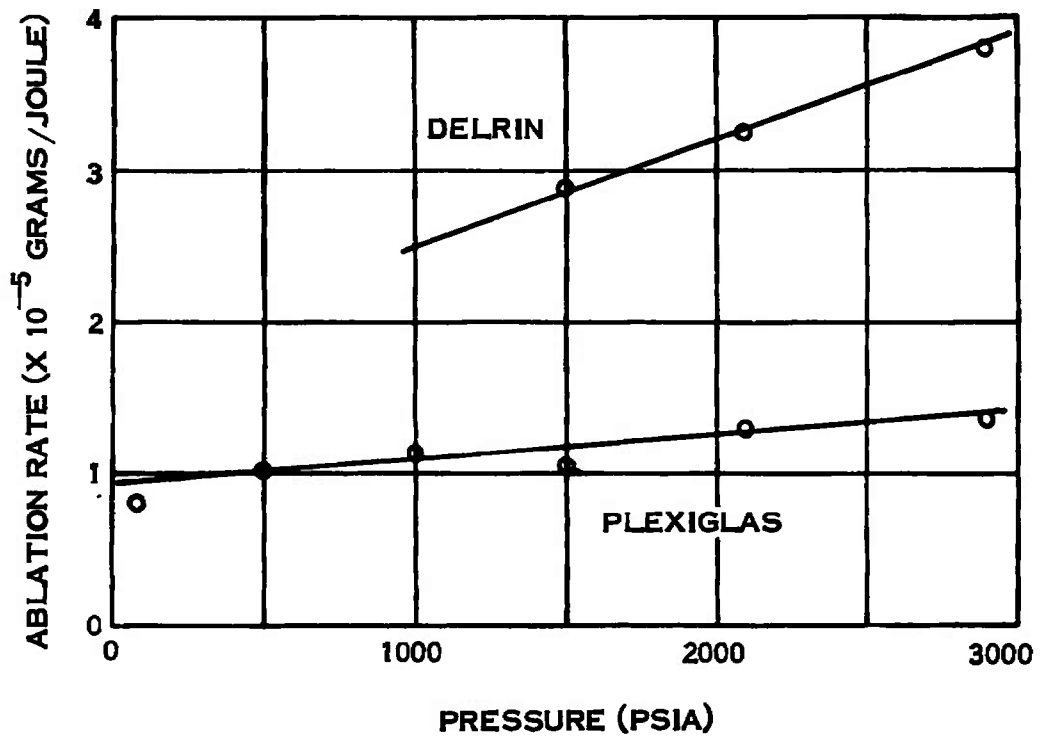


Figure 26. Variation of ablation rates with pressure. The Delrin ablation rate is more strongly influenced by pressure changes.

SECTION VII

MEASUREMENT OF RADIANT HEAT FLUX

The radiant heat flux calorimeter consists of a small copper ring of known mass concentric with the arc. The temperature rise in the ring is measured with a copper-constrictor thermocouple. The ring is recessed and protected from conducted heat of the arc. A previous report ⁽¹⁾ gives a full description of the calorimeter used for cascade air arcs, but several design modifications were required to adapt the device to measurement of an ablation arc.

Figure 27 shows the final design of our ablation type arc calorimeter. A light baffle was added to limit stray reflections and more closely approximate the calculated view factor and the calorimeter ring is protected from the arc plasma by a Suprasil quartz tube. The tube eliminates heating by conduction and convection yet passes almost 90 percent of the incident arc radiation. Operation of the arc for 5 milliseconds did not significantly damage the quartz. A special black Delrin (doped with 0.3 percent Carbon) was used to prevent energy transmission through the normally translucent (40 percent of visible light through a 1 mm layer) tubing.

In spite of these precautions, no useable results were obtained from calorimeter measurements. Temperature rise was generally much too high to be solely due to arc radiation and changing too rapidly to be reasonably extrapolated back to time of arc cutoff. * Since the expected rise was about 10^0 C (in 3 milliseconds), small effects could distort the measurement.

* Vacuum switches turn on the thermocouple circuit approximately 12 milliseconds after arc extinction to protect it from the very high voltages during arc operation.

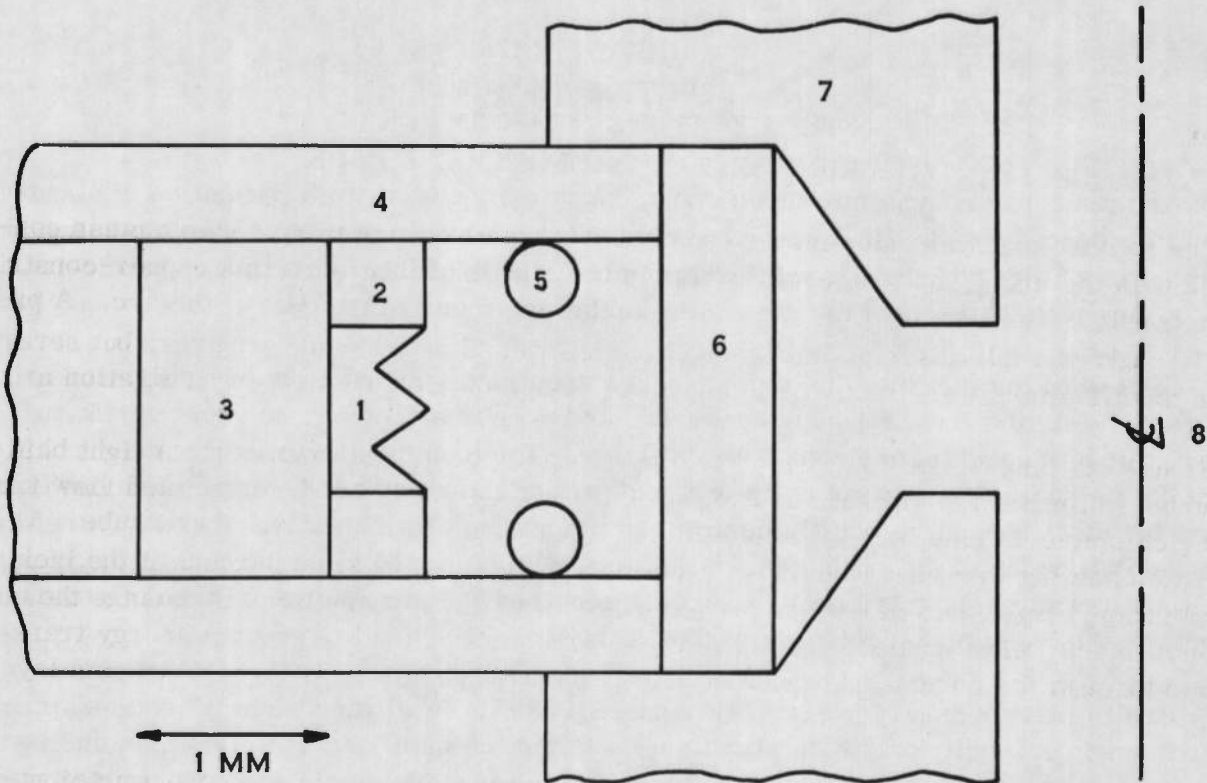


Figure 27a. Schematic Design of Calorimeter

- | | |
|------------------------|-----------------------|
| 1 - Calorimeter | 5 - Wire Light Baffle |
| 2 - Insulating Support | 6 - Suprasil quartz |
| 3 - Dead Volume | 7 - Black Delrin |
| 4 - Copper Disc | 8 - Arc |

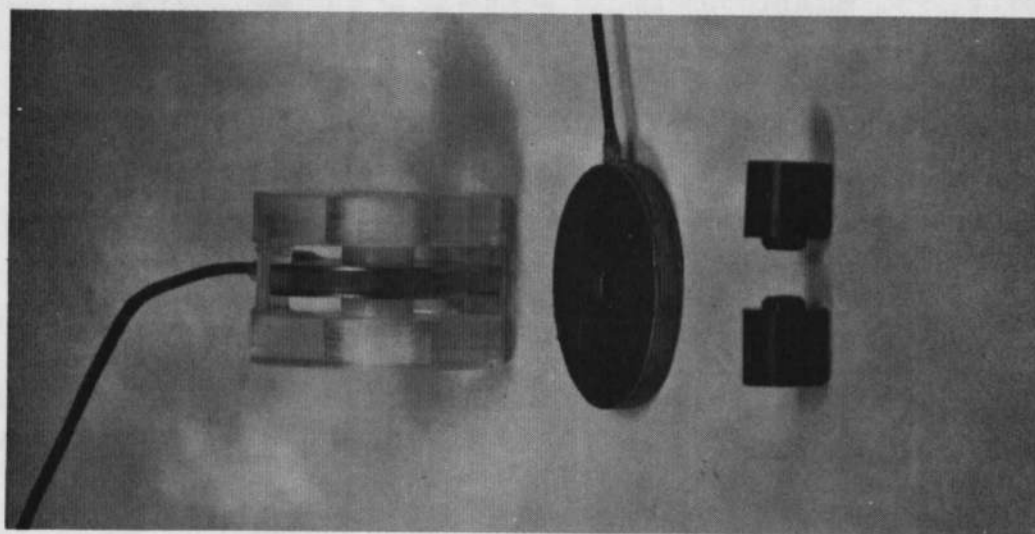


Figure 27b. Photograph of Calorimeter Constrictor and Parts

SECTION VIII

TEMPERATURE MEASUREMENTS

Arc temperature was measured spectroscopically with a time resolution of about 100 microseconds. The time resolving element was a rotating mirror; the basic spectrograph was a Hilger medium glass instrument. Details of this apparatus and the general measuring techniques used are discussed in the previous report (1).

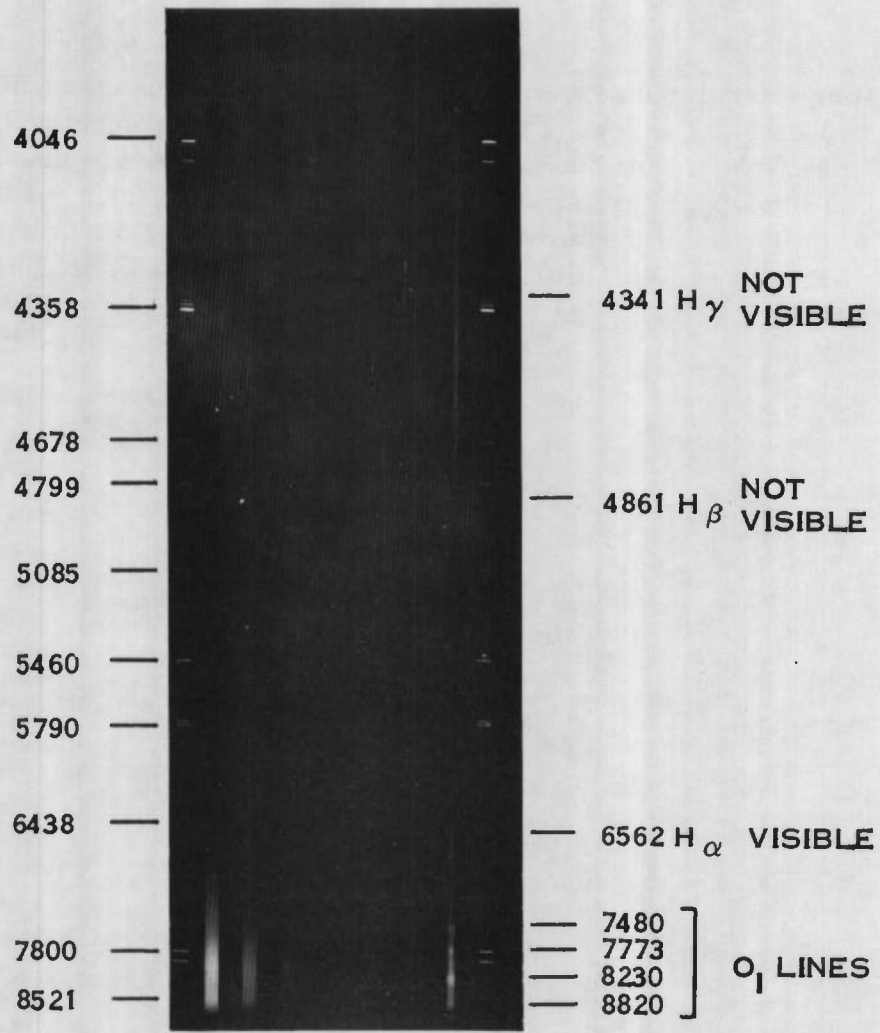
In view of the fact that the high pressure spectra displayed a largely continuous character with the lines strongly broadened and even overlapping, no great variety of temperature measuring methods was available. The plasma was strongly reabsorbing even in the continuum, so optically thin methods could not be used. Line radiation emerging from the discharge showed little contrast to the strong continuous radiation. Therefore, the absolute value of the continuous radiation was considered to be the most likely candidate for a temperature measurement. The data required was a sequence of absolute measurements of the "side on" spectral intensity of the arc.

Preliminary measurements were made at 8330\AA . However, when it became apparent that line wings might contribute significantly to the intensity, all the plates, including the one for air, were reevaluated at 7050\AA . At the latter wavelength, the continuum dominates in air and the only line of importance in Delrin is the H_{α} line. This line profile is well known, and the curves and asymptotic formula of Griem, Kolb and Shen⁽¹³⁾ were used for a detailed evaluation of its contribution to total absorption coefficient. As temperature increases, the line tends to increase both in intensity and breadth, so that at 7050\AA the line contribution is negligible at $10,000^{\circ}\text{K}$, equal to the continuum at $16,000^{\circ}\text{K}$ and about twice the continuum at $25,000^{\circ}\text{K}$.

The print of a typical spectroscopic plate for a temperature measurement of a Delrin arc of 100 atmospheres and 250 amperes is shown in Figure 28. To obtain sensitivity at the 7050\AA wavelength and also in the area of the strong infrared oxygen lines up to 9000\AA , Kodak I-N plates were used. These plates, however, are relatively insensitive in the green, as seen from Figure 28. Alongside the Delrin arc with its strong continuum and strongly broadened oxygen (and hydrogen) lines, the plate shows the intensity markers of the carbon standard^(37, 38) and wavelength markers from mercury-cadmium and rubidium lamps. Note that the well-known hydrogen line H_{β} is so strongly broadened that it can no longer be distinguished from the continuum.

The result of photometer work on the spectrum of Figure 28 is shown in Figure 29, where absolute values of the integral spectral intensity $I(x)$ are plotted against the arc radius in millimeters. This curve is then transformed by the self-absorption compensated Abelian transformation into the curve of the local spectral intensity (emission coefficient) $i(r)$, Figure 30. From this, together with the theoretical results of Section II, Part C, the radial temperature distribution of the arc is computed (Figure 31).

Similar measurements were also made for Delrin arcs of 250 amperes at 150 and 200 atmospheres. The results of the temperature measurement at 150 atmospheres, where the self-absorption correction becomes quite large, are also shown in Figure 31, but the 200 atmosphere arc exhibited too much stray light for a quantitative temperature evaluation. Details of the numerical evaluation, including the previous measurement in air, are included as Table III. Figure 32 is a summary plot of all successful profile measurements:



HG-CD AND RB CARBON STANDARD DELRIN ARC

ARC DATA

PRESSURE	110 ATM
CURRENT	250 AMPS
CONSTRICTOR DIAMETER	1.5 MM
TEST NO.	DELRIN 79

Figure 28. Spectral plate for the measurement of the temperature of a high pressure Delrin arc. Along with the spectrum of the Delrin arc, spectra of the carbon crater (intensity standard) and of line radiators (Hg-Cd and Rb) for determination of wavelength are shown. Spectrum of Delrin arc is largely continuous with a few strongly broadened lines of O_I and H_I still marginally recognizable.

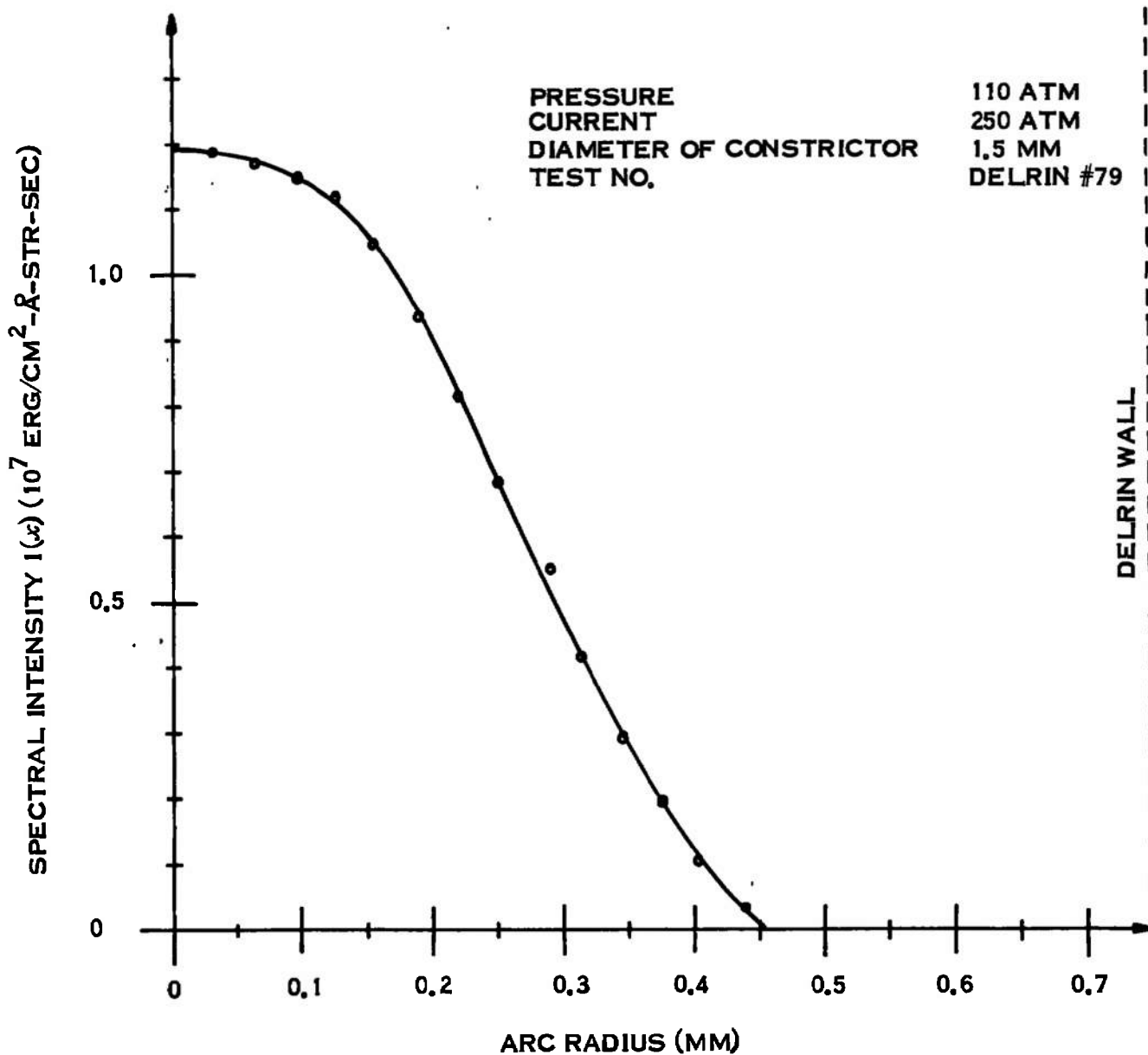


Figure 29. Absolute spectral intensity of Delrin arc as determined by comparing spectral brilliancy of arc with that of the carbon standard at the wavelength 7050 Å.

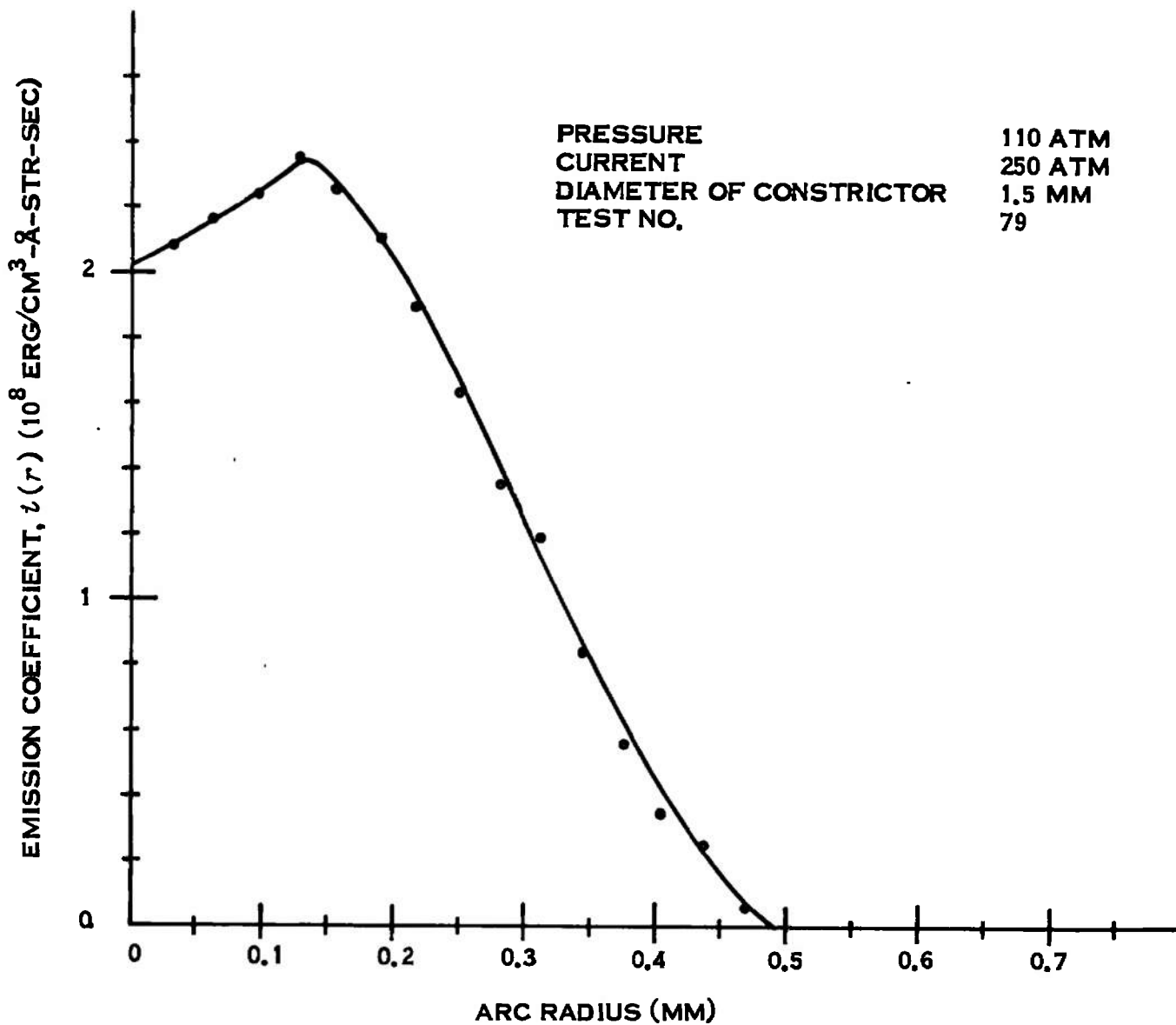


Figure 30. Local emission $i(r)$. Delrin arc shows a (probably not correct) maximum off axis. This maximum is reflected also in the radial temperature distribution (Fig. 31) but only to a minor degree.

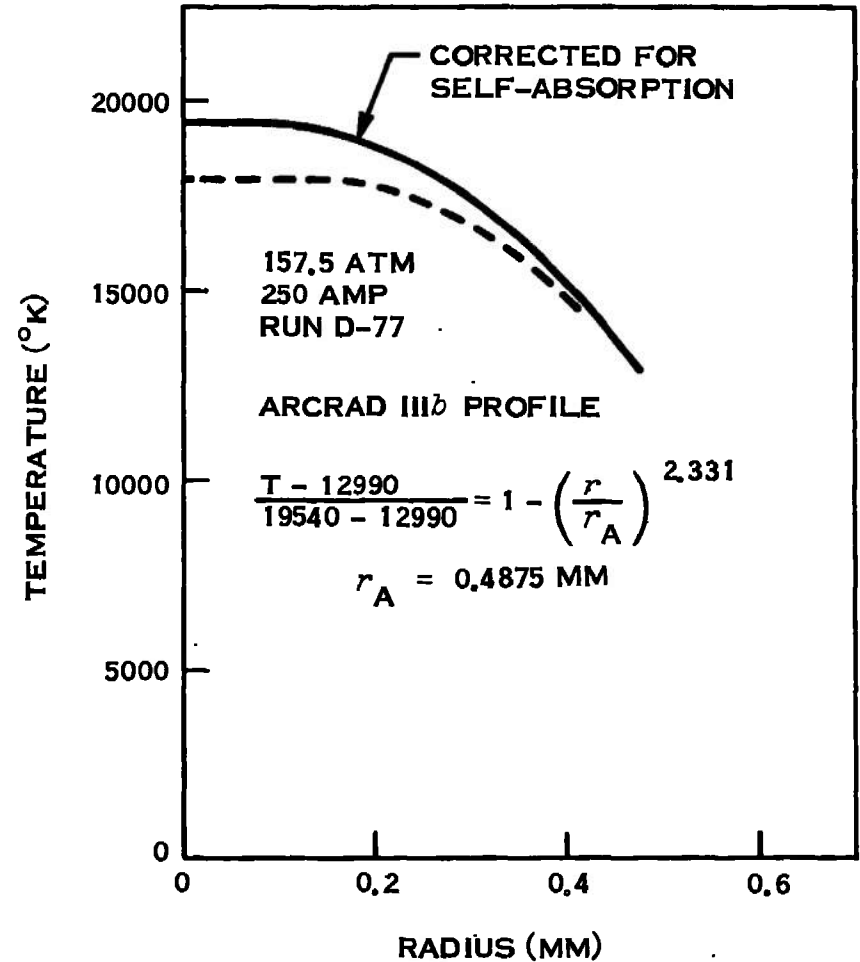
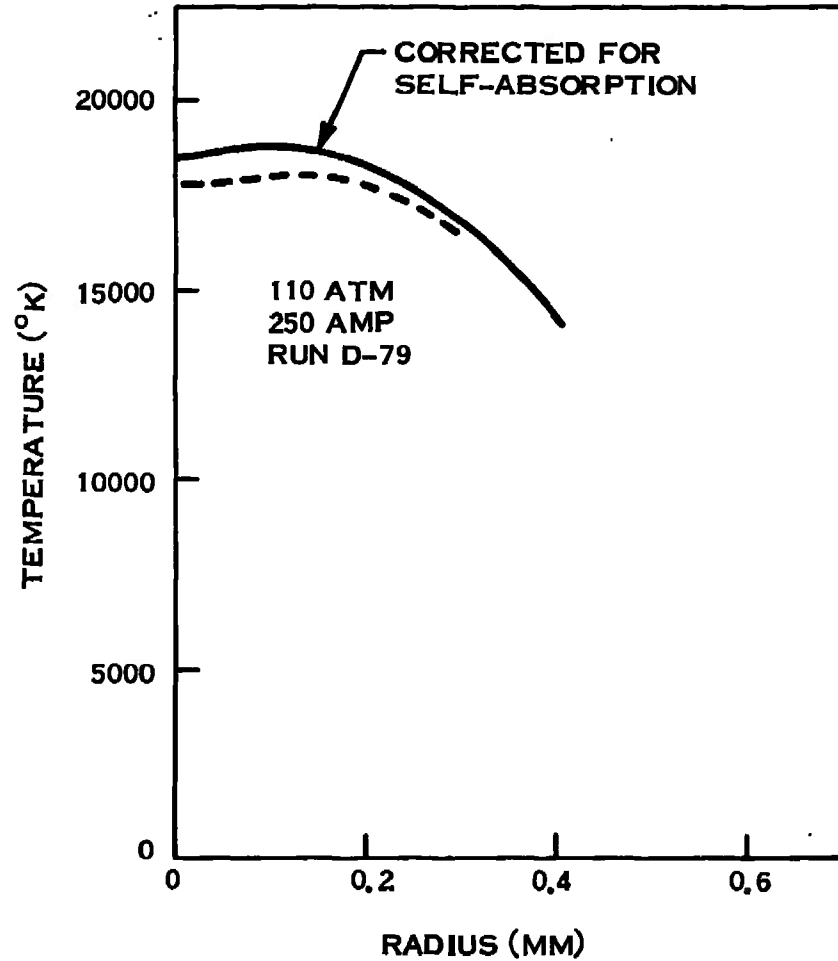


Figure 31. Radial Temperature distributions in High Pressure Delrin Arcs based on intensity measurements at 7050\AA .

Table III. Results of Temperature Profile Measurements*

AIR: 103 ATM, 1.15 AMP, 2.5 MM DIA CONSTRICTOR (RUN 400)					DELRLIN: 104 ATM, 240 AMP, 2.54 MM DIA CONSTRICTOR (RUN D-50)				
RADIUS (CM)	$I(x)$ (ERG/SEC-CM ² -Å-STR)	$I^*(x)$ (ERG/SEC-CM ² -Å-STR)	$t(r)$ (ERG/SEC-CM ³ -Å-STR)	$T(r)$ (°K)	RADIUS (CM)	$I(x)$ (ERG/SEC-CM ² -Å-STR)	$I^*(x)$ (ERG/SEC-CM ² -Å-STR)	$t(r)$ (ERG/SEC-CM ³ -Å-STR)	$T(r)$ (°K)
0.	4.700E+06	5.203E+06	7.911E+07	1.625E+04	0.	1.176E+07	1.484E+07	1.932E+08	1.824E+04
3.750E-03	4.653E+06	5.146E+06	7.792E+07	1.622E+04	4.375E-03	1.168E+07	1.474E+07	1.941E+08	1.827E+04
7.500E-03	4.516E+06	4.993E+06	7.460E+07	1.615E+04	8.750E-03	1.145E+07	1.441E+07	1.958E+08	1.829E+04
1.125E-02	4.308E+06	4.736E+06	6.977E+07	1.603E+04	1.313E-02	1.104E+07	1.380E+07	1.965E+08	1.830E+04
1.500E-02	4.051E+06	4.434E+06	6.445E+07	1.589E+04	1.750E-02	1.043E+07	1.282E+07	1.951E+08	1.828E+04
1.875E-02	3.785E+06	4.105E+06	5.959E+07	1.577E+04	2.188E-02	9.458E+06	1.131E+07	1.779E+08	1.802E+04
2.250E-02	3.460E+06	3.727E+06	5.450E+07	1.562E+04	2.625E-02	8.178E+06	9.643E+06	1.556E+08	1.765E+04
2.625E-02	3.105E+06	3.320E+06	4.922E+07	1.547E+04	3.063E-02	6.779E+06	7.881E+06	1.300E+08	1.718E+04
3.000E-02	2.727E+06	2.896E+06	4.372E+07	1.529E+04	3.500E-02	5.359E+06	6.140E+06	1.007E+08	1.655E+04
3.375E-02	2.321E+06	2.464E+06	3.827E+07	1.511E+04	3.938E-02	4.112E+06	4.596E+06	7.770E+07	1.597E+04
3.750E-02	1.938E+06	2.042E+06	3.293E+07	1.490E+04	4.375E-02	3.024E+06	3.335E+06	5.791E+07	1.535E+04
4.125E-02	1.567E+06	1.633E+06	2.769E+07	1.468E+04	4.813E-02	2.096E+06	2.286E+06	4.098E+07	1.468E+04
4.500E-02	1.213E+06	1.244E+06	2.249E+07	1.443E+04	5.250E-02	1.352E+06	1.458E+06	2.554E+07	1.383E+04
4.875E-02	8.750E+05	8.905E+05	1.778E+07	1.416E+04	5.688E-02	9.918E+05	9.742E+05	1.723E+07	1.314E+04
5.250E-02	5.539E+05				6.125E-02	6.045E+05			
5.625E-02	2.542E+05				6.562E-02	2.815E+05			
6.000E-02	-2.189E+04				7.000E-02	-1.072E+04			

DELRLIN: 110 ATM, 250 AMP, 1.52 MM DIA CONSTRICTOR (RUN D-79)					DELRLIN: 157.5 ATM, 250 AMP, 1.52 MM DIA CONSTRICTOR (RUN D-77)				
RADIUS (CM)	$I(x)$ (ERG/SEC-CM ² -Å-STR)	$I^*(x)$ (ERG/SEC-CM ² -Å-STR)	$t(r)$ (ERG/SEC-CM ³ -Å-STR)	$T(r)$ (°K)	RADIUS (CM)	$I(x)$ (ERG/SEC-CM ² -Å-STR)	$I^*(x)$ (ERG/SEC-CM ² -Å-STR)	$t(r)$ (ERG/SEC-CM ³ -Å-STR)	$T(r)$ (°K)
0.	1.191E+07	1.484E+07	2.238E+08	1.944E+04	0.	2.018E+07	3.103E+07	4.936E+08	1.938E+04
3.125E-03	1.186E+07	1.480E+07	2.266E+08	1.948E+04	3.750E-03	2.006E+07	3.079E+07	4.952E+08	1.939E+04
6.250E-03	1.173E+07	1.466E+07	2.341E+08	1.858E+04	7.500E-03	1.970E+07	3.004E+07	4.980E+08	1.941E+04
9.375E-03	1.151E+07	1.432E+07	2.435E+08	1.870E+04	1.125E-02	1.906E+07	2.863E+07	4.972E+08	1.941E+04
1.250E-02	1.117E+07	1.370E+07	2.546E+08	1.884E+04	1.500E-02	1.809E+07	2.643E+07	4.903E+08	1.936E+04
1.562E-02	1.048E+07	1.256E+07	2.433E+08	1.870E+04	1.875E-02	1.649E+07	2.314E+07	4.451E+08	1.904E+04
1.875E-02	9.420E+06	1.118E+07	2.245E+08	1.845E+04	2.250E-02	1.442E+07	1.949E+07	3.872E+08	1.861E+04
2.187E-02	8.192E+06	9.617E+06	2.004E+08	1.812E+04	2.625E-02	1.205E+07	1.564E+07	3.213E+08	1.805E+04
2.500E-02	6.892E+06	7.951E+06	1.720E+08	1.769E+04	3.000E-02	9.484E+06	1.185E+07	2.465E+08	1.733E+04
2.812E-02	5.530E+06	6.216E+06	1.421E+08	1.719E+04	3.375E-02	6.990E+06	8.535E+06	1.871E+08	1.664E+04
3.125E-02	4.191E+06	4.649E+06	1.127E+08	1.662E+04	3.750E-02	4.946E+06	5.784E+06	1.355E+08	1.590E+04
3.437E-02	2.966E+06	3.223E+06	8.438E+07	1.596E+04	4.125E-02	3.194E+06	3.514E+06	9.107E+07	1.507E+04
3.750E-02	1.914E+06	1.993E+06	5.718E+07	1.515E+04	4.500E-02	1.762E+06	1.762E+06	5.219E+07	1.403E+04
4.062E-02	1.064E+06	1.058E+06	3.506E+07	1.423E+04	4.875E-02	7.468E+05	7.411E+05	2.643E+07	1.284E+04
4.375E-02	3.743E+05				5.250E-02	6.288E+04			
4.687E-02	-6.365E+03				5.625E-02	-1.782E+05			
5.000E-02	1.760E+04				6.000E-02	4.220E+04			

* Results are based on spectral intensity measured at 7050 Å. Calculated emission included continuum only for air and continuum plus H_α line for Delrin. See Section II, part D for discussion of I(x) and I*(x).

RUN	PLASMA	CURRENT (AMP)	PRESSURE (ATM)	CONSTRICTOR DIA (MM)
400	AIR	115	103	2.5
D-50	DELRIN	240	104	2.54
D-79	DELRIN	250	110	1.52
D-77	DELRIN	250	157.5	1.52

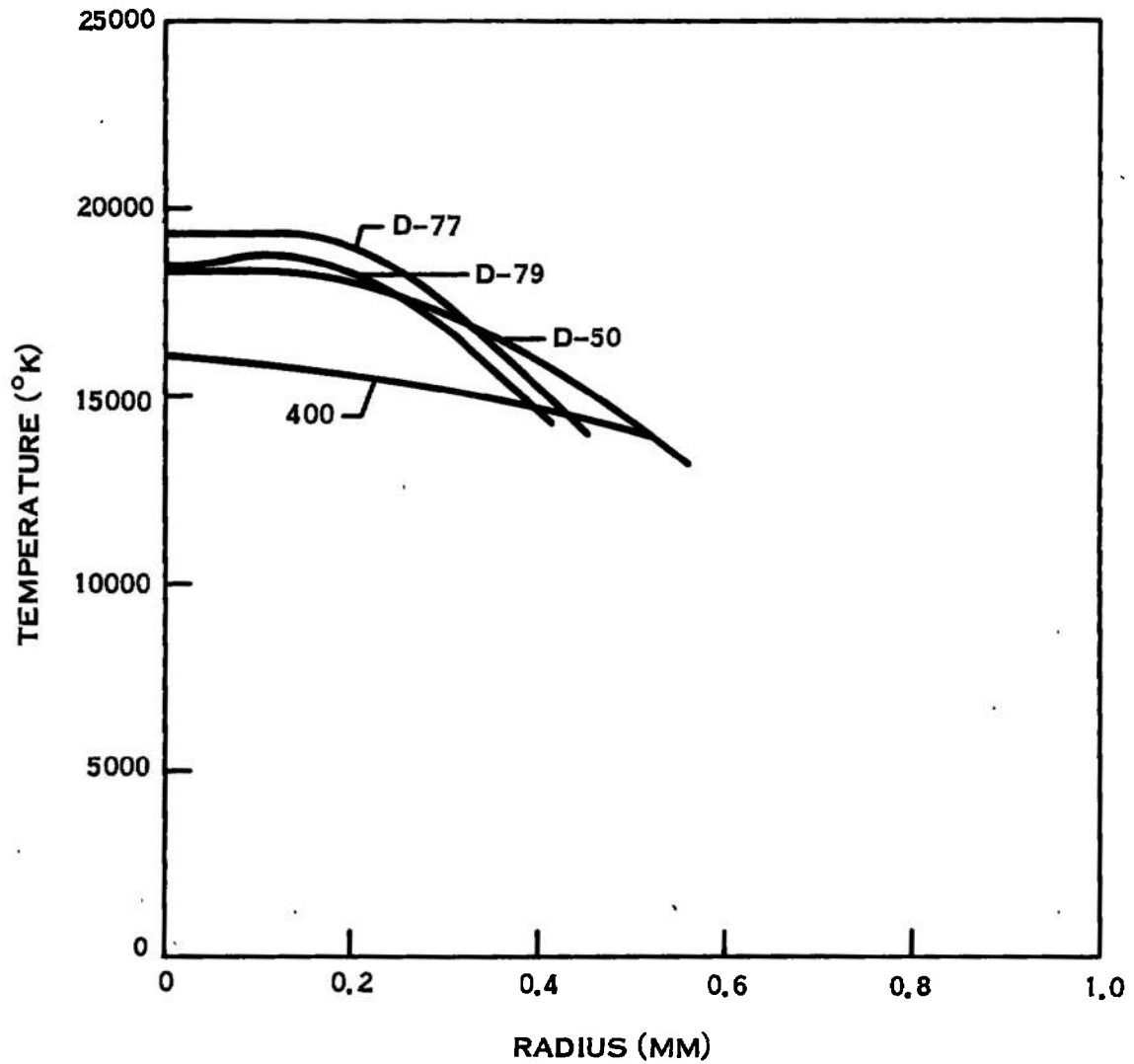


Figure 32. Summary of Temperature Measurements

SECTION IX

RESULTS AND CONCLUSIONS

The accomplishments of this study are summarized in this section. Analytically the Abel inversion has been extended to account for absorption to an optical depth of 1 or more and applied to temperature profile determination; information has been obtained on the properties of Delrin plasma and an examination has been made of the significance of some spectral lines in a very nonuniform plasma.

Experimentally, a stable, high pressure plasma was generated in an ablation type arc constrictor and the arc plasma, under conditions of the experiments, was found to be homogeneous along the arc axis. This conclusion is based on the luminous homogeneity of the plasma column, negligible pressure rise in the constrictor during arcing, and especially, the constant voltage gradient along the arc axis. The voltage gradient could be measured much more precisely than in previous work with a water arc⁽³⁾. Extremely high gradients, (sometimes exceeding 500 v/cm), and large power density were encountered. In view of its axial homogeneity the ablation type constrictor is a promising tool for end-on spectral measurements. In our work, side-on measurements required a quartz window which caused some difficulty with arc stability, though not enough to prevent good side-on spectral measurements.

A. ARC TEMPERATURE

The radial distribution of the arc temperature was measured for 250 ampere arcs in Delrin plasma with pressures in the 100 to 150 atmosphere range. The temperature distributions were flat with an occasional slight dip at the axis which, in view of the difficulties of both the analytical and experimental methods, was assumed to be spurious. The temperature measurements were based on the theoretically determined intensities at the wavelength 7050 Å. These measurements depend on the calculations of equilibrium composition (which do not include the possible effect of lowering of the ionization potential by high electron density) and absorption coefficient, as discussed in Section III. At the wavelength chosen, the dominant continuum radiation is precisely that which is best known (H_{fb} and bremsstrahlung). The H_{α} line wing is also well known.⁽¹³⁾

The measured temperatures also fall within a range bracketed by black body and electrical conduction considerations. A lower bound can be deduced from the black body limit and the fact that thermal conduction, as deduced from the measured temperature gradient at 15,000°K, and the thermal conductivity of Yos⁽²¹⁾, is less than 10 percent of the total dissipation. Making use of Figure 20, the radiation from the current carrying part of the arc must be more than 90 kw/cm. At an effective diameter of 0.4 mm radius, this corresponds to a black body temperature of 16,000°K and we know that our plasma, while not optically thin is not black because spectral lines can still be seen above the continuum background. On the other hand, a calculation of arc current using the measured temperature profiles and the air electrical conductivity of Viegas and Peng⁽²³⁾ indicates temperatures are not excessive. Calculated currents are already about 50 percent higher than measured, both in Delrin (Run D-79) and air (Run 400).

B. ENERGY DISTRIBUTION

The distribution of continuum radiation, based on the temperature profile of Figure 31b as computed using ARCRAD IIIb, is indicated in Figure 33. The plot shows the relative net radiant energy passing radially outward at any radius. Because of the very strong continuum reabsorption in the vacuum ultraviolet, 60 percent more radiant energy passes radius 0.4 mm than eventually emerges from the arc, and most of what does emerge is in the visible and near UV. This again demonstrates that the vacuum ultraviolet is a powerful mechanism for dispersing energy in the arc to the surrounding gas.

The magnitude of the calculated radiation leaving the current carrying part of the arc is 30 kw/cm, approximately one-third the total measured dissipation. This is low but may be a result of a combination of line radiation and some unaccounted for continuum. Most of the area under the black body curve at these temperatures is in the visible and near UV where the radiation processes are less certain than in the infrared, where temperature measurements were made.

C. SPECTRAL LINES

The effect of lines on radiant heat flux is greater than was anticipated because, rather than representing simply a narrow band of black body radiation, the lines are so greatly broadened that their energy is distributed over a wide spectral range. The H_{α} line, for example, covers about 1500 Å. Two of the lines evaluated using the ARCRAD IIIb program with the temperature profile of Figure 31 are shown in Figures 34 and 35. Both exhibit slight self-reversal which could not be confirmed experimentally. Energy per unit arc length for the H_{α} line was approximately 4 percent of total calculated continuum and for O_{777} about 0.6 percent.

D. APPLICATION TO AIR ARCS

The motivation for this work was a need for information about arcs in air at high pressure. However, an absolute prerequisite was an arc sufficiently stable and symmetric to yield quantitative results. Despite intensive efforts, the investigators were unable to stabilize an arc in air at conditions more severe than about 100 amperes at 100 atmospheres. Therefore, use was made of ablation stabilized arcs in Delrin plasma with the results being applicable to air as well. Differences in transport properties are small and the radiation is approaching close enough to black body to preclude large differences between the plasmas.

Figure 32 shows temperature profiles as computed from continuum radiation. Aside from uncertainties already discussed, differences are a result of the combined effects of pressure, constrictor diameter, current, constrictor type, and plasma composition.

Pressure has a relatively small effect, as can be seen by comparing Runs D-77 and D-79, which show a 5 percent change in centerline temperature for a 50 percent change in pressure. Runs D-50 and D-79 are comparable except for constrictor diameter (the larger diameter resulting in a somewhat broader profile), but the differences are small.

There is a greater difference between the 250 ampere, ablation constrictor Delrin plasma arcs and the air arc*. Though no direct comparison could be made because the air arc was unstable above 100 amperes and the Delrin arc was unstable below 200 amperes, it is believed, on the basis of indirect evidence, that the difference in the profiles is primarily due to current level. Differences in transport properties are small, and the axial uniformity of the ablation type arc indicates that the resulting flow field has little effect on the arc core. Computed continuum emission coefficients at $\lambda = 7050 \text{ \AA}$ are almost identical for the two plasmas and the temperature profile is not sensitive to small errors in $i(r)$.

* Reevaluation at $\lambda = 7050 \text{ \AA}$ has resulted in a lower temperature for the air arc than previously reported⁽¹⁾.

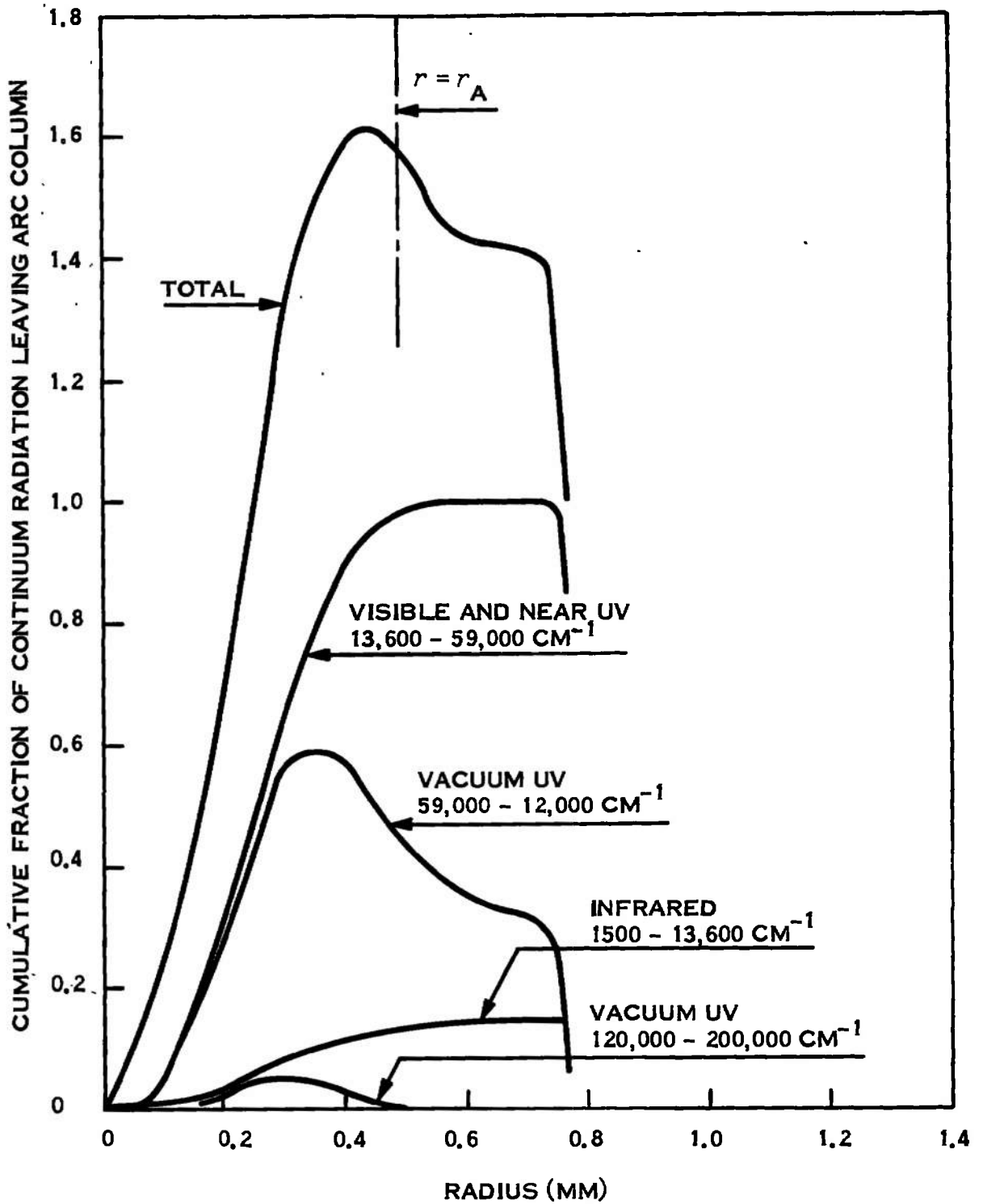


Figure 33. Cumulative Net Continuum Radiation, Temperature Profile D-77

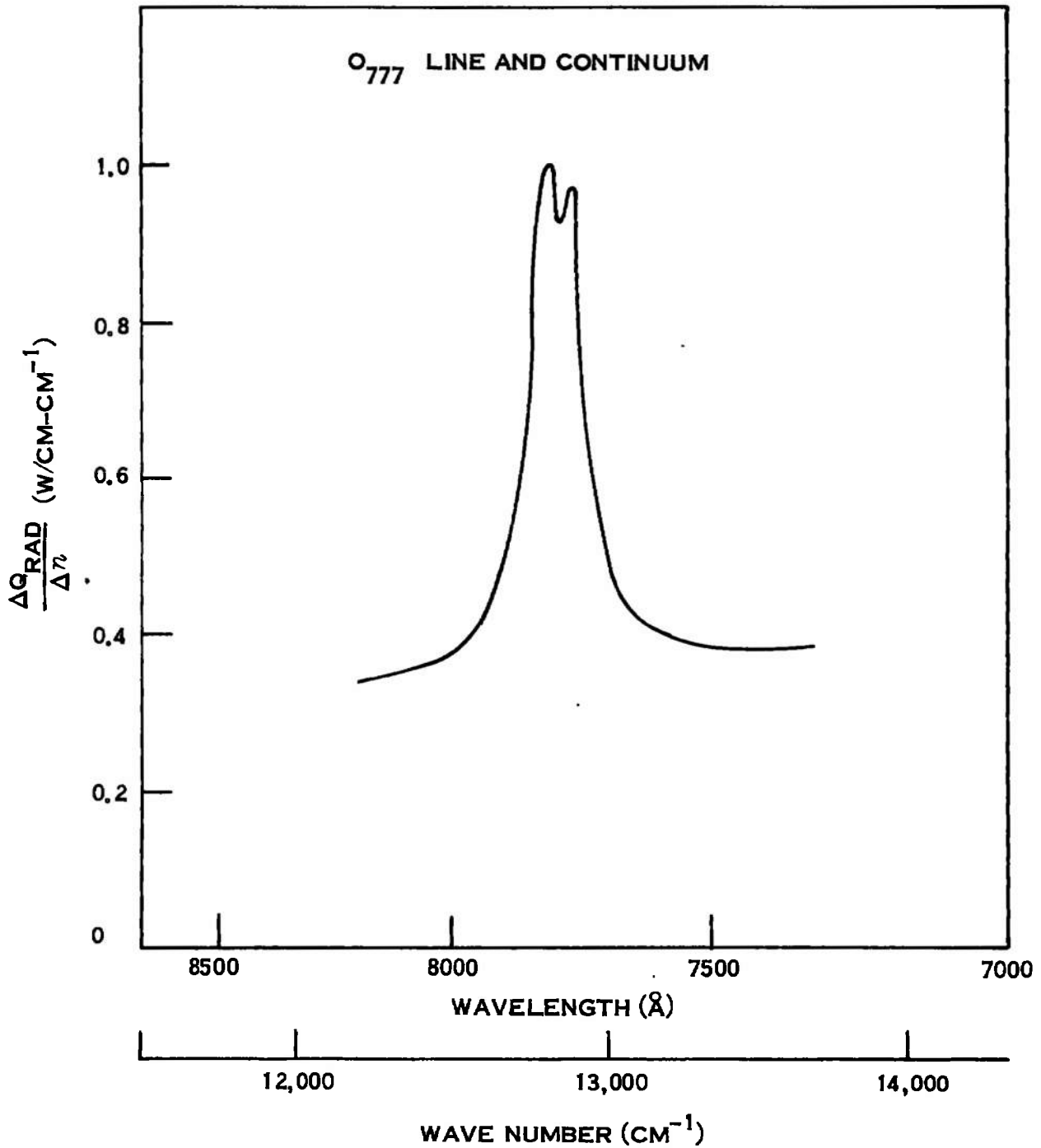


Figure 34. Net Radiant Heat Flux Per Unit Arc Column Length and Per Wave Number in Vicinity of O_{777} Line

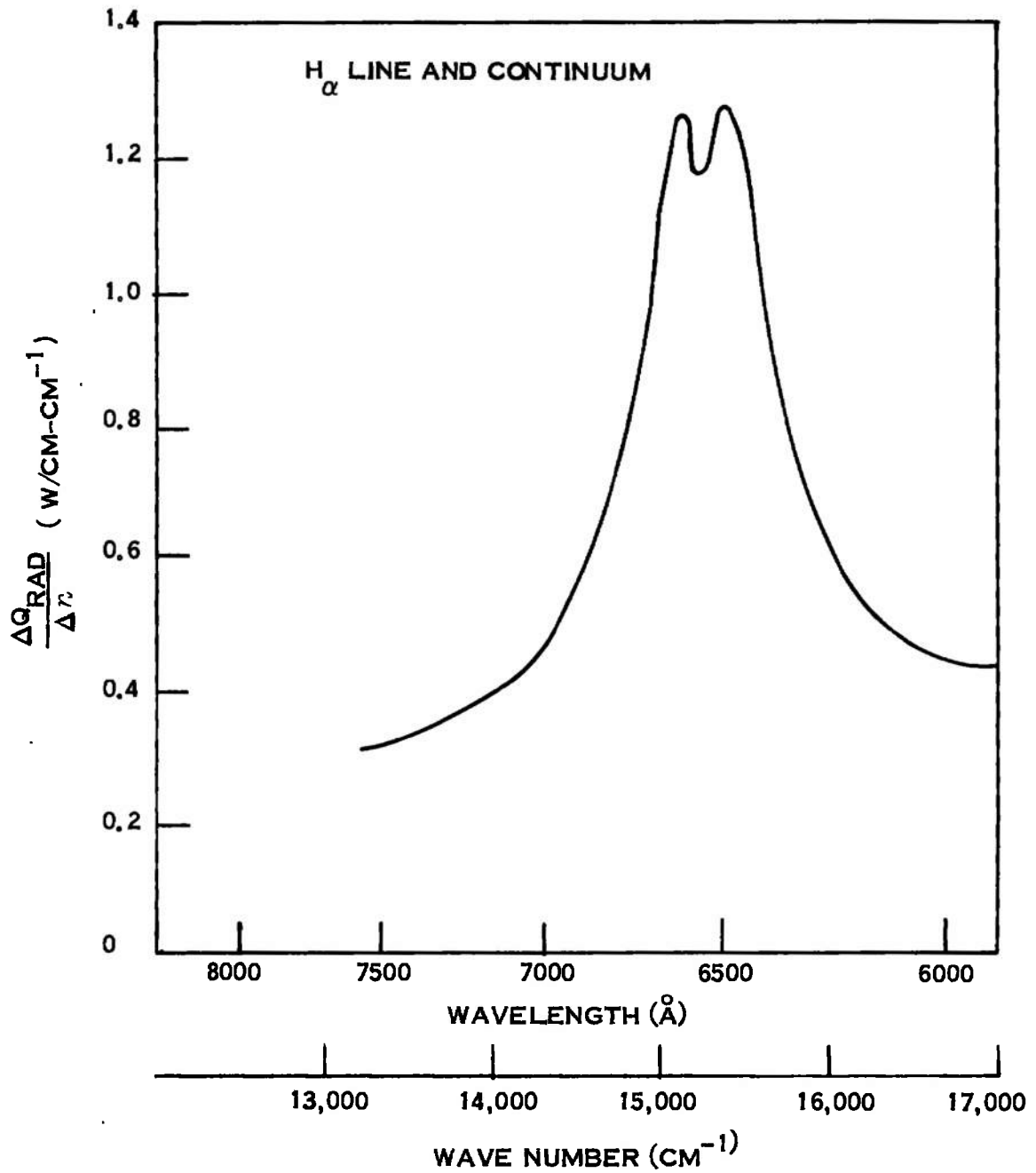


Figure 35. Net Radiant Heat Flux Per Unit Arc Column Length and Per Wave Number in Vicinity of H_α Line

APPENDIX I

ABEL INVERSION AND INTEGRATION

A. ABEL INVERSION OF A POLYNOMIAL FUNCTION

Abel inversion is the evaluation of the integral

$$f(r) = -\frac{1}{\pi} \int_r^R \frac{I'(x)dx}{\sqrt{x^2 - r^2}} \quad (1)$$

and is the inverse of Abel integration (Part B). Since $I(x)$ is a measured quantity and $f(r)$ is unknown, the inversion process is the key one in the temperature profile determination. It depends on the derivative of $I(x)$ so that the manner in which a smooth curve is fitted to the data is of great importance. Cremer's⁽¹⁷⁾ procedure for fitting polynomials by the method of least squares has been used, in program CF, Appendix II.

The arc cylinder is divided into two or more zones and a separate polynomial is computed for each zone. For each polynomial, all the data within the zone plus, where possible, three data points beyond both inner and outer zone boundaries are used. The symmetry requirement at the centerline is satisfied by using only even order terms in the polynomial associated with the innermost zone. The polynomials may be represented* by

$$I(x) = \sum_{j=1}^m A_j x^{2(j-1)} \quad (\text{innermost zone}) \quad (2)$$

$$I(x) = \sum_{j=1}^m A_j x^{j-1} \quad (\text{other zones}) \quad (3)$$

* Subscripting is compatible with computer notation which forbids zero subscripts.

When the data have been reduced to this form, the Abel inversion may be carried out analytically. Differentiating I(x) and integrating term by term, the indefinite integrals are the sum of a final series, the number of terms depending on the order of the polynomials.

$$\begin{aligned}
 \int \frac{I'(x) dx}{\sqrt{x^2 - r^2}} &= \sqrt{x^2 - r^2} \left\{ \left[\binom{2}{1} \right] A_2 + \left[\binom{4}{3} x^2 + \binom{4}{3} \binom{2}{1} r^2 \right] A_3 \right. \\
 &+ \left[\binom{6}{5} x^4 + \binom{6}{5} \binom{4}{3} x^2 r^2 + \binom{6}{5} \binom{4}{3} \binom{2}{1} r^4 \right] A_4 \\
 &+ \left[\frac{8}{7} x^6 + \binom{8}{7} \binom{6}{5} x^4 r^2 + \binom{8}{7} \binom{6}{5} \binom{4}{3} x^2 r^4 \right. \\
 &\left. + \binom{8}{7} \binom{6}{5} \binom{4}{3} \binom{2}{1} r^6 \right] A_5 + \dots \left. \right\} \quad \text{(innermost zone)} \quad (4)
 \end{aligned}$$

$$\begin{aligned}
 \int \frac{I'(x) dx}{\sqrt{x^2 - r^2}} &= \left\{ \binom{2}{1} A_3 + \left[\frac{3}{2} x \right] A_4 + \left[\binom{4}{3} x^2 + \binom{4}{3} \binom{2}{1} r^2 \right] A_5 \right. \\
 &+ \left[\binom{5}{4} x^3 + \binom{5}{4} \binom{3}{2} x r^2 \right] A_6 + \left[\binom{6}{5} x^4 + \binom{6}{5} \binom{4}{3} x^2 r^2 + \binom{6}{5} \binom{4}{3} \binom{2}{1} r^4 \right] A_7 \\
 &\left. + \left[\binom{7}{6} x^5 + \binom{7}{6} \binom{5}{4} x^3 r^2 + \binom{7}{6} \binom{5}{4} \binom{3}{2} x r^4 \right] A_8 \right\} \\
 &+ \dots + \left[A_2 + \binom{3}{2} r^2 A_4 + \binom{5}{4} \binom{3}{2} r^4 A_6 \right. \\
 &\left. + \binom{7}{6} \binom{5}{4} \binom{3}{2} r^6 A_8 + \dots \right] \ln \left(x + \sqrt{x^2 - r^2} \right) \quad \text{(other zones)} \quad (5)
 \end{aligned}$$

Generalized terms could be written for Equations 4 and 5 but they are cumbersome and the pattern for extension to higher order is clear.

Note that the integral is evaluated at a fixed value of r, which is also the first lower limit of x. Successive upper and lower limit values of x occur at the zone boundaries, where the array of coefficients changes, reaching a final upper limit at the arc radius. Evaluation of Equations 4 and 5 is performed by subroutine THIN of the optically thick inversion program, OTHICK, Appendix II.

B. ABEL INTEGRATION OF A FUNCTION KNOWN AT DISCRETE POINTS

Two different Abel integrations are required in the non-optically thick inversion process, one to find the intensity profile $I^*(x)$, and one to determine the optical depth of the absorbing path as a function of physical location. The Abel integral can be thought of as a summation over the volume elements along a line of sight, off axis in general, through the arc column Figure 36. If absorption is not significant the integral is given by

$$I_t(x) = 2 \int_x^R \frac{f(r)rdr}{\sqrt{r^2 - x^2}} \quad (6)$$

The factor of 2 arises because the line of sight is twice the limits of integration. When absorption is significant, emission from the volume elements behind the centerline will be asorbed to a greater extent than from those in front of it and instead of the factor of 2 there will be two separate integrals, with differing $f(r)$.

In our situation, the function $f(r)$ has been determined by Abel inversion at uniformly spaced, discrete points, $r_k \dots r_i, r_{i+1} \dots r_m$, and x , the lower limit of integration, is equal to r_k , see Figure 36. Integration over each interval r_i to r_{i+1} is performed with several variations on the theme of Simpson's rule, i. e., by approximating the true curve with a parabola through f_{i-1}, f_i , and f_{i+1} . When $r_{i-1} > r_k$ we let

$$\hat{f}(r) = \frac{f(r)r}{\sqrt{r^2 - r_k^2}} \quad (7)$$

and, with the notation $f \equiv f(r_i)$, find that

$$\delta I_i = \frac{(r_{i+1} - r_i)}{12} (-\hat{f}_{i-1} + 8\hat{f}_i + 5\hat{f}_{i+1}) \quad (k > 1; i \geq k + 2) \quad (8)$$

When either $r_i = r$ or $r_{i-1} = r$ Equation 7 blows up. The integral remains finite however, so Equation 6 was rewritten, defining $\eta = r/r_k$ as

$$I(\eta) = r_k \int_1^{\eta} \frac{f(\eta) \eta d\eta}{\sqrt{\eta^2 - 1}} \quad (9)$$

Integration by parts yields,

$$I(\eta) = r_k [f(\eta) \sqrt{\eta^2 - 1} - \int f'(\eta) \sqrt{\eta^2 - 1} d\eta]_1^{\eta} \quad (10)$$

Performing the indicated operations with the parabola through f_{i-1} , f_i , f_{i+1} results in

$$\begin{aligned} \delta I_i = r_k & \left\{ f_{i+1} \sqrt{\eta_{i+1}^2 - 1} - f_i \sqrt{\eta_i^2 - 1} \right. \\ & - \frac{\phi_3}{2} \left[\eta_{i+1} \sqrt{\eta_{i+1}^2 - 1} - \eta_i \sqrt{\eta_i^2 - 1} - \ln \left(\frac{\eta_{i+1} + \sqrt{\eta_{i+1}^2 - 1}}{\eta_i + \sqrt{\eta_i^2 - 1}} \right) \right. \\ & \left. \left. - \frac{\phi_2}{3} \left[\left(\eta_{i+1}^2 - 1 \right)^{3/2} - \left(\eta_i^2 - 1 \right)^{3/2} \right] \right\}; \quad (k > 1, i = k \text{ or } i = k + 1) \quad (11) \end{aligned}$$

$$\eta_i = r_i / r_k \quad (12)$$

$$\phi_1 = \frac{1}{2(\eta_{i+1} - \eta_i)} [f_{i+1} - f_{i-1}] \quad (13)$$

$$\phi_2 = \frac{1}{(\eta_{i+1} - \eta_i)^2} [f_{i-1} - 2f_i + f_{i+1}] \quad (14)$$

$$\phi_3 = \phi_1 - \eta_i \phi_2 \quad (15)$$

When $k = 1$, $r_k = 0$ and the transformation, Equation 7 reduces to the statement that \hat{f} is identical to f . Equation 8 applies when $i = 2$ but when $i = 1$ the condition of zero slope at the centerline replaces f_{i-1} so that

$$\delta I_i = \frac{(r_{i+1} - r_i)}{3} (f_i + 2 f_{i+1}) \quad i = 1 \quad (16)$$

$$\delta I_i = \frac{r_{i+1} - r_i}{12} (-f_{i-1} + 8 f_i + 5 f_{i+1}) \quad i > 1 \quad (17)$$

Equation 16 may also be obtained formally from Equation 14 by letting $f_{i-1} = f_{i+1}$ when $i = 1$.

The complete integral is then computed from the summation

$$I = \sum_{i=k}^m \delta I_i \quad (18)$$

with δI_i given by Equations 8, 11, 16, or 17 as appropriate. The integration process is performed by subroutine INT3P in the optically thick inversion program, INVER.

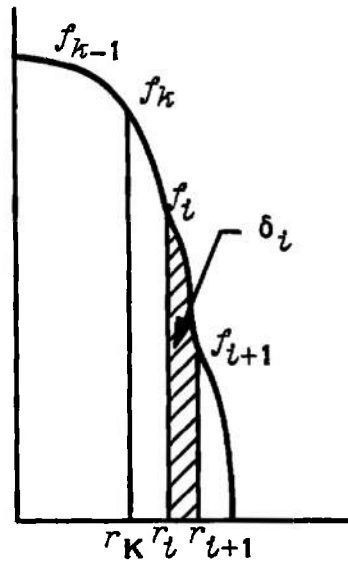
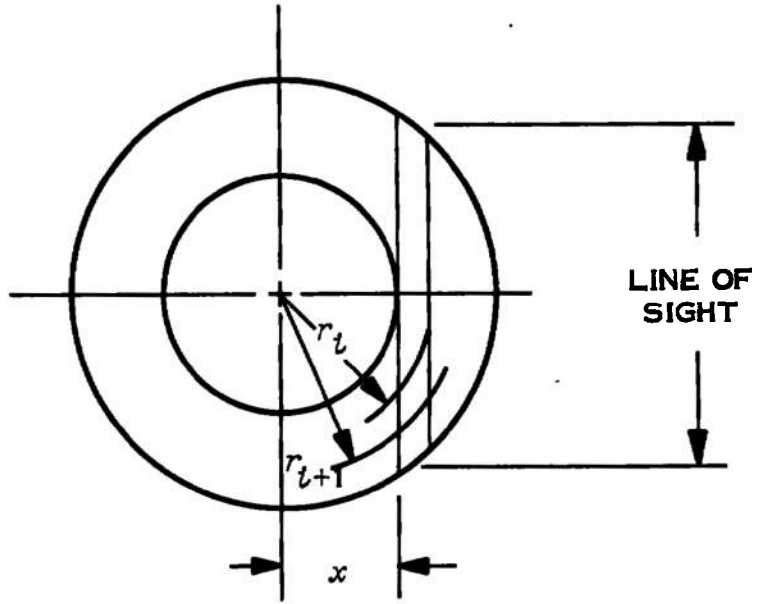


Figure 36. Abel Integration

APPENDIX II

NON-OPTICALLY THIN ABEL INVERSION PROGRAMS

A. INTRODUCTION

The computer programs CF and INVER, developed to convert raw intensity data to temperature profiles, are discussed in this Appendix. Table IV presents a brief summary of their purpose, inputs and outputs. Computations were carried out on the GE Desk Side Computer System (DSCS II), which is a time sharing system using a standard teletypewriter as a remote terminal. The system uses FORTRAN IV with a number of special features. Those special features and those library subroutines and built-in functions which pertain to CF and INVER are summarized in Tables V and VI.

One of the special features is a disc storage capability. Outputs of program CF are stored automatically in binary disc files and are retrieved as desired when program INVER is run. This is a convenience but not a necessity, and other means of data transfer can be employed with minor modifications to the programs.

B. PROGRAM CF

Program CF fits polynomials to raw intensity measurements prior to Abel inversion. Data may be at random intervals and both the degree of the polynomials and the number of zones (i.e., number of different polynomials) can be varied to obtain best fit. This a matter of some judgment, particularly since it is the slope of the intensity curve that is of interest, but, as a guide, program CF computes root mean square deviation, σ , for each fitted curve.

If the data are "reasonable," σ will tend to decrease as degree is increased* until a minimum is reached. Further increases in degree then cause σ to remain roughly constant, sometimes increasing or oscillating slightly. When this happens the additional terms in the polynomial are simply putting extra "wiggles" in the curve and the result is a progressively poorer representation of the "true" slope. Third degree consistently gave best results with our data, though the program arrays are sized for up to fifth degree. At least two zones must be used because of the special treatment given the center zone to assure zero slope at the centerline (Appendix I). The program variables are sized for up to five zones, and a total of 50 data points.

Data are read-in in dimensional form with the units specified in Table IV, but are normalized prior to computation of the least squares fit to avoid exponential overflow or underflow. Also, each curve is fitted to its own origin of coordinates to minimize round off error in the least squares algorithm. Polynomial coefficients are computed using library subroutine

* Polynomials must be at least third degree for proper operation of INVER.

LINEQ, according to the least squares criterion, as discussed by Scarborough⁽¹⁶⁾. The normalization process is then reversed and the coefficients transformed to a common axis. The latter process requires that a polynomial of the form*

$$y = \hat{A}_1 + \hat{A}_2(x - a) + \hat{A}_3(x - a)^2 + \dots + \hat{A}_{n+1}(x - a)^n \quad (1)$$

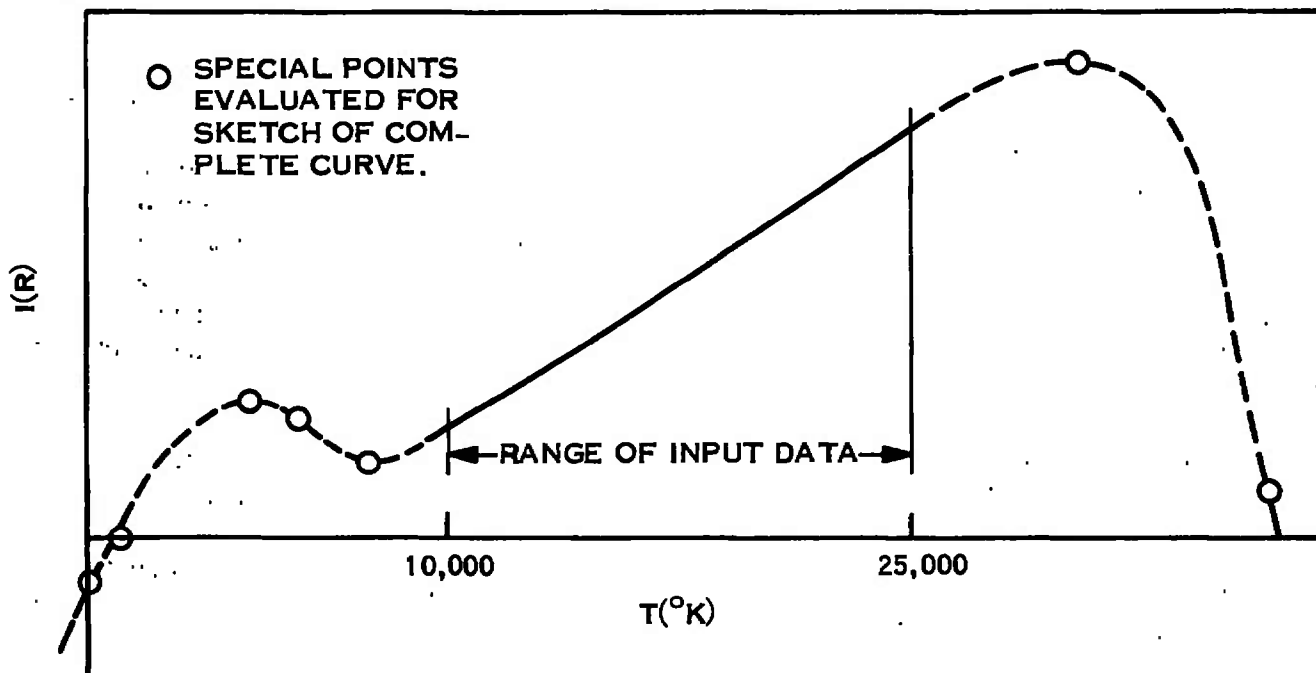
be transformed to

$$y = A_1 + A_2x + A_3x^2 + \dots + A_{n+1}x^n \quad (2)$$

The process involves finding the A's as functions of $(a, \hat{A}_1, \dots, \hat{A}_{n+1})$ by expanding Equation 1 and equating like powers of x. Library subroutine BICOF was used for generation of the necessary arrays of binomial coefficients.

C. PROGRAM INVER

Program INVER is used to compute temperature profiles. It has as its input the polynomials representing observed intensity, another polynomial relating emission coefficient to temperature, and certain run-identification information. Because emission coefficient $i(r)$ can best be represented as a polynomial in temperature rather than vice versa, Newton's method for finding the root of a polynomial was used to obtain T for a given $i(r)$. Thus it is vital that the emission coefficient polynomial increase monotonically with temperature in the range of interest. A curve fit procedure was used which evaluated all roots, extrema, and points of inflection so that complete behavior could be ascertained (see sketch).



* Subscript notation is again made to conform to computer requirements.

Choice of the number of discrete points for numerical integration is governed by a balance among truncation and round-off errors and computation time, but since all the numerical processes are integrations (differentiation of intensity profiles is analytic, Appendix I), computational errors are not a serious problem, and 15 to 20 points on the profile have proved adequate.

The block diagram of Figure 37 shows the steps in the computation. From one to six iterations were necessary to converge to minimum rms deviation, σ_{\min} , between measured and computed $I(x)$. Typically, σ_{\min} was between 1 and 2 percent of $I(0)$.

The following subprograms form an important part of INVER:

Function ROOT is a separate function subprogram for calculating $\sqrt{u^2 - v^2}$, which is useful in evaluating both the Abel integral and its inversion.

Subroutine IOFX is a straightforward calculation of $I^*(x)$ at discrete points from the polynomials.

Subroutine THIN performs the Abel inversion of $I^*(x)$. The inversion follows the analytic procedure outlined in Appendix I and is performed at each successive $x_k = r_k$ from centerline to outside edge. The indicator LIM is set as follows:

LIM	Significance
1	Lower limit of integration for zones outside the zone for which LIM = 3
2	Upper limit of integration for zones outside the zone for which LIM = 3
3	Upper and lower limits of integration at the first zone boundary where the radius exceeds r_k

LIM = 3 is a special case because then the lower limit is zero except for the logarithm term in Equation 5 of Appendix I, and this is included by setting $DEN = x_k = r_k$.

Subroutine POLYTEM is a straightforward evaluation of $i(r)$ and its first derivative (needed for Newton's method correction of trial value of temperature) at a specified temperature.

Subroutine INT3P performs the Abel integration of $f(r)$ following the procedure described in Appendix I.

Subroutine FITX fits new polynomials to corrected values of $I^*(x)$ in the same way as the original data prior to Abel inversion. Now, however, the zone structure and order are already established and the points are at uniform intervals and can be expected to conform very closely to a smooth curve.

Table IV. Programs for Computation of Temperature Profiles

Program	Purpose	Input	Output
CF	Converts raw intensity data to polynomials and transmits other input information to program INVER.	<ol style="list-style-type: none"> 1. Material (e.g. air, Delrin) pressure, wave number of intensity measurements and coefficients of the polynomial representing emission coefficient ($\text{erg/cm}^3 \text{ sec-A-str}$) 2. Number of data points, displacement from axis (cm) of each data point, intensity measurements ($10^6 \text{ erg/sec-cm}^2 \text{-A-str}$). Data must be in order of increasing displacement from the axis 3. Degree of polynomials (3 to 5), number of zones (2 to 5), arc radius (cm) 	<ol style="list-style-type: none"> 1. (optional) Column listing of input 2 2. Root mean square deviation for each zone 3. (optional) Table of values for zone: displacement, raw data, smoothed data, differences 4. Items 1 and 3 of input 5. Coefficients of the polynomials
INVER	Performs Abel inversion accounting for effects of self absorption	<ol style="list-style-type: none"> 1. Number of points to be computed for each zone 2. Output from program CF 3. Integer index after each iteration (0 = repeat cycle, 1 = print output, then repeat cycle, 2 = new case) 	<ol style="list-style-type: none"> 1. Average difference and root mean square deviation between measured $I(x)$ and computed $I(x)$ for each iteration (see Section IID). 2. Table of intensity, emission coefficients, and temperature as functions of radius (see input 3)

Table V. Special Features of the FORTRAN Language Used for Programs CF and INVER

Symbols:

- * - Comment
- & - Continuation of statement

Statements:

- ASC II** Specifies alphameric variable (used to record the type of plasma, e. g., Delrin or air)

- DATA** Statement enabling one to put many program constants into a single statement

- FILENAME** Used to specify the name of the disc storage file (used for transfer of CF output to INVER). STOW is a filename variable, whose current "value" is the name assigned to the binary disc file containing data from a specific run. The experimental run designation was used to name the file.

- PRINT:** Permits printout of alphameric information without need of a FORMAT statement

- READ:** Used for free format data input

Other Notes:

Mixed mode expressions are allowed and were used.

Logical IF is used in CF.

Subscripts of an array need not be shown explicitly in arguments of subroutine.

Table VI. Library Subroutines and Built-in Functions Used by Programs CF and INVER

LINEQ (AM, AB, NA, NB, IDIM)

Solves an array of simultaneous linear equations by Gaussian elimination

AM	Array containing the matrix of coefficients
AB	Array containing right-hand-side vector on input and solution vector when completed
NA	Number of equations
NB	Number of right-hand-side vectors
IDIM	First dimension of AM and AB arrays

BICOF (ϕ , N, COF)

Generates an array of binomial coefficients

COF (J, 1)	Array containing the coefficients ($J = 1, N$)
N	Degree of the array. For example if $N=4$ the array would be (1, 4, 6, 4, 1)

Built in Functions Used by CF and INVER

EXP	Exponential function
ALOG	Natural logarithm
SQRT	Square root
ABS	Absolute value

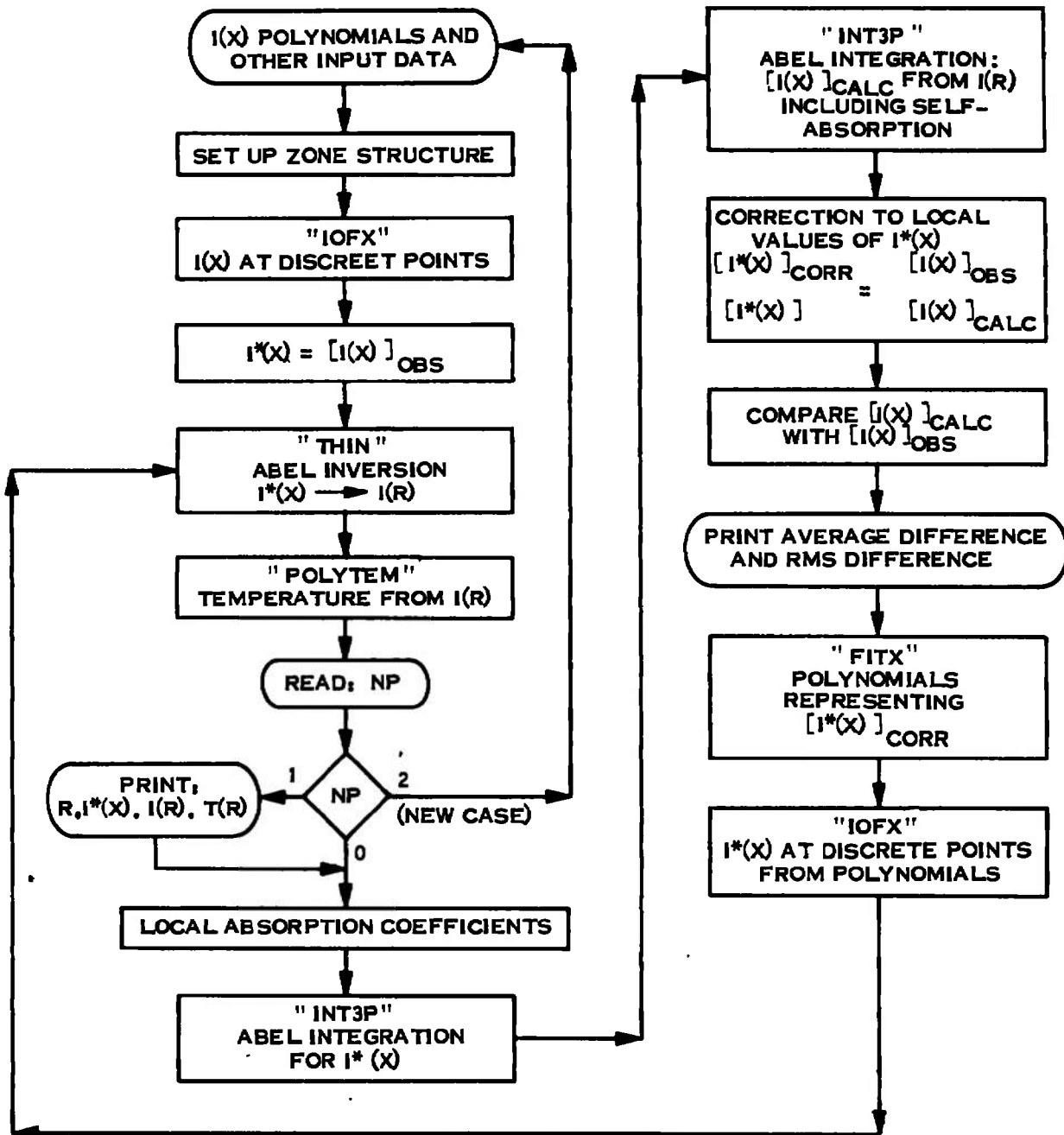


Figure 37. Program IVER Block Diagram

D. GLOSSARY

AB (J, 1)	Array for LINEQ (see Table VI)
ABS (K)	Local absorption coefficient
AJ (J)	Coefficients of polynomial for emission coefficient as f (T)
AM (JK, JL)	Array of coefficients of the polynomials for I*(x)
BICOF	See Table IV
C (J, 1) } C (J, 2) }	Constants for calculation of coefficients of terms in Abel inversion, see Equations 4 and 5, Appendix I
CF	Curve fit program
COF (JR, 1)	Output of BICOF (Table VI)
COF (JR J+1)	Modified binomial coefficient array for translation to common axis (see part B of this Appendix)
CLG	Coefficient of logarithmic term in Abel inversion, Equation 5, Appendix I
CP	Coefficient of each term in Abel inversion, Equations 4 and 5, Appendix I
CW5	Planck function term
C2W	Exponent in Planck function
DE	Increment in E
DEN	Lower integration limit value of argument of logarithm term in Abel inversion, Equation 5, Appendix I. See Subroutine THIN, part C of this Appendix.
DI	Difference between calculated and observed I(x)
DIS	Running sum of DI squared; eventually, rms deviation
DIT	Running sum of DI; eventually, mean deviation
DR	Radius increment
DT (K)	Incremental Abel integral, Subroutine INT3P

DTIS (KX)	DT applied to I*(x)
DTXR (KX)	DT applied to optical depth for computation of $[I(x)]_{\text{calc}}$; also used by Subroutine POLYTEM for derivative of temperature-emission coefficient function
E	Eta, dimensionless argument in Abel integral, Equation 10, Appendix I
ER	$\sqrt{1 - \eta^2}$, Equation 10 Appendix I
FITX	Subroutine, see part C of this Appendix
INT3P	Subroutine, see part C of this Appendix
INVER	Non-optically thin Abel inversion program
IOFX	Subroutine, see part C of this Appendix
J	Index of intensity polynomial coefficients and emission polynomial coefficients
JK } JL }	Indices in least squares algorithm
JM	Maximum value of J
JORD	Degree of emission coefficient polynomial
JP	J-1, argument of BICOF
K	Index on radius or displacement from axis
KDIF	KSTR T-KI
KF	Largest value of K for which RD (K) falls at or within the boundary of a particular zone
KFIN	Largest value of K for set of data to which a polynomial will be fitted, see KSTR T
KI	Smallest value of K for which RD (K) falls at or within the boundary of a particular zone
KM	Maximum value of K

KMX	KM-1
KSTRT	First value of K for which RD (K) falls within the set of data to which a polynomial will be fitted (up to 3 points beyond zone boundary are included where possible)
KX	Summation index; $KX \geq K$
KX1	$KX + 1$
KX2	Index on first point of 3-point Abel integral, $KX2 = 2$ or $KX+2$
KZ	Number of subintervals per zone (INVER only).
L	Counts number of iterations. Initial (optically thin) inversion is numbered zero.
LIM	See Subroutine OTHIN, part C of this Appendix.
LINEQ	See Table VI.
M	Number of data points included in a curve fit calculation
MAT	ASC II variable; Table VI
MDATA	Total number of data points
MS	Indexing constant, Subroutine IFTX
MZ (NZ)	Value of K at outer boundaries of zones
N	$NORD + 1$
NA, NB	See LINEQ
NNEW	Option indicator. Used by operator to execute choices to be made while program is being run.
NNN	See NNEW
NNZ	Total number of zones ($2 \leq NNZ \leq 5$)
NORD	Degree of I(x) polynomials
NP	See NNEW

NPO Counts iterations to find $i(r)$ from $T(r)$. Causes print out if this process does not converge.

NXY See NNEW

NZ Index on zone

P Pressure (program CF)

PHI (I, J) Array of values of polynomial functions for least squares algorithm.

PH1 }
PH2 }
PH3 } Coefficients of Abel integral, Equation 12, Appendix I

PI 3.1415927

POLYTEM Subroutine, see part C of this Appendix

PR Pressure (program INVER)

PTSF Abel integral function defined at beginning of subroutine INT3P; see Equation 11 of Appendix I

Q (KX) Array of inputs to Abel integral, dummy argument of the subroutine INT3P

QI (KX) Same as Q to start with, but modified by Subroutine INT3P. Used to avoid changes in the array in INVER which Q (kx) represents

R (K) Radius (program INVER)

RD (K) Radius (program CF)

RDMAX (NZ) Radius of outer boundary of zone

RDMIN (NZ) Radius of inner boundary of zone

REF Reference value for normalization prior to curve fit

ROOT Function, see part C of this Appendix

RO Arc radius

SIGMA	rms deviation: raw data from polynomials in program CF; computed intensity from measured intensity in program INVER
STOW	See Table V
T (K)	Temperature
THIN	Subroutine, see part C of this Appendix
TI (K)	Emission coefficient
TIA (K)	Intensity including self-absorption
TICK	Residual in calculation of temperature from emission coefficient
TILG	Coefficient of logarithm term in Abel inversion, Equation 5, Appendix I
TIS (K)	$I^*(x)$; intensity which would have been observed if part of the energy had not been reabsorbed.
TIP	Running sum in Abel inversion
TIX (K)	Observed intensities, as computed from polynomials fitted to data
TIZ	Running sum to compute TI (K)
TPW	Running sum to compute T (K)
TXR	Optical depth; also used by Subroutine POLYTEM for temperature calculation
WN	Wave number
X	Displacement from arc centerline; this the lower limit of Abel integral (program INVER)
X (I)	Dependent variable, least squares algorithm
YA (K)	Intensity from fitted polynomials (program CF)
YI (K)	Intensity data (program CF)

E. LISTINGS

```

00010 * CF, UP TO 50 DATA POINTS, 5 ZONES, 5TH DEGREE POLYNOMIALS
00020   1 FORMAT(1H ,F6.3,1XE11.3)
00030   3 FORMAT(" ")
00040   8 FORMAT(3(1PE11.3),2(1PE10.2))
00050  10 FORMAT(2(1PE10.2))
00060   COMMON AB(6,1),AR(6,6),COF(6,7)
00070   COMMON X(20),Y(20),PHI(50,6),AM(6,6)
00080   COMMON RDMAX(6),RDMIN(6),RD(50),YI(50)
00090   COMMON YA(16)
00100   DIMENSION AJ(7)
00110   FILENAME STOW
00120   ASCII MAT(1)
00130 *
00140 *   READ IN DATA
00150  100 PRINT 3
00160     PRINT 3
00170     PRINT:"AIR OR DELR, PRESS, WN, JORD, JM, AJ(J)"
00180     PRINT 3
00190     READ: MAT, P, WN, JORD, JM, (AJ(J), J=1,JM)
00200     PRINT 3
00210     PRINT:"MDATA, ALL R(CM), ALL I(X)(10.E6ERG/SEC-CM2-A-STR)"
00220     PRINT 3
00230     READ:MDATA,(RD(K),K=1,MDATA),(YI(K),K=1,MDATA)
00240     RD(MDATA+1)=RD(MDATA)+1.
00250     DO 102 K=1,MDATA
00260  102 YI(K)=YI(K)*1.E6
00270     PRINT:"LIST DATA=1, "
00280     READ:NNN
00290     IF(NNN) 105,105,104
00300  104 PRINT 1,(RD(K),YI(K),K=1,MDATA)
00310 *
00320 *   SET UP ZONE STRUCTURE
00330  105 PRINT:"NORD,NNZ,R0"
00340     READ: NORD, NNZ, R0
00350     N=NORD+1
00360     RDMIN(1)=0.
00370     RDMAX(1)=R0/NNZ
00380     DO 110 NZ=2, NNZ
00390     RDMIN(NZ)=RDMAX(NZ-1)
00400  110 RDMAX(NZ)=RDMAX(1)*NZ
00410     RDMAX(NNZ)=R0
00420     PRINT:"PRINT COORD=1, "
00430     READ: NXY
00440     IF(NXY) 100, 114, 112
00450  112 PRINT:"      R          YI          YA"
00460  114 DO 300 NZ=1, NNZ
00470 *
00480 *   SELECT DATA
00490     K=0
00500  120 K=K+1
00510     IF(RD(K)-RDMAX(NZ)-.00001)120,120,130
00520  130 KFIN=K
00530     K=K+2
00540     IF(MDATA-K) 150, 140, 140

```

```

00550      140 M=K
00560      GO TO 160
00570      150 M=MDATA
00580      KFIN=MDATA
00590      160 K=0
00600      170 K=K+1
00610      IF(RD(K)-RDMIN(NZ)+.00001) 170,180,180
00620      180 KSTRT=K-1
00630      KI=K-3
00640      IF(KI) 190, 190, 200
00650      190 KSTRT=1
00660      KI=1
00670      200 KDIF=KSTRT-KI
00680      M=M+1-KI
00690      DO 210 I=1, M
00700      X(I)=RD(I-1+KI)
00710      210 Y(I)=YI(I-1+KI)
00720 *
00730 * LEAST SQUARES
00740      REF=X(M)-X(1)
00750      DO 255 I=1,M
00760      PHI(I,1)=1.
00770      IF(NZ-1) 1000, 220, 240
00780      220 DO 230 J=2, N
00790      230 PHI(I,J)=(X(I)/REF)**(2*(J-1))
00800      GO TO 255
00810      240 DO 250 J=2, N
00820      250 PHI(I,J)=((X(I)-X(1))/REF)**(J-1)
00830      255 CONTINUE
00840      DO 256 JL=1,N
00850      DO 256 JK=1,N
00860      AM(JK,JL)=0.
00870      DO 256 I=1,M
00880      256 AM(JK,JL)=AM(JK,JL)+PHI(I,JL)*PHI(I,JK)
00890      DO 257 JK=1,N
00900      AB(JK,1)=0.
00910      DO 257 I=1,M
00920      257 AB(JK,1)=AB(JK,1)+Y(I)*PHI(I,JK)
00930      CALL LINEQ(AM,AB,N,1,6)
00940      DO 261 J=2,N
00950      IF(NZ-1) 1000, 258, 260
00960      258 AB(J,1)=AB(J,1)*(REF**(2*(1-J)))
00970      GO TO 261
00980      260 AB(J,1)=AB(J,1)*(REF**(1-J))
00990      261 CONTINUE
01000 *
01010 * SHIFT AXIS
01020      IF((NZ.EQ.1).OR.(X(1).EQ.0.)) GO TO 266
01030      DO 262 J=1,N
01040      JP=J-1
01050      CALL BICOF(0,JP,COF)
01060      DO 262 JR=1, J
01070      262 COF(JR,J+1)=COF(JR,1)
01080      DO 264 JR=1, N

```

```

01090      AR(JR,NZ)=0.
01100      DO 264 J=JR, N
01110      264 AR(JR,NZ)=AR(JR,NZ)+((-1)**(J-JR))*AB(J,1)*
01120 &      (RD(KI)**(J-JR))*COF(JR,J+1)
01130      GO TO 270
01140      266 DO 268 J=1,N
01150      268 AR(J,NZ)=AB(J,1)
01160 *
01170 *   CALC AND PRINT COORD
01180      270 M=KDIF+KFIN-KSTRT+1
01190      ISTRT=KDIF+1
01200      SIGMA=0.
01210      DO 290 I=ISTRT, M
01220      IF(NZ-1) 1000, 272, 276
01230      272 CONTINUE
01240      YA(I)=AR(1,1)
01250      DO 274 J=2,N
01260      274 YA(I)=YA(I)+AR(J,1)*X(I)**(2*(J-1))
01270      GO TO 290
01280      276 CONTINUE
01290      YA(I)=AR(1,NZ)+AR(2,NZ)*X(I)
01300      DO 280 J=3,N
01310      280 YA(I)=YA(I)+AR(J,NZ)*(X(I)**(J-1))
01320      290 SIGMA=SIGMA+(Y(I)-YA(I))**2
01330      SIGMA=SQRT (SIGMA/(M-KDIF))
01340      IF(NXY) 298,298,294
01350      294 CONTINUE
01360      DO 296 I=ISTRT,M
01370      295 PRINT 8, X(I),Y(I),YA(I)
01380      296 CONTINUE
01390      298 PRINT 10, SIGMA
01400      PRINT 3
01410      300 CONTINUE
01420 *
01430 *   RESULTS TO FILE OR TRY AGAIN
01440      PRINT:"NEW FIT=0, TO FILE=1, "
01450      READ: NNEW
01460      IF (NNEW) 1000, 105, 302
01470      302 PRINT:"FILENAME"
01480      READ:STOW
01490      BEGIN FILE STOW
01500      WRITE(STOW) MAT,P,WN,JORD,JM,(AJ(J),J=1,JM),N,NNZ,R0
01510      END FILE STOW
01520      DO 310 NZ=1, NNZ
01530      WRITE(STOW)(AR(J,NZ),J=1,N)
01540      310 PRINT: (AR(J,NZ), J=1,N)
01550      PRINT 3
01560      END FILE STOW
01570      PRINT:"NEW FIT=0, NEW DATA=1"
01580      CLOSE FILE STOW
01590      READ: NNEW
01600      IF(NNEW) 1000, 105, 100
01610      1000 STOP
01620      END

```

```

00010 * INVER, 2ND TO 5TH ORDER, 2 TO 5 ZONES, UP TO 10 PTS/ZONE
00020     COMMON AR(6,5), MZ(5), C(6,2), R(5), TIS(5), TIX(5)
00030     COMMON ABS(5), T(5), TI(5), TIA(5)
00040     COMMON TXR(5), DTIS(5), DTXR(5), DR,X,K,KX1,KMX,KM
00050     COMMON PHI(17,6),AM(6,6),COF(6,7),Y(17),AB(6,1)
00060     COMMON AJ(7), JORD,JM
00070     FILENAME STOW, P
00080     ASCII MAT(1)
00090     1 FORMAT(4(1PE11.3))
00100     2 FORMAT(1H ,A4,F6.0,F8.0,I3,I5,I4)
00110     3 FORMAT(" ")
00120 *
00130 * INPUT, ZONE STRUCTURE AND PROGRAM CONSTANTS
00140     PI=3.1415927
00150     100 PRINT:"FILENAME, PTS/ZONE "
00160     READ: STOW, KZ
00170     BEGIN FILE STOW
00180     READ(STOW,END=105)MAT,PR,WN,JORD,JM,(AJ(J),J=1,JM),N,NNZ,R0
00190     105 DO 110 NZ=1,NNZ
00200     READ(STOW,END=110)(AR(J,NZ),J=1,N)
00210     110 MZ(NZ)=KZ*NZ+1
00220     KM=MZ(NNZ)
00230     KMX=KM-1
00240     DR=R0/KMX
00250     DO 120 K=1, KM
00260     120 R(K)=(K-1)*DR
00270 * CW5=(ERG/SEC-CM2-A-STR)
00280     CW5=(WN**5)*1.1909E-13
00290     C2W=1.438*WN
00300     C(2,1)=2.
00310     DO 130 J=3, N
00320     C(J,1)=(2.*(J-1))/(2.*J-3.)
00330     130 C(J,2)=(J-1.)/(J-2.)
00340 *
00350 * ISTAR(X) TO I(R) AND TEMPERATURE
00360     TI(KM)=0.
00370     TIA(KM)=0.
00380     CALL IOFX(KZ, N,NNZ)
00390     DO 150 K=1, KM
00400     150 TIX(K)=TIS(K)
00410     NORD=N-1
00420     PRINT 3
00430     PRINT:"      P(ATM)      WN  JORD  NORD  NNZ"
00440     PRINT 2, MAT, PR, WN, JORD, NORD, NNZ
00450     L=-1
00460     220 L=L+1
00470     CALL THIN(N,NNZ)
00480     DO 570 K=1,KMX
00490     TI(K)=-TI(K)/PI
00500     T(K)=10000.

```

```

00510      CALL POLYTEM
00520      IF(TI(K)-TXR(K)) 570, 570, 300
00530      300 T(K)=T(K)+2000.
00540      IF(T(K)-30000) 360, 360, 340
00550      340 PRINT:"TEMP TOO HIGH"
00560      360 NPO=0
00570      CALL POLYTEM
00580      IF(TI(K)-TXR(K)) 400, 570, 300
00590      400 T(K)=T(K)-(TXR(K)-TI(K))/DTXR(K)
00600      NPO=NPO+1
00610      IF(NPO-50) 430, 430, 420
00620      420 PRINT:"T UNSTABLE"
00630      430 CALL POLYTEM
00640      TICK=1.-TXR(K)/TI(K)
00650      TICK=SQRT(TICK+TICK)
00660      IF(TICK-.0005) 570, 570, 400
00670      570 CONTINUE
00680      T(KM)=10000.
00690 *
00700 * P/O OF ISTAR(X), I(R) AND TEMPERATURE
00710      PRINT 3
00720      PRINT:L," ITERATION, PRINT=1, NEW FILE=2 "
00730      READ:NP
00740      IF(NP-1) 590, 575, 573
00750      573 CLOSE FILE STOW
00760      GO TO 100
00770      575 PRINT:"      R      ISTAR(X)      I(R)      TEMP"
00780      DO 580 K=1, KM
00790      580 PRINT 1, R(K), TIS(K), TI(K), T(K)
00800      PRINT 3
00810 *
00820 * THICK INVERSION
00830 *
00840 * ABSORPTION COEFFICIENT AND LOCAL ISTAR(X)
00850      590 DIT=0.
00860      DIS=0.
00870      DO 600 K=1, KM
00880      600 ABS(K)=TI(K)/(CW5/(EXP(C2W/T(K))-1.))
00890      TIS(KM)=0.
00900      DO 800 K=1, KMX
00910      KX1=K+1
00920      X=R(K)
00930      CALL INT3P(TI,DTIS)
00940      TIS(K)=0.
00950      DO 640 KX=K,KMX
00960      640 TIS(K)=TIS(K)+2.*DTIS(KX)
00970 *
00980 *
00990      CALL INT3P(ABS,DTXR)
01000      TXR(K)=0.

```

```

01010      DO 660 KX=K,KMX
01020      660 TXR(KX+1)=TXR(KX)+DTXR(KX)
01030 *
01040 * COMPUTED OTHICK I(X) AND NEW ISTAR(X)
01050      TIA(K)=0.
01060      DO 680 KX=K,KMX
01070      DTIA=DTIS(KX)*(EXP(-TXR(KM)+TXR(KX))+EXP(-TXR(KM)-TXR(KX)))
01080      680 TIA(K)=TIA(K)+DTIA
01090      TIS(K)=TIS(K)*TIX(K)/TIA(K)
01100 *
01110 * COMPARISON OF MEASURED AND COMPUTED OTHICK I(X)
01120      DI=TIA(K)-TIX(K)
01130      DIT=DIT+DI
01140      DIS=DIS+DI**2
01150      800 CONTINUE
01160      DIT=DIT/KMX
01170      DIS=SQRT(DIS/KMX)
01180      PRINT:"  AVG DIF      SIGMA"
01190      PRINT 1, DIT, DIS
01200      CALL FITX(KZ,N,NNZ)
01210      CONTINUE
01220      CALL IOFX(KZ,N,NNZ)
01230      GO TO 220
01240      1000 STOP
01250      ... END

```

```

00010      FUNCTION ROOT(U,V)
00020      REAL ROOT
00030      ROOT=SQRT (U**2-V**2)
00040      RETURN
00050      END

```



```

00010      SUBROUTINE IOFX(KZ, N, NNZ)
00020      COMMON AR(6,5), MZ(5), C(6,2), R(51), TIS(51), TIX(51)
00030      COMMON ABS(51), T(51), TI(51), TIA(51)
00040      COMMON TXR(51), DTIS(51), DTXR(51), DR,X,K,KX1,KMX,KM
00050      COMMON PHI(17,6),AM(6,6),COF(6,7),Y(17),AB(6,1)
00060      KF=MZ(1)
00070      DO 140 K=1, KF
00080      TIS(K)=AR(1,1)
00090      DO 140 J=2, N
00100 140 TIS(K)=TIS(K)+AR(J,1)*R(K)**(2*(J-1))
00110      DO 165 NZ=2, NNZ
00120      KI=MZ(NZ)-KZ+1
00130      KF=MZ(NZ)
00140      DO 165 K=KI, KF
00150 150 TIS(K)=AR(1,NZ)
00160      DO 165 J=2,N
00170 165 TIS(K)=TIS(K)+AR(J,NZ)*(R(K)**(J-1))
00180      RETURN
00190      END

```

```

00010      SUBROUTINE THIN(N,NNZ)
00020      COMMON AR(6,5), MZ(5), C(6,2), R(51), TIS(51), TIX(51)
00030      COMMON ABS(51), T(51), TI(51), TIA(51)
00040      COMMON TXR(51), DTIS(51), DTXR(51), DR,X,K,KX1,KMX,KM
00050      COMMON PHI(17,6),AM(6,6),COF(6,7),Y(17),AB(6,1)
00060 * OTHIN I(X) TO I(R)
00070      DO 560 K=1, KMX
00080      TI(K)=0.
00090      NZ=0
00100 340 NZ=NZ+1
00110      X=R(MZ(NZ))
00120      IF(X-R(K)) 340, 340, 350
00130 350 DEN=R(K)
00140      LIM=3
00150      IF(NZ-1) 1000, 400, 500
00160 360 DEN=1
00170 370 TI(K)=TI(K)+TIZ
00180      NZ=NZ+1
00190      LIM=1
00200      IF(NNZ-NZ)560, 500, 500
00210 380 TI(K)=TI(K)-TIZ
00220      X=R(MZ(NZ))
00230      LIM=2
00240      GO TO 500
00250 400 TIZ=2.*AR(2,1)
00260      DO 420 J=3, N
00270      CP=C(J,1)
00280      TIP=CP*(X**(2*J-4))

```

```

00290      DO 410 JP=3, J
00300      CP=CP+C((J-JP+2),1)
00310 410 TIP=TIP+CP*(X**(2*(J-JP)))*(R(K)**(2*(JP-2)))
00320 420 TIZ=TIZ+TIP*AR(J,1)
00330      TIZ=TIZ*ROOT(X,R(K))
00340      GO TO 360
00350 500 TIZ=C(3,2)*AR(3,NZ)+C(4,2)*AR(4,NZ)*X
00360      IF(N-4) 1000, 540, 510
00370 510 DO 530 J=5, N
00380      CP=C(J,2)
00390      TIP=CP*(X**(J-3))
00400      DO 520 JP=5, J, 2
00410      CP=CP+C((J-JP+3),2)
00420 520 TIP=TIP+CP*(X**(J-JP))*(R(K)**(JP-3))
00430 530 TIZ=TIZ+TIP*AR(J,NZ)
00440 540 TIZ=TIZ*ROOT(X,R(K))
00450      TILG=AR(2,NZ)
00460      CLG=1
00470      DO 550 J=4, N, 2
00480      CLG=C(J,2)*CLG
00490 550 TILG=TILG+CLG*(R(K)**(J-2))*AR(J,NZ)
00500      TIZ=TIZ+TILG*ALOG((X+ROOT(X,R(K)))/DEN)
00510      GO TO (380, 370, 360), LIM
00520 560 CONTINUE
00530      RETURN
00540 1000 STOP
00550      END

```

```

00010      SUBROUTINE POLYTEM
00020      COMMON AR(6,5), MZ(5), C(6,2), R(51), TIS(51), TIX(51)
00030      COMMON ABS(51), T(51), TI(51), TIA(51)
00040      COMMON TXR(51), DTIS(51), DTXR(51), DR,X,K,KX1,KMX,KM
00050      COMMON PHI(17,6),AM(6,6),COF(6,7),Y(17),AB(6,1)
00060      COMMON AJ(7), JORD,JM
00070      TPW=T(K)
00080      TXR(K)=AJ(1)
00090      DTXR(K)=AJ(2)
00100      DO 100 J=2, JORD
00110      DTXR(K)=DTXR(K)+TPW*J*AJ(J+1)
00120      TXR(K)=TXR(K)+TPW*AJ(J)
00130 100 TPW=TPW*T(K)
00140      TXR(K)=TXR(K)+TPW*AJ(JM)
00150      RETURN
00160      END

```

```

00010      SUBROUTINE INT3P(Q,DT)
00020      COMMON AR(6,5), MZ(5), C(6,2), R(51), TIS(51), TIX(51)
00030      COMMON ABS(51), T(51), TI(51), TIA(51)
00040      COMMON TXR(51), DTIS(51), DTXR(51), DR,X,K,KX1,KMX,KM
00050      COMMON PHI(17,6),AM(6,6),COF(6,7),Y(17),AB(6,1)
00060      DIMENSION Q(51), QI(51), E(3), ER(3), DT(51)
00070      PTSF(EU,EL,EUR,ELR,FU,FL,PH2,PH3)=FU*EUR-FL*ELR
00080 &      -(PH3/2)*(EU*EUR-EL*ELR-ALOG((EU+EUR)/(EL+ELR)))
00090 &      -(PH2/3)*(EUR**3-ELR**3)
00100      DO 10 KX=K,KM
00110      10 QI(KX)=Q(KX)
00120      IF(K-1) 15, 15, 20
00130      15 DT(1)=(DR/3)*(2*QI(1)+QI(2))
00140      KX2=2
00150      GO TO 60
00160      20 DE=DR/X
00170      QI(K-1)=Q(K-1)
00180      E(1)=1
00190      ER(1)=0.
00200      DO 30 J=2,3
00210      E(J)=E(J-1)+DE
00220      30 ER(J)=ROOT(E(J),E(1))
00230      PH1=(QI(K+1)-QI(K-1))/(2*DE)
00240      PH2=(QI(K+1)-2*QI(K)+QI(K-1))/DE**2
00250      PH3=PH1-E(1)*PH2
00260      DT(K)=X*PTSF(E(2),E(1),ER(2),ER(1),QI(K+1),QI(K),PH2,PH3)
00270      IF(KMX-K) 70, 70, 40
00280      40 PH1=(QI(K+2)-QI(K))/(2*DE)
00290      PH2=(QI(K+2)-2*QI(K+1)+QI(K))/DE**2
00300      PH3=PH1-E(2)*PH2
00310      DT(KX1)=X*PTSF(E(3),E(2),ER(3),ER(2),QI(K+2),QI(K+1),
00320 &      PH2,PH3)
00330      IF(KMX-KX1) 70, 70, 50
00340      50 DO 55 KX=KX1, KM
00350      55 QI(KX)=QI(KX)*R(KX)/ROOT(R(KX),X)
00360      KX2=KX1+1
00370      60 DO 65 KX=KX2, KMX
00380      65 DT(KX)=(DR/12)*(-QI(KX-1)+8*QI(KX)+5*QI(KX+1))
00390      70 RETURN
00400      END

```

```

00010 SUBROUTINE FITX(KZ,N,NNZ)
00020 COMMON AR(6,5), MZ(5), C(6,2), R(51), TIS(51), TIX(51)
00030 COMMON ABS(51), T(51), TI(51), TIA(51)
00040 COMMON TXR(51), DTIS(51), DTXR(51), DR,X,K,KX1,KMX,KM
00050 COMMON PHI(17,6),AM(6,6),COF(6,7),Y(17),AB(6,1)
00060 NB=1
00070 NA=N
00080 DO 950 NZ=1, NNZ
00090 IF(NZ-1) 1000, 400, 500
00100 400 MS=0
00110 M=0
00120 GO TO 650
00130 500 MS=MZ(NZ-1)-4
00140 IF(MS) 550, 600, 600
00150 550 MS=0
00160 M=MZ(NZ-1)-1
00170 GO TO 650
00180 600 M=3
00190 650 IF(KM-(MZ(NZ)+3)) 700, 750, 750
00200 700 M=M+(KZ+1)+(KM-MZ(NZ))
00210 GO TO 800
00220 750 M=M+(KZ+1)+3
00230 800 REF=DR*(M-1)
00240 DO 880 I=1,M
00250 PHI(I,1)=1.
00260 Y(I)=TIS(I+MS)
00270 IF(NZ-1) 1000, 820, 840
00280 820 DO 830 J=2,N
00290 830 PHI(I,J)=(R(I)/REF)**(2*(J-1))
00300 GO TO 880
00310 840 DO 850 J=2,N
00320 850 PHI(I,J)=(DR*(I-1)/REF)**(J-1)
00330 880 CONTINUE
00340 890 DO 892 JL=1, N
00350 DO 892 JK=1,N
00360 AM(JK,JL)=0.
00370 DO 892 I=1,M
00380 892 AM(JK,JL)=AM(JK,JL)+PHI(I,JL)*PHI(I,JK)
00390 DO 896 JK=1,N
00400 AB(JK,1)=0.
00410 DO 896 I=1,M
00420 896 AB(JK,1)=AB(JK,1)+Y(I)*PHI(I,JK)
00430 CALL LINEQ(AM,AB,NA,NB,6)
00440 DO 915 J=2,N
00450 IF(NZ-1) 1000, 900, 910
00460 900 AB(J,1)=AB(J,1)*(REF**(2*(1-J)))
00470 GO TO 915
00480 910 AB(J,1)=AB(J,1)*(REF**(1-J))

```

```

00490 915 CONTINUE
00500 IF(MS) 1000, 942, 920
00510 920 DO 930 J=1,N
00520 JP=J-1
00530 CALL BICOF(0,JP,COF)
00540 DO 930 JR=1, J
00550 930 COF(JR,J+1)=COF(JR,1)
00560 DO 940 JR=1, N
00570 AR(JR,NZ)=0.
00580 DO 940 J=JR, N
00590 940 AR(JR,NZ)=AR(JR,NZ)+((-1)**(J-JR))*AB(J,1)*(R(M
00600 & Z(NZ-1)-3)**(J-JR))*COF(JR,(J+1))
00610 GO TO 950
00620 942 DO 946 J=1,N
00630 946 AR(J,NZ)=AB(J,1)
00640 950 CONTINUE
00650 RETURN
00660 1000 STOP
00670 END

```

REFERENCES

1. Marston, C.H., Frind, G. and Mishkovsky, V., "Research Study of Radiation Heat Flux from High Pressure Air Arcs," Arnold Engineering Development Center Report AEDC TR-66-258 (December 1966) See Also General Electric Co., Philadelphia, Pa., Report TIS R67SD58 (October 1967).
2. Anderson, J.A., "Spectral Energy Distribution of the High Current Vacuum Tube," *Astrophys. Jour.* 75, 394-406 (1932).
3. Peters, T.H., "Temperatur-Und Strahlungsmessungen A.M. Wasserstabilisierten Hochdruck-bogen," *Z. Physik.* 135, 573-592 (1953).
4. Ogurtsova, N.N., Podmoshenskii, V.M. and Shelemina, V.M., "Characteristics of the Plasma Jet of a Powerful Capillary Discharge," *Opt. Spectr.* 15, 404-406 (1963).
5. Charatis, G. and Hershey, T.L., Technical Note BN-361 University of Maryland (July 1964).
6. Frind, G., "An Ablation Type Plasma Generator," *Journ. Spacecraft and Rockets*, 2, 458-460 (1965).
7. Bogen, P., Conrads, H., and Rusbuldt, D., "Bestimmung von Temperatur und Dichte Eines Gleitfunken Aus Der Bremsstrahlung inn Infrarot," *Z. Physik*, 186, 240-248 (1965).
8. Bohn, W.L., Beth, M.V. and Nedder, G., "Spectroscopic Investigation of an Argon Plasma with Self Absorption," 7th Int. Conf. of Ion. Phen. in Gases, Belgrade (1965).
9. Maisenhalder, F. and Schoeck, P.A., "The Energy Balance of Electric Arcs Without and With Superimposed Gas Flow," 7th Int. Conf. of Ion Phen. in Gases, Belgrade (1965).
10. Powers, W.E. and Patrick, R.M., "A Magnetic Annular Arc," *Phys, of Fluids* 5 1196-1206 (Oct. 1962).
11. Greim, H.R., Plasma Spectroscopy, (McGraw Hill Book Co., New York, 1964).
12. Penner, S.S., Quantitative Molecular Spectroscopy and Gas Emissivities, Addison-Wesley Publishing Co., Reading, Mass. (1959).
13. Griem, H.R., Kolb, A.C. and Shen, K.Y., "Stark Broadening of Hydrogen Lines in Plasma," U.S. Naval Research Laboratory Report NRL 5455 (March 1960).
14. Moore, Charlotte E., Atomic Energy Levels, Vol. 1, Circular of the National Bureau of Standards 467 (June 15, 1949).

15. Wiese, W. L., Smith, M. W., and Glennon, B. M., Atomic Transition Probabilities, Vol. 1, National Standard Reference Data Series, National Bureau of Standards 4 (May 20, 1966).
16. Scarborough, J. B., Numerical Mathematical Analysis (The Johns Hopkins Press, Baltimore, 1962 5th ed.).
17. Cremers, C. J. and Birkebak, R. C., "Application of the Abel Integral Equation to Spectrographic Data," Applied Optics 5, 6 (June 1966).
18. Browne, W. G., "Thermodynamic Properties of the Earth's Atmosphere," GE-MSD, Radiation and Space Physics, TM 2 (1962).
19. Gilmore, F. R., "Equilibrium Composition and Thermodynamic Properties of Air to 24000°K," Rand Corp. Report RM-1543 (August 1955).
20. Brinkley, S. R., Jr., and Lewis, B., "The Thermodynamics of Combustion Gases: General Considerations," U.S. Bureau of Mines Report of Investigations 4806 (April 1952).
21. Yos, J. M., "Transport Properties of Nitrogen, Hydrogen, Oxygen, and Air to 30,000°K," AVCO Report No. RAD-TM-63-7 (1963).
22. Peng, T. and Pindroh, A. L., "An Improved Calculation of Gas Properties at High Temperatures-Air," Magnetohydrodynamics Proc. Fourth Biennial Gas Dynamics Symposium (Northwestern University Press, Evanston, Illinois, 1962).
23. Viegas, J. R. and Peng, T. C., "Electrical Conductivity of Ionized Air in Thermodynamic Equilibrium," ARS Journal, 31, 654-657 (1961).
24. Weber, H. E., "Skin Friction and Heat Transfer for High Temperature Equilibrium Boundary Layer Flows With and Without Blowing," General Electric Co., Philadelphia, Pa., Report TIS R66SD9 (March 1966).
25. Main, R. P. and Bauer, E., "Equilibrium Opacities and Emmissivities of Hydrocarbon-Air Mixtures at High Temperatures," J. Quant. Spectrosc. Radiat. Transfer 7 527-557, (1957).
26. Aller, L. A., Astrophysics - The Atmospheres of the Sun and Stars, Ronald Press, New York (1953).
27. Burgess, A. and Seaton, M. F., "A General Formula for the Calculation of Atomic Photo-ionization Cross Sections," Monthly Notices Royal Astron. Soc 120, 121 (1960).

28. Sherman, M.P. and Kulander, J. L. , "Free-Bound Radiation from Nitrogen Oxygen and Air," General Electric Co. , Philadelphia, Pa. , TIS R65SD15 (May 1965).
29. Kulander, J. and Sherman, M. P. , "Bound-Free Absorption Coefficients for C^- , C and C^+ ," Theoretical Fluid Physics Technical Memorandum No. 7 (April 1965).
30. Chandrasekhar, S. and Breen, H. , "On the Continuous Absorption Coefficient of the Negative Hydrogen Ion III," Ap. J. 104, 430-445, (1946).
31. Chandrasekhar, S. , "On the Continuous Absorption Coefficient of the Negative Hydrogen Ion IV," Ap. J. , 128 114-123 (1958).
32. Breene, R.G. , Jr. , "The Bound Free Continuum for C^- ," Planet. Space Sci. 2 10-16 (1959).
33. Branscomb, L. M. et al. , "Photodetachment Cross Section and the Electron Affinity of Atomic Oxygen," Phys. Rev. 111, 2, 504-513 (1958).
34. Unsöld, A. , Physik der Sternatmosphären (Springer, Berlin 1955).
35. Breene, R.G. and Nardone, M. , "Radiant Emission from High Temperature Equilibrium Air," General Electric Co. Report TIS R61SD020 (May 1961).
36. Schultz, E.O. , Holland, A.C. and Marmo, F. F. , "Planetary Aeronomy, VIII:A Congeries of Absorption Cross Sections for Wavelengths Less than 3000 Å," NASA CR-15 (September 1963).
37. Euler, J. , "Der Graphitbogen Als Spectralphotometrisches Strahldichtenormal im Gebiet Von 0.25 Bis. 1.8 μ ," Annalen Phys. 11, 203-224 (1953).
38. Null, M.R. and Lozier, W.W. , "Carbon Arc as a Radiation Standard," J. Opt. Soc. Am. 52, 1156-1162 (1962).

DOCUMENT CONTROL DATA - R & D

(Security classification of title, body of abstract and indexing ennoletion must be entered when the overall report is classified)

1. ORIGINATING ACTIVITY (Corporate author) General Electric Company, Missile and Space Division, Valley Forge Space Technology Center King of Prussia, Pennsylvania		2a. REPORT SECURITY CLASSIFICATION UNCLASSIFIED	
		2b. GROUP N/A	
3. REPORT TITLE RADIATION HEAT FLUX FROM HIGH PRESSURE ARCS			
4. DESCRIPTIVE NOTES (Type of report and inclusive dates) Final Report			
5. AUTHOR(S) (First name, middle initial, last name) C. H. Marston, G. Frind, and B. Damsky			
6. REPORT DATE July 1968	7a. TOTAL NO. OF PAGES 111	7b. NO. OF REFS 38	
8a. CONTRACT OR GRANT NO. F40600-67-C-0005	9a. ORIGINATOR'S REPORT NUMBER(S) AEDC-TR-68-146		
b. PROJECT NO. 8951	9b. OTHER REPORT NO(S) (Any other numbers that may be assigned this report) N/A		
c. Program Element 6140501F			
d. Task 895107			
10. DISTRIBUTION STATEMENT This document has been approved for public release and sale; its distribution is unlimited.			
11. SUPPLEMENTARY NOTES Available in DDC		12. SPONSORING MILITARY ACTIVITY Arnold Engineering Development Center Air Force Systems Command Arnold Air Force Station, Tennessee	
13. ABSTRACT An ablation type constrictor has been developed in which an electric arc at very high pressure is sufficiently stable for spectrographic measurements. Radial temperature distributions were determined for 250 ampere arcs in Delrin, (COH ₂) _n , plasma at 100 and 150 atmospheres. Voltage gradient is constant along the arc axis and as high as 500 volts/cm. Pressure gradient in the constrictor is negligible. These two results indicate strongly that in spite of the self-induced flow field, the ablation type arc is homogeneous along the column. Temperature measurement was based on non-optically thin Abel inversion of continuum intensity measurements useful to an optical depth of one or more, which related temperature to theoretically computed continuum emission. A previously developed arc radiation model was extended to include a few selected lines, and these contribute significantly to total radiation because they are very much broadened.			

14 KEY WORDS	LINK A		LINK B		LINK C	
	ROLE	WT	ROLE	WT	ROLE	WT
1 constrictors, ablation-type 2 electric arcs 3 spectrographic measurements temperature distributions 4 arc heaters plasmas heat flux radiation 5. Heat exchangers. 15-7						